



Publication Year	2023
Acceptance in OA @INAF	2023-11-20T13:47:40Z
Title	Search for Gravitational Waves Associated with Fast Radio Bursts Detected by CHIME/FRB during the LIGO-Virgo Observing Run O3a
Authors	Abbott, R.; Abbott, T. D.; Acernese, F.; Ackley, K.; Adams, C.; et al.
DOI	10.3847/1538-4357/acd770
Handle	http://hdl.handle.net/20.500.12386/34478
Journal	THE ASTROPHYSICAL JOURNAL
Number	955



Search for Gravitational Waves Associated with Fast Radio Bursts Detected by CHIME/FRB during the LIGO–Virgo Observing Run O3a

R. Abbott¹, T. D. Abbott², F. Acernese^{3,4}, K. Ackley⁵, C. Adams⁶, N. Adhikari⁷, R. X. Adhikari¹, V. B. Adya⁸, C. Affeldt^{9,10}, D. Agarwal¹¹, M. Agathos^{12,13}, K. Agatsuma¹⁴, N. Aggarwal¹⁵, O. D. Aguiar¹⁶, L. Aiello¹⁷, A. Ain¹⁸, P. Ajith¹⁹, T. Akutsu^{20,21}, S. Albanesi²², A. Allocca^{4,23}, P. A. Altin⁸, A. Amato²⁴, C. Anand⁵, S. Anand¹, A. Ananyeva¹, S. B. Anderson¹, W. G. Anderson⁷, M. Ando^{25,26}, T. Andrade²⁷, N. Andres²⁸, T. Andric²⁹, S. V. Angelova³⁰, S. Ansoldi^{31,32}, J. M. Antelis³³, S. Antier³⁴, S. Appert¹, Koji Arai¹, Koya Arai³⁵, Y. Arai³⁵, S. Araki³⁶, A. Araya³⁷, M. C. Araya¹, J. S. Areeda³⁸, M. Arène³⁴, N. Aritomi³⁴, N. Arnaud^{39,40}, S. M. Aronson², K. G. Arun⁴¹, H. Asada⁴², Y. Asali⁴³, G. Ashton⁵, Y. Aso^{44,45}, M. Assiduo^{46,47}, S. M. Aston⁶, P. Astone⁴⁸, F. Aubin²⁸, C. Austin², S. Babak³⁴, F. Badaracco⁴⁹, M. K. M. Bader⁵⁰, C. Badger⁵¹, S. Bae⁵², Y. Bae⁵³, A. M. Baer⁵⁴, S. Bagnasco²², Y. Bai¹, L. Baiotti⁵⁵, J. Baird³⁴, R. Bajpai⁵⁶, M. Ball⁵⁷, G. Ballardín⁴⁰, S. W. Ballmer⁵⁸, A. Balsamo⁵⁴, G. Baltus⁵⁹, S. Banagiri⁶⁰, D. Bankar¹¹, J. C. Barayoga¹, C. Barbieri^{61,62,63}, B. C. Barish¹, D. Barker⁶⁴, P. Barneo²⁷, F. Barone^{64,65}, B. Barr⁶⁶, L. Barsotti⁶⁷, M. Barsuglia³⁴, D. Barta⁶⁸, J. Bartlett⁶⁴, M. A. Barton^{20,66}, I. Bartos⁶⁹, R. Bassiri⁷⁰, A. Basti^{18,71}, M. Bawaj^{72,73}, J. C. Bayley⁶⁶, A. C. Baylor^{74,75}, M. Bazzan⁷⁶, B. Bécsy⁷⁶, V. M. Bedakihalé⁷⁷, M. Bejger⁷⁸, I. Belahcene³⁹, V. Benedetto⁷⁹, D. Beniwal⁸⁰, T. F. Bennett⁸¹, J. D. Bentley¹⁴, M. BenYaala³⁰, F. Bergamin^{9,10}, B. K. Berger⁷⁰, S. Bernuzzi¹³, C. P. L. Berry^{15,66}, D. Bersanetti⁸², A. Bertolini⁵⁰, J. Betzwieser⁶, D. Beveridge⁸³, R. Bhandare⁸⁴, U. Bhardwaj^{50,85}, D. Bhattacharjee⁸⁶, S. Bhaumik⁶⁹, I. A. Bilenko⁸⁷, G. Billingsley¹, S. Bini^{88,89}, R. Birney⁹⁰, O. Birnholtz⁹¹, S. Biscans^{1,67}, M. Bischi^{46,47}, S. Biscoveanu⁶⁷, A. Bisht^{9,10}, B. Biswas¹¹, M. Bitossi^{18,40}, M.-A. Bizouard⁹², J. K. Blackburn¹, C. D. Blair^{6,83}, D. G. Blair⁸³, R. M. Blair⁶⁴, F. Bobba^{93,94}, N. Bode^{9,10}, M. Boer⁹², G. Bogaert⁹², M. Boldrini^{48,95}, L. D. Bonavena⁷⁴, F. Bondu⁹⁶, E. Bonilla⁷⁰, R. Bonnand²⁸, P. Booker^{9,10}, B. A. Boom⁵⁰, R. Bork¹, V. Boschi¹⁸, N. Bose⁹⁷, S. Bose¹¹, V. Bossilkov⁸³, V. Boudart⁵⁹, Y. Bouffanais^{74,75}, A. Boumerdassi¹⁷, A. Bozzi⁴⁰, C. Bradaschia¹⁸, P. R. Brady⁷, A. Bramley⁶, A. Branch⁶, M. Branchesi^{29,98}, J. E. Brau⁵⁷, M. Breschi¹³, T. Briant⁹⁹, J. H. Briggs⁶⁶, A. Brillet⁹², M. Brinkmann^{9,10}, P. Brockill⁷, A. F. Brooks¹, J. Brooks⁴⁰, D. D. Brown⁸⁰, S. Brunett¹, G. Bruno⁴⁹, R. Bruntz⁵⁴, J. Bryant¹⁴, J. Buchanan⁵⁴, T. Bulik¹⁰⁰, H. J. Bulten⁵⁰, A. Buonanno^{101,102}, R. Busicchio¹⁴, D. Buskulic²⁸, C. Buy¹⁰³, R. L. Byer⁷⁰, L. Cadonati¹⁰⁴, G. Cagnoli²⁴, C. Cahillane⁶⁴, J. Calderón Bustillo^{105,106}, J. D. Callaghan⁶⁶, T. A. Callister^{107,108}, E. Calloni^{4,23}, J. Cameron⁸³, J. B. Camp¹⁰⁹, M. Canepa^{82,110}, S. Canevarolo¹¹¹, M. Cannavacciuolo⁹³, K. C. Cannon²⁶, H. Cao⁸⁰, Z. Cao¹¹², E. Capocasa²⁰, E. Capote⁵⁸, G. Carapella^{93,94}, F. Carbognani⁴⁰, J. B. Carlin¹¹³, M. F. Carney¹⁵, M. Carpinelli^{40,114,115}, G. Carrillo⁵⁷, G. Carullo^{18,71}, T. L. Carver¹⁷, J. Casanueva Diaz⁴⁰, C. Casentini^{116,117}, G. Castaldi¹¹⁸, S. Caudill^{50,111}, M. Cavaglia⁸⁶, F. Cavalier³⁹, R. Cavalieri⁴⁰, M. Ceasar¹¹⁹, G. Cella¹⁸, P. Cerdá-Durán¹²⁰, E. Cesarini¹¹⁷, W. Chaibi⁹², K. Chakravarti¹¹, S. Chalathadka Subrahmanya¹²¹, E. Champion¹²², C.-H. Chan¹²³, C. Chan²⁶, C. L. Chan¹⁰⁶, K. Chan¹⁰⁶, M. Chan¹²⁴, K. Chandra⁹⁷, P. Chanial⁴⁰, S. Chao¹²³, P. Charlton¹²⁵, E. A. Chase¹⁵, E. Chassande-Mottin³⁴, C. Chatterjee⁸³, Debarati Chatterjee¹¹, Deep Chatterjee⁷, M. Chaturvedi⁸⁴, S. Chaty³⁴, C. Chen^{126,127}, H. Y. Chen⁶⁷, J. Chen¹²³, K. Chen¹²⁸, X. Chen⁸³, Y.-B. Chen¹²⁹, Y.-R. Chen¹³⁰, Z. Chen¹⁷, H. Cheng⁶⁹, C. K. Cheong¹⁰⁶, H. Y. Cheung¹⁰⁶, H. Y. Chia⁶⁹, F. Chiadini^{94,131}, C.-Y. Chiang¹³², G. Chiarini⁷⁵, R. Chierici¹³³, A. Chincarini⁸², M. L. Chiofalo^{18,71}, A. Chiummo⁴⁰, G. Cho¹³⁴, H. S. Cho¹³⁵, R. K. Choudhary⁸³, S. Choudhary¹¹, N. Christensen⁹², H. Chu¹²⁸, Q. Chu⁸³, Y.-K. Chu¹³², S. Chua⁸, K. W. Chung⁵¹, G. Ciani^{74,75}, P. Ciecielag⁷⁸, M. Cieřlar⁷⁸, M. Cifaldi^{116,117}, A. A. Ciobanu⁸⁰, R. Ciolfi^{75,136}, F. Cipriano⁹², A. Cirone^{82,110}, F. Clara⁶⁴, E. N. Clark¹³⁷, J. A. Clark^{1,104}, L. Clarke¹³⁸, P. Clearwater¹³⁹, S. Clesse¹⁴⁰, F. Cleva⁹², E. Coccia^{29,98}, E. Codazzo²⁹, P.-F. Cohadon⁹⁹, D. E. Cohen³⁹, L. Cohen², M. Colleoni¹⁴¹, C. G. Collette¹⁴², A. Colombo⁶¹, M. Colpi^{61,62}, C. M. Compton⁶⁴, M. Constanco Jr.¹⁶, L. Conti⁷⁵, S. J. Cooper¹⁴, P. Corban⁶, T. R. Corbitt², I. Cordero-Carrión¹⁴³, S. Corezzi^{72,73}, K. R. Corley⁴³, N. Cornish⁷⁶, D. Corre³⁹, A. Corsi¹⁴⁴, S. Cortese⁴⁰, C. A. Costa¹⁶, R. Cotesta¹⁰², M. W. Coughlin⁶⁰, J.-P. Coulon⁹², S. T. Countryman⁴³, B. Cousins¹⁴⁵, P. Couvares¹, D. M. Coward⁸³, M. J. Cowart⁶, D. C. Coyne¹, R. Coyne¹⁴⁶, J. D. E. Creighton⁷, T. D. Creighton¹⁴⁷, A. W. Criswell⁶⁰, M. Croquette⁹⁹, S. G. Crowder¹⁴⁸, J. R. Cudell⁵⁹, T. J. Cullen², A. Cumming⁶⁶, R. Cummings⁶⁶, L. Cunningham⁶⁶, E. Cuomo^{18,40,149}, M. Curyto¹⁰⁰, P. Dabadie²⁴, T. Dal Canton³⁹, S. Dall’Osso²⁹, G. Dálya¹⁵⁰, A. Dana⁷⁰, L. M. DaneshgaranBajastani⁸¹, B. D’Angelo^{82,110}, S. Danilishin^{50,151}, S. D’Antonio¹¹⁷, K. Danzmann^{9,10}, C. Darsow-Fromm¹²¹, A. Dasgupta⁷⁷, L. E. H. Datrier⁶⁶, S. Datta¹¹, V. Dattilo⁴⁰, I. Dave⁸⁴, M. Davies³⁹, G. S. Davies¹⁵², D. Davis¹, M. C. Davis¹¹⁹, E. J. Daw¹⁵³, R. Dean¹¹⁹, D. DeBra⁷⁰, M. Deenadayalan¹¹, J. Degallaix¹⁵⁴, M. De Laurentis^{4,23}, S. Deléglise⁹⁹, V. Del Favero¹²², F. De Lillo⁴⁹, N. De Lillo⁶⁶, W. Del Pozzo^{18,71}, L. M. DeMarchi¹⁵, F. De Matteis^{116,117}, V. D’Emilio¹⁷, N. Demos⁶⁷, T. Dent¹⁰⁵, A. Depasse⁴⁹, R. De Pietri^{155,156}, R. De Rosa^{4,23}, C. De Rossi⁴⁰, R. DeSalvo¹¹⁸, R. De Simone¹³¹, S. Dhurandhar¹¹, M. C. Díaz¹⁴⁷, M. Diaz-Ortiz Jr.⁶⁹, N. A. Didio⁵⁸, T. Dietrich^{50,102}, L. Di Fiore⁴, C. Di Fronzo¹⁴, C. Di Giorgio^{93,94}, F. Di Giovanni¹²⁰, M. Di Giovanni²⁹, T. Di Girolamo^{4,23}, A. Di Lieto^{18,71}, B. Ding¹⁴², S. Di Pace^{48,95}, I. Di Palma^{48,95}, F. Di Renzo^{18,71}, A. K. Divakarla⁶⁹, A. Dmitriev¹⁴, Z. Doctor⁵⁷, L. D’Onofrio^{4,23}, F. Donovan⁶⁷, K. L. Dooley¹⁷, S. Doravari¹¹, I. Dorrington¹⁷, M. Drago^{48,95}, J. C. Driggers⁶⁴, Y. Drori¹, J.-G. Ducoin³⁹, P. Dupej⁶⁶, O. Durante^{93,94}, D. D’Urso^{114,115}, P.-A. Duverne³⁹, S. E. Dwyer⁶⁴, C. Eassa⁶⁴, P. J. Easter⁵, M. Ebersold¹⁵⁷, T. Eckhardt¹²¹, G. Eddolls⁶⁶, B. Edelman⁵⁷, T. B. Edo¹, O. Edy¹⁵², A. Effler⁶, S. Eguchi¹²⁴, J. Eichholz⁸, S. S. Eikenberry⁶⁹, M. Eisenmann²⁸, R. A. Eisenstein⁶⁷, A. Ejlli¹⁷, E. Engelby³⁸, Y. Enomoto²⁵, L. Errico^{4,23}, R. C. Essick¹⁵⁸, H. Estellés¹⁴¹, D. Estevez¹⁵⁹, Z. Etienne¹⁶⁰, T. Etzel¹, M. Evans⁶⁷, T. M. Evans⁶

B. E. Ewing¹⁴⁵, V. Fafone^{29,116,117}, H. Fair⁵⁸, S. Fairhurst¹⁷, A. M. Farah¹⁵⁸, S. Farinon⁸², B. Farr⁵⁷, W. M. Farr^{107,108},
N. W. Farrow⁵, E. J. Fauchon-Jones¹⁷, G. Favaro⁷⁴, M. Favata¹⁶¹, M. Fays⁵⁹, M. Fazio¹⁶², J. Feicht¹, M. M. Fejer⁷⁰,
E. Fenyvesi^{68,163}, D. L. Ferguson¹⁶⁴, A. Fernandez-Galiana⁶⁷, I. Ferrante^{18,71}, T. A. Ferreira¹⁶, F. Fidecaro^{18,71}, P. Figura¹⁰⁰,
I. Fiori⁴⁰, M. Fishbach¹⁵, R. P. Fisher⁵⁴, R. Fittipaldi^{94,165}, V. Fiumara^{94,166}, R. Flaminio^{20,28}, E. Floden⁶⁰, H. Fong²⁶,
J. A. Font^{120,167}, B. Fornal¹⁶⁸, P. W. F. Forsyth⁸, A. Franke¹²¹, S. Frasca^{48,95}, F. Frasconi¹⁸, C. Frederick¹⁶⁹, J. P. Freed³³,
Z. Frei¹⁵⁰, A. Freise¹⁷⁰, R. Frey⁵⁷, P. Fritschel⁶⁷, V. V. Frolov⁶, G. G. Fronzè²², Y. Fujii¹⁷¹, Y. Fujikawa¹⁷², M. Fukunaga³⁵,
M. Fukushima²¹, P. Fulda⁶⁹, M. Fyffe⁶, H. A. Gabbard⁶⁶, B. U. Gadre¹⁰², J. R. Gair¹⁰², J. Gais¹⁰⁶, S. Galaudage⁵, R. Gamba¹³,
D. Ganapathy⁶⁷, A. Ganguly¹⁹, D. Gao¹⁷³, S. G. Gaonkar¹¹, B. Garaventa^{82,110}, C. García-Núñez⁹⁰, C. García-Quirós¹⁴¹,
F. Garufi^{4,23}, B. Gateley⁶⁴, S. Gaudio³³, V. Gayathri⁶⁹, G.-G. Ge¹⁷³, G. Gemme⁸², A. Gennai¹⁸, J. George⁸⁴, O. Gerberding¹²¹,
L. Gergely¹⁷⁴, P. Gewecke¹²¹, S. Ghonge¹⁰⁴, Abhirup Ghosh¹⁰², Archisman Ghosh¹⁷⁵, Shaon Ghosh^{7,161}, Shrobana Ghosh¹⁷,
B. Giacomazzo^{61,62,63}, L. Giacoppo^{48,95}, J. A. Giaime^{2,6}, K. D. Giardino⁶, D. R. Gibson⁹⁰, C. Gier³⁰, M. Giesler¹⁷⁶, P. Giri^{18,71},
F. Gissi⁷⁹, J. Glanzer², A. E. Gleckl³⁸, P. Godwin¹⁴⁵, E. Goetz¹⁷⁷, R. Goetz⁶⁹, N. Gohlke^{9,10}, B. Goncharov^{5,29}, G. González²,
A. Gopakumar¹⁷⁸, M. Gosselin⁴⁰, R. Gouaty²⁸, D. W. Gould⁸, B. Grace⁸, A. Grado^{4,179}, M. Granata¹⁵⁴, V. Granata⁹³, A. Grant⁶⁶,
S. Gras⁶⁷, P. Grassia¹, C. Gray⁶⁴, R. Gray⁶⁶, G. Greco⁷², A. C. Green⁶⁹, R. Green¹⁷, A. M. Gretarsson³³, E. M. Gretarsson³³,
D. Griffith¹, W. Griffiths¹⁷, H. L. Griggs¹⁰⁴, G. Grignani^{72,73}, A. Grimaldi^{88,89}, S. J. Grimm^{29,98}, H. Grote¹⁷, S. Grunewald¹⁰²,
P. Gruning³⁹, D. Guerra¹²⁰, G. M. Guidi^{46,47}, A. R. Guimaraes², G. Guixé²⁷, H. K. Gulati⁷⁷, H.-K. Guo¹⁶⁸, Y. Guo⁵⁰,
Anchal Gupta¹, Anuradha Gupta¹⁸⁰, P. Gupta^{50,111}, E. K. Gustafson¹, R. Gustafson¹⁸¹, F. Guzman¹⁸², S. Ha¹⁸³, L. Haegel³⁴,
A. Hagiwara^{35,184}, S. Haino¹³², O. Halim^{32,185}, E. D. Hall⁶⁷, E. Z. Hamilton¹⁵⁷, G. Hammond⁶⁶, W.-B. Han¹⁸⁶, M. Haney¹⁵⁷,
J. Hanks⁶⁴, C. Hanna¹⁴⁵, M. D. Hannam¹⁷, O. Hannuksela^{50,111}, H. Hansen⁶⁴, T. J. Hansen³³, J. Hanson⁶, T. Harder⁹²,
T. Hardwick², K. Haris^{50,111}, J. Harms^{29,98}, G. M. Harry¹⁸⁷, I. W. Harry¹⁵², D. Hartwig¹²¹, K. Hasegawa³⁵, B. Haskell⁷⁸,
R. K. Hasskew⁶, C.-J. Haster⁶⁷, K. Hattori¹⁸⁸, K. Haughian⁶⁶, H. Hayakawa¹⁸⁹, K. Hayama¹²⁴, F. J. Hayes⁶⁶, J. Healy¹²²,
A. Heidmann⁹⁹, A. Heidt^{9,10}, M. C. Heintze⁶, J. Heinze^{9,10}, J. Heinzl¹⁹⁰, H. Heitmann⁹², F. Hellman¹⁹¹, P. Hello³⁹,
A. F. Helmling-Cornell⁵⁷, G. Hemming⁴⁰, M. Hendry⁶⁶, I. S. Heng⁶⁶, E. Hennes⁵⁰, J. Hennig¹⁹², M. H. Hennig¹⁹²,
A. G. Hernandez⁸¹, F. Hernandez Vivanco⁵, M. Heurs^{9,10}, S. Hild^{50,151}, P. Hill³⁰, Y. Himemoto¹⁹³, A. S. Hines¹⁸², Y. Hiranuma¹⁹⁴,
N. Hirata²⁰, E. Hirose³⁵, S. Hochheim^{9,10}, D. Hofman¹⁵⁴, J. N. Hohmann¹²¹, D. G. Holcomb¹¹⁹, N. A. Holland⁸, I. J. Hollows¹⁵³,
Z. J. Holmes⁸⁰, K. Holt⁶, D. E. Holz¹⁵⁸, Z. Hong¹⁹⁵, P. Hopkins¹⁷, J. Hough⁶⁶, S. Hourihane¹²⁹, E. J. Howell⁸³, C. G. Hoy¹⁷,
D. Hoyland¹⁴, A. Hreibi^{9,10}, B.-H. Hsieh³⁵, Y. Hsu¹²³, G.-Z. Huang¹⁹⁵, H.-Y. Huang¹³², P. Huang¹⁷³, Y.-C. Huang¹³⁰,
Y.-J. Huang¹³², Y. Huang⁶⁷, M. T. Hübner⁵, A. D. Huddart¹³⁸, B. Hughey³³, D. C. Y. Hui¹⁹⁶, V. Hui²⁸, S. Husa¹⁴¹, S. H. Huttner⁶⁶,
R. Huxford¹⁴⁵, T. Huynh-Dinh⁶, S. Ide¹⁹⁷, B. Idzkowski¹⁰⁰, A. Iess^{116,117}, B. Ikenoue²¹, S. Imam¹⁹⁵, K. Inayoshi¹⁹⁸, C. Ingram⁸⁰,
Y. Inoue¹²⁸, K. Ioka¹⁹⁹, M. Isi⁶⁷, K. Isleif¹²¹, K. Ito²⁰⁰, Y. Itoh^{201,202}, B. R. Iyer¹⁹, K. Izumi²⁰³, V. JaberianHamedan⁸³,
T. Jacqmin⁹⁹, S. J. Jadhav²⁰⁴, S. P. Jadhav¹¹, A. L. James¹⁷, A. Z. Jan¹²², K. Jani²⁰⁵, J. Janquart^{50,111}, K. Janssens^{92,206},
N. N. Janthaler²⁰⁴, P. Jaranowski²⁰⁷, D. Jariwala⁶⁹, R. Jaume¹⁴¹, A. C. Jenkins⁵¹, K. Jenner⁸⁰, C. Jeon²⁰⁸, M. Jeunon⁶⁰, W. Jia⁶⁷,
H.-B. Jin^{209,210}, G. R. Johns⁵⁴, A. W. Jones⁸³, D. I. Jones²¹¹, J. D. Jones⁶⁴, P. Jones¹⁴, R. Jones⁶⁶, R. J. G. Jonker⁵⁰, L. Ju⁸³,
P. Jung⁵³, K. Jung¹⁸³, J. Junker^{9,10}, V. Juste¹⁵⁹, K. Kaihotsu²⁰⁰, T. Kajita²¹², M. Kakizaki¹⁸⁸, C. V. Kalaghatgi^{17,111}, V. Kalogera¹⁵,
B. Kamai¹, M. Kamiizumi¹⁸⁹, N. Kanda^{201,202}, S. Kandhasamy¹¹, G. Kang²¹³, J. B. Kanner¹, Y. Kao¹²³, S. J. Kapadia¹⁹,
D. P. Kapasi⁸, S. Karat¹, C. Karathanasis²¹⁴, S. Karki⁸⁶, R. Kashyap¹⁴⁵, M. Kasprzak¹, W. Kastaun^{9,10}, S. Katsanevas⁴⁰,
E. Katsavounidis⁶⁷, W. Katzman⁶, T. Kaur⁸³, K. Kawabe⁶⁴, K. Kawaguchi³⁵, N. Kawai²¹⁵, T. Kawasaki²⁵, F. Kéfélian⁹²,
D. Keitel¹⁴¹, J. S. Key²¹⁶, S. Khadka⁷⁰, F. Y. Khalili⁸⁷, S. Khan¹⁷, E. A. Khazanov²¹⁷, N. Khetan^{29,98}, M. Khurshed⁸⁴,
N. Kijbunchoo⁸, C. Kim²¹⁸, J. C. Kim²¹⁹, J. Kim²²⁰, K. Kim²²¹, W. S. Kim²²², Y.-M. Kim²²³, C. Kimball¹⁵, N. Kimura¹⁸⁴,
M. Kinley-Hanlon⁶⁶, R. Kirchoff^{9,10}, J. S. Kissel⁶⁴, N. Kita²⁵, H. Kitazawa²⁰⁰, L. Kleybolte¹²¹, S. Klimenko⁶⁹, A. M. Knee¹⁷⁷,
T. D. Knowles¹⁶⁰, E. Knyazev⁶⁷, P. Koch^{9,10}, G. Koekoek^{50,151}, Y. Kojima²²⁴, K. Kokeyama²²⁵, S. Koley²⁹, P. Kolitsidou¹⁷,
M. Kolstein²¹⁴, K. Komori^{25,67}, V. Kondrashov¹, A. K. H. Kong²²⁶, A. Kontos²²⁷, N. Koper^{9,10}, M. Korobko¹²¹, K. Kotake¹²⁴,
M. Kovalam⁸³, D. B. Kozak¹, C. Kozakai⁴⁴, R. Kozu¹⁸⁹, V. Kringel^{9,10}, N. V. Krishnendu^{9,10}, A. Królak^{228,229}, G. Kuehn^{9,10},
F. Kuei¹²³, P. Kuijper⁵⁰, A. Kumar²⁰⁴, P. Kumar¹⁷⁶, Rahul Kumar⁶⁴, Rakesh Kumar⁷⁷, J. Kume²⁶, K. Kuns⁶⁷, C. Kuo¹²⁸,
H.-S. Kuo¹⁹⁵, Y. Kuromiya²⁰⁰, S. Kuroyanagi^{230,231}, K. Kusayanagi²¹⁵, S. Kuwahara²⁶, K. Kwak¹⁸³, P. Lagabbe²⁸, D. Laghi^{18,71},
E. Lalande²³², T. L. Lam¹⁰⁶, A. Lamberts^{92,233}, M. Landry⁶⁴, B. B. Lane⁶⁷, R. N. Lang⁶⁷, J. Lange¹⁶⁴, B. Lantz⁷⁰, I. La Rosa²⁸,
A. Lartaux-Vollard³⁹, P. D. Lasky⁵, M. Laxen⁶, A. Lazzarini¹, C. Lazzaro^{74,75}, P. Leaci^{48,95}, S. Leavey^{9,10}, Y. K. Lecoeuche¹⁷⁷,
H. K. Lee²³⁴, H. M. Lee¹³⁴, H. W. Lee²¹⁹, J. Lee¹³⁴, K. Lee²³⁵, R. Lee¹³⁰, J. Lehmann^{9,10}, A. Lemaître²³⁶, M. Leonardi²⁰,
N. Leroy³⁹, N. Letendre²⁸, C. Levesque²³², Y. Levin⁵, J. N. Leviton¹⁸¹, K. Leyde³⁴, A. K. Y. Li¹, B. Li¹²³, J. Li¹⁵, K. L. Li²³⁷,
T. G. F. Li¹⁰⁶, X. Li¹²⁹, C.-Y. Lin²³⁸, F.-K. Lin¹³², F.-L. Lin¹⁹⁵, H. L. Lin¹²⁸, L. C.-C. Lin¹⁸³, F. Linde^{50,239}, S. D. Linker⁸¹,
J. N. Linley⁶⁶, T. B. Littenberg²⁴⁰, G. C. Liu¹²⁶, J. Liu^{9,10}, K. Liu¹²³, X. Liu⁷, F. Llamas¹⁴⁷, M. Llorens-Monteagudo¹²⁰,
R. K. L. Lo¹, A. Lockwood²⁴¹, L. T. London⁶⁷, A. Longo^{242,243}, D. Lopez¹⁵⁷, M. Lopez Portilla¹¹¹, M. Lorenzini^{116,117},
V. Lorient²⁴⁴, M. Lormand⁶, G. Losurdo¹⁸, T. P. Lott¹⁰⁴, J. D. Lough^{9,10}, C. O. Lousto¹²², G. Lovelace³⁸, J. F. Lucaccioni¹⁶⁹,
H. Lück^{9,10}, D. Lumaca^{116,117}, A. P. Lundgren¹⁵², L.-W. Luo¹³², J. E. Lynam⁵⁴, R. Macas¹⁵², M. MacInnis⁶⁷, D. M. Macleod¹⁷,
I. A. O. MacMillan¹, A. Macquet⁹², I. Magaña Hernandez⁷, C. Magazzù¹⁸, R. M. Magee¹, R. Maggiore¹⁴, M. Magnozzi^{82,110},
S. Mahesh¹⁶⁰, E. Majorana^{48,95}, C. Makarem¹, I. Maksimovic²⁴⁴, S. Maliakal¹, A. Malik⁸⁴, N. Man⁹², V. Mandic⁶⁰,
V. Mangano^{48,95}, J. L. Mango²⁴⁵, G. L. Mansell^{64,67}, M. Manske⁷, M. Mantovani⁴⁰, M. Mapelli^{74,75}, F. Marchesoni^{72,246,247},

M. Marchio²⁰, F. Marion²⁸, Z. Mark¹²⁹, S. Márka⁴³, Z. Márka⁴³, C. Markakis¹², A. S. Markosyan⁷⁰, A. Markowitz¹, E. Maros¹, A. Marquina¹⁴³, S. Marsat³⁴, F. Martelli^{46,47}, I. W. Martin⁶⁶, R. M. Martin¹⁶¹, M. Martinez²¹⁴, V. A. Martinez⁶⁹, V. Martinez²⁴, K. Martinovic⁵¹, D. V. Martynov¹⁴, E. J. Marx⁶⁷, H. Masalehdan¹²¹, K. Mason⁶⁷, E. Massera¹⁵³, A. Masserot²⁸, T. J. Massinger⁶⁷, M. Masso-Reid⁶⁶, S. Mastrogiovanni³⁴, A. Matas¹⁰², M. Mateu-Lucena¹⁴¹, F. Matichard^{1,67}, M. Matushechkina^{9,10}, N. Mavalvala⁶⁷, J. J. McCann⁸³, R. McCarthy⁶⁴, D. E. McClelland⁸, P. K. McClincy¹⁴⁵, S. McCormick⁶, L. McCuller⁶⁷, G. I. McGhee⁶⁶, S. C. McGuire²⁴⁸, C. McIsaac¹⁵², J. McIver¹⁷⁷, T. McRae⁸, S. T. McWilliams¹⁶⁰, D. Meacher⁷, M. Mehmet^{9,10}, A. K. Mehta¹⁰², Q. Meijer¹¹¹, A. Melatos¹¹³, D. A. Melchor³⁸, G. Mendell⁶⁴, A. Menendez-Vazquez²¹⁴, C. S. Menoni¹⁶², R. A. Mercer⁷, L. Mereni¹⁵⁴, K. Merfeld⁵⁷, E. L. Merilh⁶, J. D. Merritt⁵⁷, M. Merzougui⁹², S. Meshkov^{1,314}, C. Messenger⁶⁶, C. Messick¹⁶⁴, P. M. Meyers¹¹³, F. Meylahn^{9,10}, A. Mhaske¹¹, A. Miani^{88,89}, H. Miao¹⁴, I. Michaloliakos⁶⁹, C. Michel¹⁵⁴, Y. Michimura²⁵, H. Middleton¹¹³, L. Milano²³, A. L. Miller⁴⁹, A. Miller⁸¹, B. Miller^{50,85}, M. Millhouse¹¹³, J. C. Mills¹⁷, E. Milotti^{32,185}, O. Minazzoli^{92,249}, Y. Minenkov¹¹⁷, N. Mio²⁵⁰, Li. M. Mir²¹⁴, M. Miravet-Tenés¹²⁰, C. Mishra²⁵¹, T. Mishra⁶⁹, T. Mistry¹⁵³, S. Mitra¹¹, V. P. Mitrofanov⁸⁷, G. Mitselmakher⁶⁹, R. Mittleman⁶⁷, O. Miyakawa¹⁸⁹, A. Miyamoto²⁰¹, Y. Miyazaki²⁵, K. Miyo¹⁸⁹, S. Miyoki¹⁸⁹, Geoffrey Mo⁶⁷, E. Moguel¹⁶⁹, K. Mogushi⁸⁶, S. R. P. Mohapatra⁶⁷, S. R. Mohite⁷, I. Molina³⁸, M. Molina-Ruiz¹⁹¹, M. Mondin⁸¹, M. Montani^{46,47}, C. J. Moore¹⁴, D. Moraru⁶⁴, F. Morawski⁷⁸, A. More¹¹, C. Moreno³³, G. Moreno⁶⁴, Y. Mori²⁰⁰, S. Morisaki⁷, Y. Moriwaki¹⁸⁸, B. Mours¹⁵⁹, C. M. Mow-Lowry^{14,170}, S. Mozzon¹⁵², F. Muciaccia^{48,95}, Arunava Mukherjee²⁵², D. Mukherjee¹⁴⁵, Soma Mukherjee¹⁴⁷, Subroto Mukherjee⁷⁷, Suvodip Mukherjee⁸⁵, N. Mukund^{9,10}, A. Mullavey⁶, J. Munch⁸⁰, E. A. Muñoz⁵⁸, P. G. Murray⁶⁶, R. Musenich^{82,110}, S. Muusse⁸⁰, S. L. Nadji^{9,10}, K. Nagano²⁰³, S. Nagano²⁵³, A. Nagar^{22,254}, K. Nakamura²⁰, H. Nakano²⁵⁵, M. Nakano³⁵, R. Nakashima²¹⁵, Y. Nakayama²⁰⁰, V. Napolano⁴⁰, I. Nardecchia^{116,117}, T. Narikawa³⁵, L. Naticchioni⁴⁸, B. Nayak⁸¹, R. K. Nayak²⁵⁶, R. Negishi¹⁹⁴, B. F. Neil⁸³, J. Neilson^{79,94}, G. Nelemans²⁵⁷, T. J. N. Nelson⁶, M. Nery^{9,10}, P. Neubauer¹⁶⁹, A. Neunzert²¹⁶, K. Y. Ng⁶⁷, S. W. S. Ng⁸⁰, C. Nguyen³⁴, P. Nguyen⁵⁷, T. Nguyen⁶⁷, L. Nguyen Quynh²⁵⁸, W.-T. Ni^{130,173,209}, S. A. Nichols², A. Nishizawa²⁶, S. Nissanke^{50,85}, E. Nitoglia¹³³, F. Nocera⁴⁰, M. Norman¹⁷, C. North¹⁷, S. Nozaki¹⁸⁸, L. K. Nuttall¹⁵², J. Oberling⁶⁴, B. D. O'Brien⁶⁹, Y. Obuchi²¹, J. O'Dell¹³⁸, E. Oelker⁶⁶, W. Ogaki³⁵, G. Oganessian^{29,98}, J. J. Oh²²², K. Oh¹⁹⁶, S. H. Oh²²², M. Ohashi¹⁸⁹, N. Ohishi⁴⁴, M. Ohkawa¹⁷², F. Ohme^{9,10}, H. Ohta²⁶, M. A. Okada¹⁶, Y. Okutani¹⁹⁷, K. Okutomi¹⁸⁹, C. Olivetto⁴⁰, K. Oohara¹⁹⁴, C. Ooi²⁵, R. Oram⁶, B. O'Reilly⁶, R. G. Ormiston⁶⁰, N. D. Ormsby⁵⁴, L. F. Ortega⁶⁹, R. O'Shaughnessy¹²², E. O'Shea¹⁷⁶, S. Oshino¹⁸⁹, S. Ossokine¹⁰², C. Osthelder¹, S. Otabe²¹⁵, D. J. Ottaway⁸⁰, H. Overmier⁶, A. E. Pace¹⁴⁵, G. Pagano^{18,71}, M. A. Page⁸³, G. Pagliaroli^{29,98}, A. Pai⁹⁷, S. A. Pai⁸⁴, J. R. Palamos⁵⁷, O. Palashov²¹⁷, C. Palomba⁴⁸, H. Pan¹²³, K. Pan^{130,226}, P. K. Panda²⁰⁴, H. Pang¹²⁸, P. T. H. Pang^{50,111}, C. Pankow¹⁵, F. Pannarale^{48,95}, B. C. Pant⁸⁴, F. H. Panther⁸³, F. Paoletti¹⁸, A. Paoli⁴⁰, A. Paolone^{48,259}, A. Parisi¹²⁶, H. Park⁷, J. Park²⁶⁰, W. Parker^{6,248}, D. Pascucci⁵⁰, A. Pasqualetti⁴⁰, R. Passaquieti^{18,71}, D. Passuello¹⁸, M. Patel⁵⁴, M. Pathak⁸⁰, B. Patricelli^{18,40}, A. S. Patron², S. Patrone^{48,95}, S. Paul⁵⁷, E. Payne⁵, M. Pedraza¹, M. Pegoraro⁷⁵, A. Pele⁶, F. E. Peña Arellano¹⁸⁹, S. Penn²⁶¹, A. Perego^{88,89}, A. Pereira²⁴, T. Pereira²⁶², C. J. Perez⁶⁴, C. Périgois²⁸, C. C. Perkins⁶⁹, A. Perreca^{88,89}, S. Perriès¹³³, J. Petermann¹²¹, D. Petterson¹, H. P. Pfeiffer¹⁰², K. A. Pham⁶⁰, K. S. Phukon^{50,239}, O. J. Piccinni⁴⁸, M. Pichot⁹², M. Piendibene^{18,71}, F. Piergiovanni^{46,47}, L. Pierini^{48,95}, V. Pierro^{79,94}, G. Pillant⁴⁰, M. Pillas³⁹, F. Pilo¹⁸, L. Pinard¹⁵⁴, I. M. Pinto^{79,94,263}, M. Pinto⁴⁰, B. J. Piotrkowski⁷, K. Piotrkowski⁴⁹, M. Pirello⁶⁴, M. D. Pitkin²⁶⁴, E. Placidi^{48,95}, L. Planas¹⁴¹, W. Plastino^{242,243}, C. Pluchar¹³⁷, R. Poggiani^{18,71}, E. Polini²⁸, D. Y. T. Pong¹⁰⁶, S. Ponrathnam¹¹, P. Popolizio⁴⁰, E. K. Porter³⁴, R. Poulton⁴⁰, J. Powell¹³⁹, M. Pracchia²⁸, T. Pradier¹⁵⁹, A. K. Prajapati⁷⁷, K. Prasai⁷⁰, R. Prasanna²⁰⁴, G. Pratten¹⁴, M. Principe^{79,94,263}, G. A. Prodi^{89,265}, L. Prokhorov¹⁴, P. Proposito^{116,117}, L. Prudenzi¹⁰², A. Puecher^{50,111}, M. Punturo⁷², F. Puosi^{18,71}, P. Puppo⁴⁸, M. Pürner¹⁰², H. Qi¹⁷, V. Quetschke¹⁴⁷, R. Quitzow-James⁸⁶, F. J. Raab⁶⁴, G. Raaijmakers^{50,85}, H. Radkins⁶⁴, N. Radulesco⁹², P. Raffai¹⁵⁰, S. X. Rail²³², S. Raja⁸⁴, C. Rajan⁸⁴, K. E. Ramirez⁶, T. D. Ramirez³⁸, A. Ramos-Buades¹⁰², J. Rana¹⁴⁵, P. Rapagnani^{48,95}, U. D. Rapol²⁶⁶, A. Ray⁷, V. Raymond¹⁷, N. Raza¹⁷⁷, M. Razzano^{18,71}, J. Read³⁸, L. A. Rees¹⁸⁷, T. Regimbau²⁸, L. Rei⁸², S. Reid³⁰, S. W. Reid⁵⁴, D. H. Reitze^{1,69}, P. Relton¹⁷, A. Renzini¹, P. Rettegno^{22,267}, M. Rezac³⁸, F. Ricci^{48,95}, D. Richards¹³⁸, J. W. Richardson¹, L. Richardson¹⁸², G. Riemschneider^{22,267}, K. Riles¹⁸¹, S. Rinaldi^{18,71}, K. Rink¹⁷⁷, M. Rizzo¹⁵, N. A. Robertson^{1,66}, R. Robie¹, F. Robinet³⁹, A. Rocchi¹¹⁷, S. Rodriguez³⁸, L. Rolland²⁸, J. G. Rollins¹, M. Romanelli⁹⁶, R. Romano^{3,4}, C. L. Romel⁶⁴, A. Romero-Rodríguez²¹⁴, I. M. Romero-Shaw⁵, J. H. Romie⁶, S. Ronchini^{29,98}, L. Rosa^{4,23}, C. A. Rose⁷, D. Rosińska¹⁰⁰, M. P. Ross²⁴¹, S. Rowan⁶⁶, S. J. Rowlinson¹⁴, S. Roy¹¹¹, Santosh Roy¹¹, Soumen Roy²⁶⁸, D. Rozza^{114,115}, P. Ruggi⁴⁰, K. Ryan⁶⁴, S. Sachdev¹⁴⁵, T. Sadecki⁶⁴, J. Sadiq¹⁰⁵, N. Sago²⁶⁹, S. Saito²¹, Y. Saito¹⁸⁹, K. Sakai²⁷⁰, Y. Sakai¹⁹⁴, M. Sakellariadou⁵¹, Y. Sakuno¹²⁴, O. S. Salafia^{61,62,63}, L. Salconi⁴⁰, M. Saleem⁶⁰, F. Salemi^{88,89}, A. Samajdar^{50,111}, E. J. Sanchez¹, J. H. Sanchez³⁸, L. E. Sanchez¹, N. Sanchis-Gual²⁷¹, J. R. Sanders²⁷², A. Sanuy²⁷, T. R. Saravanan¹¹, N. Sarin⁵, B. Sassolas¹⁵⁴, H. Satari⁸³, S. Sato²⁷³, T. Sato¹⁷², O. Sauter⁶⁹, R. L. Savage⁶⁴, T. Sawada²⁰¹, D. Sawant⁹⁷, H. L. Sawant¹¹, S. Sayah¹⁵⁴, D. Schaetzel¹, M. Scheel¹²⁹, J. Scheuer¹⁵, M. Schiworski⁸⁰, P. Schmidt¹⁴, S. Schmidt¹¹¹, R. Schnabel¹²¹, M. Schneewind^{9,10}, R. M. S. Schofield⁵⁷, A. Schönbeck¹²¹, B. W. Schulte^{9,10}, B. F. Schutz^{9,10,17}, E. Schwartz¹⁷, J. Scott⁶⁶, S. M. Scott⁸, M. Seglar-Arroyo²⁸, T. Sekiguchi²⁶, Y. Sekiguchi²⁷⁴, D. Sellers⁶, A. S. Sengupta²⁶⁸, D. Sentenac⁴⁰, E. G. Seo¹⁰⁶, V. Sequino^{4,23}, A. Sergeev²¹⁷, Y. Setyawati¹¹¹, T. Shaffer⁶⁴, M. S. Shahriar¹⁵, B. Shams¹⁶⁸, L. Shao¹⁹⁸, A. Sharma^{29,98}, P. Sharma⁸⁴, P. Shawhan¹⁰¹, N. S. Shcheblanov²³⁶, S. Shibagaki¹²⁴, M. Shikauchi²⁶, R. Shimizu²¹, T. Shimoda²⁵, K. Shimode¹⁸⁹, H. Shinkai²⁷⁵, T. Shishido⁴⁵, A. Shoda²⁰, D. H. Shoemaker⁶⁷, D. M. Shoemaker¹⁶⁴, S. ShyamSundar⁸⁴, M. Sieniawska¹⁰⁰, D. Sigg⁶⁴, L. P. Singer¹⁰⁹, D. Singh¹⁴⁵, N. Singh¹⁰⁰, A. Singha^{50,151}, A. M. Sintes¹⁴¹, V. Sipala^{114,115}, V. Skliris¹⁷, B. J. J. Slagmolen⁸, T. J. Slaven-Blair⁸³, J. Smetana¹⁴, J. R. Smith³⁸, R. J. E. Smith⁵,

J. Soldateschi^{47,276,277}, S. N. Somala²⁷⁸, K. Somiya²¹⁵, E. J. Son²²², K. Soni¹¹, S. Soni², V. Sordini¹³³, F. Sorrentino⁸², N. Sorrentino^{18,71}, H. Sotani²⁷⁹, R. Soulard⁹², T. Souradeep^{11,266}, E. Sowell¹⁴⁴, V. Spagnuolo^{50,151}, A. P. Spencer⁶⁶, M. Spera^{74,75}, R. Srinivasan⁹², A. K. Srivastava⁷⁷, V. Srivastava⁵⁸, K. Staats¹⁵, C. Stachie⁹², D. A. Steer³⁴, J. Steinlechner^{50,151}, S. Steinlechner^{50,151}, D. J. Stops¹⁴, M. Stover¹⁶⁹, K. A. Strain⁶⁶, L. C. Strang¹¹³, G. Stratta^{47,280}, A. Strunk⁶⁴, R. Sturani²⁶², A. L. Stuver¹¹⁹, S. Sudhagar¹¹, V. Sudhir⁶⁷, R. Sugimoto^{203,281}, H. G. Suh⁷, T. Z. Summerscales²⁸², H. Sun⁸³, L. Sun⁸, S. Sunil⁷⁷, A. Sur⁷⁸, J. Suresh^{26,35}, P. J. Sutton¹⁷, Takamasa Suzuki¹⁷², Toshikazu Suzuki³⁵, B. L. Swinkels⁵⁰, M. J. Szczepańczyk⁶⁹, P. Szewczyk¹⁰⁰, M. Tacca⁵⁰, H. Tagoshi³⁵, S. C. Tait⁶⁶, H. Takahashi²⁸³, R. Takahashi²⁰, A. Takamori³⁷, S. Takano²⁵, H. Takeda²⁵, M. Takeda²⁰¹, C. J. Talbot³⁰, C. Talbot¹, H. Tanaka²⁸⁴, Kazuyuki Tanaka²⁰¹, Kenta Tanaka²⁸⁴, Taiki Tanaka³⁵, Takahiro Tanaka²⁶⁹, A. J. Tanasijczuk⁴⁹, S. Tanioka^{20,45}, D. B. Tanner⁶⁹, D. Tao¹, L. Tao⁶⁹, E. N. Tapia San Martín²⁰, E. N. Tapia San Martín⁵⁰, C. Taranto¹¹⁶, J. D. Tasson¹⁹⁰, S. Telada²⁸⁵, R. Tenorio¹⁴¹, J. E. Terhune¹¹⁹, L. Terkowski¹²¹, M. P. Thirugnanasambandam¹¹, M. Thomas⁶, P. Thomas⁶⁴, J. E. Thompson¹⁷, S. R. Thondapu⁸⁴, K. A. Thorne⁶, E. Thrane⁵, Shubhanshu Tiwari¹⁵⁷, Srishti Tiwari¹¹, V. Tiwari¹⁷, A. M. Toivonen⁶⁰, K. Toland⁶⁶, A. E. Tolley¹⁵², T. Tomaru²⁰, Y. Tomigami²⁰¹, T. Tomura¹⁸⁹, M. Tonelli^{18,71}, A. Torres-Forné¹²⁰, C. I. Torrie¹, I. Tosta e Melo^{114,115}, D. Töyrä⁸, A. Trapananti^{72,246}, F. Traverso^{72,246}, G. Traylor⁶, M. Trevor¹⁰¹, M. C. Tringali⁴⁰, A. Tripathee¹⁸¹, L. Troiano^{94,286}, A. Trovato³⁴, L. Trozzo^{4,189}, R. J. Trudeau¹, D. S. Tsai¹²³, D. Tsai¹²³, K. W. Tsang^{50,111,287}, T. Tsang²⁸⁸, J.-S. Tsao¹⁹⁵, M. Tse⁶⁷, R. Tso¹²⁹, K. Tsubono²⁵, S. Tsuchida²⁰¹, L. Tsukada²⁶, D. Tsuna²⁶, T. Tsutsui²⁶, T. Tsuzuki²¹, K. Turbang^{206,289}, M. Turconi⁹², D. Tuyenbayev²⁰¹, A. S. Ubhi¹⁴, N. Uchikata³⁵, T. Uchiyama¹⁸⁹, R. P. Udall¹, A. Ueda¹⁸⁴, T. Uehara^{290,291}, K. Ueno²⁶, G. Ueshima²⁹², C. S. Unnikrishnan¹⁷⁸, F. Uraguchi²¹, A. L. Urban², T. Ushiba¹⁸⁹, A. Utina^{50,151}, H. Vahlbruch^{9,10}, G. Vajente¹, A. Vajpeyi⁵, G. Valdes¹⁸², M. Valentini^{88,89}, V. Valsan⁷, N. van Bakel⁵⁰, M. van Beuzekom⁵⁰, J. F. J. van den Brand^{50,151,293}, C. Van Den Broeck^{50,111}, D. C. Vander-Hyde⁵⁸, L. van der Schaaf⁵⁰, J. V. van Heijningen⁴⁹, J. Vanosky¹, M. H. P. M. van Putten²⁹⁴, N. van Remortel²⁰⁶, M. Vardaro^{50,239}, A. F. Vargas¹¹³, V. Varma¹⁷⁶, M. Vasúth⁶⁸, A. Vecchio¹⁴, G. Vedovato⁷⁵, J. Veitch⁶⁶, P. J. Veitch⁸⁰, J. Venneberg^{9,10}, G. Venugopalan¹, D. Verkindt²⁸, P. Verma²²⁹, Y. Verma⁸⁴, D. Veske⁴³, F. Vetrano⁴⁶, A. Vicere^{46,47}, S. Vidyant⁵⁸, A. D. Viets²⁴⁵, A. Vijaykumar¹⁹, V. Villa-Ortega¹⁰⁵, J.-Y. Vinet⁹², A. Virtuoso^{32,185}, S. Vitale⁶⁷, T. Vo⁵⁸, H. Vocca^{72,73}, E. R. G. von Reis⁶⁴, J. S. A. von Wrangel^{9,10}, C. Vorvick⁶⁴, S. P. Vyatchanin⁸⁷, L. E. Wade¹⁶⁹, M. Wade¹⁶⁹, K. J. Wagner¹²², R. C. Walet⁵⁰, M. Walker⁵⁴, G. S. Wallace³⁰, L. Wallace¹, S. Walsh⁷, J. Wang¹⁷³, J. Z. Wang¹⁸¹, W. H. Wang¹⁴⁷, R. L. Ward⁸, J. Warner⁶⁴, M. Was²⁸, T. Washimi²⁰, N. Y. Washington¹, K. Watada⁵⁴, J. Watchi¹⁴², B. Weaver⁶⁴, S. A. Webster⁶⁶, M. Weinert^{9,10}, A. J. Weinstein¹, R. Weiss⁶⁷, C. M. Weller²⁴¹, F. Wellmann^{9,10}, L. Wen⁸³, P. Weßels^{9,10}, K. Wette⁸, J. T. Whelan¹²², D. D. White³⁸, B. F. Whiting⁶⁹, C. Whittle⁶⁷, D. Wilken^{9,10}, D. Williams⁶⁶, M. J. Williams⁶⁶, A. R. Williamson¹⁵², J. L. Willis¹, B. Willke^{9,10}, D. J. Wilson¹³⁷, W. Winkler^{9,10}, C. C. Wipf¹, T. Wlodarczyk¹⁰², G. Woan⁶⁶, J. Woehler^{9,10}, J. K. Wofford¹²², I. C. F. Wong¹⁰⁶, C. Wu¹³⁰, D. S. Wu^{9,10}, H. Wu¹³⁰, S. Wu¹³⁰, D. M. Wysocki⁷, L. Xiao¹, W.-R. Xu¹⁹⁵, T. Yamada²⁸⁴, H. Yamamoto¹, Kazuhiro Yamamoto¹⁸⁸, Kohei Yamamoto²⁸⁴, T. Yamamoto¹⁸⁹, K. Yamashita²⁰⁰, R. Yamazaki¹⁹⁷, F. W. Yang¹⁶⁸, L. Yang¹⁶², Y. Yang²⁹⁵, Yang Yang⁶⁹, Z. Yang⁶⁰, M. J. Yap⁸, D. W. Yeeles¹⁷, A. B. Yelikar¹²², M. Ying¹²³, K. Yokogawa²⁰⁰, J. Yokoyama^{25,26}, T. Yokozawa¹⁸⁹, J. Yoo¹⁷⁶, T. Yoshioka²⁰⁰, Hang Yu¹²⁹, Haocun Yu⁶⁷, H. Yuzurihara³⁵, A. Zadrożny²²⁹, M. Zanolin³³, S. Zeidler²⁹⁶, T. Zelenova⁴⁰, J.-P. Zendri⁷⁵, M. Zevin¹⁵⁸, M. Zhan¹⁷³, H. Zhang¹⁹⁵, J. Zhang⁸³, L. Zhang¹, T. Zhang¹⁴, Y. Zhang¹⁸², C. Zhao⁸³, G. Zhao¹⁴², Y. Zhao²⁰, Yue Zhao¹⁶⁸, R. Zhou¹⁹¹, Z. Zhou¹⁵, X. J. Zhu⁵, Z.-H. Zhu¹¹², A. B. Zimmerman¹⁶⁴, M. E. Zucker^{1,67}, J. Zweizig¹, M. Bhardwaj^{297,298}, P. J. Boyle^{297,298}, T. Cassanelli^{299,300}, F. Dong³⁰¹, E. Fonseca^{302,303}, V. Kaspi^{297,298}, C. Leung^{304,305}, K. W. Masui^{304,305}, B. W. Meyers³⁰¹, D. Michilli^{304,305}, C. Ng³⁰⁰, A. B. Pearlman^{297,298,306,315,316}, E. Petroff^{297,298,307}, Z. Pleunis³⁰⁰, M. Rafei-Ravandi^{297,308,309}, M. Rahman³¹⁰, S. Ransom³¹¹, P. Scholz³⁰⁰, K. Shin^{304,305}, K. Smith³⁰⁸, I. Stairs³⁰¹, S. P. Tendulkar^{312,313}, A. V. Zwaniga^{297,298}

The LIGO Scientific Collaboration,

The Virgo Collaboration,

The KAGRA Collaboration,

and

The CHIME/FRB Collaboration

¹ LIGO Laboratory, California Institute of Technology, Pasadena, CA 91125, USA; lsc-spokesperson@ligo.org, virgo-spokesperson@ego-gw.it, hisaaki.shinkai@oit.ac.jp

² Louisiana State University, Baton Rouge, LA 70803, USA

³ Dipartimento di Farmacia, Università di Salerno, I-84084 Fisciano, Salerno, Italy

⁴ INFN, Sezione di Napoli, Complesso Universitario di Monte S. Angelo, I-80126 Napoli, Italy

⁵ OzGrav, School of Physics & Astronomy, Monash University, Clayton 3800, Victoria, Australia

⁶ LIGO Livingston Observatory, Livingston, LA 70754, USA

⁷ University of Wisconsin-Milwaukee, Milwaukee, WI 53201, USA

⁸ OzGrav, Australian National University, Canberra, Australian Capital Territory 0200, Australia

⁹ Max Planck Institute for Gravitational Physics (Albert Einstein Institute), D-30167 Hannover, Germany

¹⁰ Leibniz Universität Hannover, D-30167 Hannover, Germany

¹¹ Inter-University Centre for Astronomy and Astrophysics, Pune 411007, India

¹² University of Cambridge, Cambridge CB2 1TN, UK

¹³ Theoretisch-Physikalisches Institut, Friedrich-Schiller-Universität Jena, D-07743 Jena, Germany

¹⁴ University of Birmingham, Birmingham B15 2TT, UK

- ¹⁵ Center for Interdisciplinary Exploration & Research in Astrophysics (CIERA), Northwestern University, Evanston, IL 60208, USA
- ¹⁶ Instituto Nacional de Pesquisas Espaciais, 12227-010 São José dos Campos, São Paulo, Brazil
- ¹⁷ Gravity Exploration Institute, Cardiff University, Cardiff CF24 3AA, UK
- ¹⁸ INFN, Sezione di Pisa, I-56127 Pisa, Italy
- ¹⁹ International Centre for Theoretical Sciences, Tata Institute of Fundamental Research, Bengaluru 560089, India
- ²⁰ Gravitational Wave Science Project, National Astronomical Observatory of Japan (NAOJ), Mitaka City, Tokyo 181-8588, Japan
- ²¹ Advanced Technology Center, National Astronomical Observatory of Japan (NAOJ), Mitaka City, Tokyo 181-8588, Japan
- ²² INFN, Sezione di Torino, I-10125 Torino, Italy
- ²³ Università di Napoli “Federico II,” Complesso Universitario di Monte S. Angelo, I-80126 Napoli, Italy
- ²⁴ Université de Lyon, Université Claude Bernard Lyon 1, CNRS, Institut Lumière Matière, F-69622 Villeurbanne, France
- ²⁵ Department of Physics, The University of Tokyo, Bunkyo-ku, Tokyo 113-0033, Japan
- ²⁶ Research Center for the Early Universe (RESCEU), The University of Tokyo, Bunkyo-ku, Tokyo 113-0033, Japan
- ²⁷ Institut de Ciències del Cosmos (ICCB), Universitat de Barcelona, C/ Martí i Franquès 1, Barcelona, E-08028, Spain
- ²⁸ Laboratoire d’Annecy de Physique des Particules (LAPP), Univ. Grenoble Alpes, Université Savoie Mont Blanc, CNRS/IN2P3, F-74941 Annecy, France
- ²⁹ Gran Sasso Science Institute (GSSI), I-67100 L’Aquila, Italy
- ³⁰ SUPA, University of Strathclyde, Glasgow G1 1XQ, UK
- ³¹ Dipartimento di Scienze Matematiche, Informatiche e Fisiche, Università di Udine, I-33100 Udine, Italy
- ³² INFN, Sezione di Trieste, I-34127 Trieste, Italy
- ³³ Embry-Riddle Aeronautical University, Prescott, AZ 86301, USA
- ³⁴ Université de Paris, CNRS, Astroparticule et Cosmologie, F-75006 Paris, France
- ³⁵ Institute for Cosmic Ray Research (ICRR), KAGRA Observatory, The University of Tokyo, Kashiwa City, Chiba 277-8582, Japan
- ³⁶ Accelerator Laboratory, High Energy Accelerator Research Organization (KEK), Tsukuba City, Ibaraki 305-0801, Japan
- ³⁷ Earthquake Research Institute, The University of Tokyo, Bunkyo-ku, Tokyo 113-0032, Japan
- ³⁸ California State University Fullerton, Fullerton, CA 92831, USA
- ³⁹ Université Paris-Saclay, CNRS/IN2P3, IJCLab, F-91405 Orsay, France
- ⁴⁰ European Gravitational Observatory (EGO), I-56021 Cascina, Pisa, Italy
- ⁴¹ Chennai Mathematical Institute, Chennai 603103, India
- ⁴² Department of Mathematics and Physics, Gravitational Wave Science Project, Hirosaki University, Hirosaki City, Aomori 036-8561, Japan
- ⁴³ Columbia University, New York, NY 10027, USA
- ⁴⁴ Kamioka Branch, National Astronomical Observatory of Japan (NAOJ), Kamioka-cho, Hida City, Gifu 506-1205, Japan
- ⁴⁵ The Graduate University for Advanced Studies (SOKENDAI), Mitaka City, Tokyo 181-8588, Japan
- ⁴⁶ Università degli Studi di Urbino “Carlo Bo.,” I-61029 Urbino, Italy
- ⁴⁷ INFN, Sezione di Firenze, I-50019 Sesto Fiorentino, Firenze, Italy
- ⁴⁸ INFN, Sezione di Roma, I-00185 Roma, Italy
- ⁴⁹ Université catholique de Louvain, B-1348 Louvain-la-Neuve, Belgium
- ⁵⁰ Nikhef, Science Park 105, 1098 XG Amsterdam, The Netherlands
- ⁵¹ King’s College London, University of London, London WC2R 2LS, UK
- ⁵² Korea Institute of Science and Technology Information (KISTI), Yuseong-gu, Daejeon 34141, Republic of Korea
- ⁵³ National Institute for Mathematical Sciences, Yuseong-gu, Daejeon 34047, Republic of Korea
- ⁵⁴ Christopher Newport University, Newport News, VA 23606, USA
- ⁵⁵ International College, Osaka University, Toyonaka City, Osaka 560-0043, Japan
- ⁵⁶ School of High Energy Accelerator Science, The Graduate University for Advanced Studies (SOKENDAI), Tsukuba City, Ibaraki 305-0801, Japan
- ⁵⁷ University of Oregon, Eugene, OR 97403, USA
- ⁵⁸ Syracuse University, Syracuse, NY 13244, USA
- ⁵⁹ Université de Liège, B-4000 Liège, Belgium
- ⁶⁰ University of Minnesota, Minneapolis, MN 55455, USA
- ⁶¹ Università degli Studi di Milano-Bicocca, I-20126 Milano, Italy
- ⁶² INFN, Sezione di Milano-Bicocca, I-20126 Milano, Italy
- ⁶³ INAF, Osservatorio Astronomico di Brera sede di Merate, I-23807 Merate, Lecco, Italy
- ⁶⁴ LIGO Hanford Observatory, Richland, WA 99352, USA
- ⁶⁵ Dipartimento di Medicina, Chirurgia e Odontoiatria “Scuola Medica Salernitana,” Università di Salerno, I-84081 Baronissi, Salerno, Italy
- ⁶⁶ SUPA, University of Glasgow, Glasgow G12 8QQ, UK
- ⁶⁷ LIGO Laboratory, Massachusetts Institute of Technology, Cambridge, MA 02139, USA
- ⁶⁸ Wigner RCP, RMKI, H-1121 Budapest, Konkoly Thege Miklós út 29-33, Hungary
- ⁶⁹ University of Florida, Gainesville, FL 32611, USA
- ⁷⁰ Stanford University, Stanford, CA 94305, USA
- ⁷¹ Università di Pisa, I-56127 Pisa, Italy
- ⁷² INFN, Sezione di Perugia, I-06123 Perugia, Italy
- ⁷³ Università di Perugia, I-06123 Perugia, Italy
- ⁷⁴ Università di Padova, Dipartimento di Fisica e Astronomia, I-35131 Padova, Italy
- ⁷⁵ INFN, Sezione di Padova, I-35131 Padova, Italy
- ⁷⁶ Montana State University, Bozeman, MT 59717, USA
- ⁷⁷ Institute for Plasma Research, Bhat, Gandhinagar 382428, India
- ⁷⁸ Nicolaus Copernicus Astronomical Center, Polish Academy of Sciences, 00-716, Warsaw, Poland
- ⁷⁹ Dipartimento di Ingegneria, Università del Sannio, I-82100 Benevento, Italy
- ⁸⁰ OzGrav, University of Adelaide, Adelaide, South Australia 5005, Australia
- ⁸¹ California State University, Los Angeles, 5151 State University Drive, Los Angeles, CA 90032, USA
- ⁸² INFN, Sezione di Genova, I-16146 Genova, Italy
- ⁸³ OzGrav, University of Western Australia, Crawley, Western Australia 6009, Australia
- ⁸⁴ RRCAT, Indore, Madhya Pradesh 452013, India
- ⁸⁵ GRAPPA, Anton Pannekoek Institute for Astronomy and Institute for High-Energy Physics, University of Amsterdam, Science Park 904, 1098 XH Amsterdam, The Netherlands
- ⁸⁶ Missouri University of Science and Technology, Rolla, MO 65409, USA
- ⁸⁷ Faculty of Physics, Lomonosov Moscow State University, Moscow 119991, Russia
- ⁸⁸ Università di Trento, Dipartimento di Fisica, I-38123 Povo, Trento, Italy

- ⁸⁹ INFN, Trento Institute for Fundamental Physics and Applications, I-38123 Povo, Trento, Italy
- ⁹⁰ SUPA, University of the West of Scotland, Paisley PA1 2BE, UK
- ⁹¹ Bar-Ilan University, Ramat Gan, 5290002, Israel
- ⁹² Artemis, Université Côte d'Azur, Observatoire de la Côte d'Azur, CNRS, F-06304 Nice, France
- ⁹³ Dipartimento di Fisica "E.R. Caianiello," Università di Salerno, I-84084 Fisciano, Salerno, Italy
- ⁹⁴ INFN, Sezione di Napoli, Gruppo Collegato di Salerno, Complesso Universitario di Monte S. Angelo, I-80126 Napoli, Italy
- ⁹⁵ Università di Roma "La Sapienza," I-00185 Roma, Italy
- ⁹⁶ Univ Rennes, CNRS, Institut FOTON—UMR6082, F-3500 Rennes, France
- ⁹⁷ Indian Institute of Technology Bombay, Powai, Mumbai 400 076, India
- ⁹⁸ INFN, Laboratori Nazionali del Gran Sasso, I-67100 Assergi, Italy
- ⁹⁹ Laboratoire Kastler Brossel, Sorbonne Université, CNRS, ENS-Université PSL, Collège de France, F-75005 Paris, France
- ¹⁰⁰ Astronomical Observatory Warsaw University, 00-478 Warsaw, Poland
- ¹⁰¹ University of Maryland, College Park, MD 20742, USA
- ¹⁰² Max Planck Institute for Gravitational Physics (Albert Einstein Institute), D-14476 Potsdam, Germany
- ¹⁰³ L2IT, Laboratoire des 2 Infinis—Toulouse, Université de Toulouse, CNRS/IN2P3, UPS, F-31062 Toulouse Cedex 9, France
- ¹⁰⁴ School of Physics, Georgia Institute of Technology, Atlanta, GA 30332, USA
- ¹⁰⁵ IGFAE, Campus Sur, Universidad de Santiago de Compostela, E-15782, Spain
- ¹⁰⁶ The Chinese University of Hong Kong, Shatin, NT, Hong Kong
- ¹⁰⁷ Stony Brook University, Stony Brook, NY 11794, USA
- ¹⁰⁸ Center for Computational Astrophysics, Flatiron Institute, New York, NY 10010, USA
- ¹⁰⁹ NASA Goddard Space Flight Center, Greenbelt, MD 20771, USA
- ¹¹⁰ Dipartimento di Fisica, Università degli Studi di Genova, I-16146 Genova, Italy
- ¹¹¹ Institute for Gravitational and Subatomic Physics (GRASP), Utrecht University, Princetonplein 1, 3584 CC Utrecht, The Netherlands
- ¹¹² Department of Astronomy, Beijing Normal University, Beijing 100875, People's Republic of China
- ¹¹³ OzGrav, University of Melbourne, Parkville, Victoria 3010, Australia
- ¹¹⁴ Università degli Studi di Sassari, I-07100 Sassari, Italy
- ¹¹⁵ INFN, Laboratori Nazionali del Sud, I-95125 Catania, Italy
- ¹¹⁶ Università di Roma Tor Vergata, I-00133 Roma, Italy
- ¹¹⁷ INFN, Sezione di Roma Tor Vergata, I-00133 Roma, Italy
- ¹¹⁸ University of Sannio at Benevento, I-82100 Benevento, Italy and INFN, Sezione di Napoli, I-80100 Napoli, Italy
- ¹¹⁹ Villanova University, 800 Lancaster Avenue, Villanova, PA 19085, USA
- ¹²⁰ Departamento de Astronomía y Astrofísica, Universitat de València, E-46100 Burjassot, València, Spain
- ¹²¹ Universität Hamburg, D-22761 Hamburg, Germany
- ¹²² Rochester Institute of Technology, Rochester, NY 14623, USA
- ¹²³ National Tsing Hua University, Hsinchu City, 30013 Taiwan, People's Republic Of China
- ¹²⁴ Department of Applied Physics, Fukuoka University, Jonan, Fukuoka City, Fukuoka 814-0180, Japan
- ¹²⁵ OzGrav, Charles Sturt University, Wagga Wagga, New South Wales 2678, Australia
- ¹²⁶ Department of Physics, Tamkang University, Danshui Dist., New Taipei City 25137, Taiwan
- ¹²⁷ Department of Physics and Institute of Astronomy, National Tsing Hua University, Hsinchu 30013, Taiwan
- ¹²⁸ Department of Physics, Center for High Energy and High Field Physics, National Central University, Zhongli District, Taoyuan City 32001, Taiwan
- ¹²⁹ CaRT, California Institute of Technology, Pasadena, CA 91125, USA
- ¹³⁰ Department of Physics, National Tsing Hua University, Hsinchu 30013, Taiwan
- ¹³¹ Dipartimento di Ingegneria Industriale (DIIN), Università di Salerno, I-84084 Fisciano, Salerno, Italy
- ¹³² Institute of Physics, Academia Sinica, Nankang, Taipei 11529, Taiwan
- ¹³³ Université Lyon, Université Claude Bernard Lyon 1, CNRS, IP2I Lyon/IN2P3, UMR 5822, F-69622 Villeurbanne, France
- ¹³⁴ Seoul National University, Seoul 08826, Republic of Korea
- ¹³⁵ Pusan National University, Busan 46241, Republic of Korea
- ¹³⁶ INAF, Osservatorio Astronomico di Padova, I-35122 Padova, Italy
- ¹³⁷ University of Arizona, Tucson, AZ 85721, USA
- ¹³⁸ Rutherford Appleton Laboratory, Didcot OX11 0DE, UK
- ¹³⁹ OzGrav, Swinburne University of Technology, Hawthorn VIC 3122, Australia
- ¹⁴⁰ Université Libre de Bruxelles, Avenue Franklin Roosevelt 50, B-1050 Bruxelles, Belgium
- ¹⁴¹ Universitat de les Illes Balears, IAC3—IEEC, E-07122 Palma de Mallorca, Spain
- ¹⁴² Université Libre de Bruxelles, Brussels B-1050, Belgium
- ¹⁴³ Departamento de Matemáticas, Universitat de València, E-46100 Burjassot, València, Spain
- ¹⁴⁴ Texas Tech University, Lubbock, TX 79409, USA
- ¹⁴⁵ The Pennsylvania State University, University Park, PA 16802, USA
- ¹⁴⁶ University of Rhode Island, Kingston, RI 02881, USA
- ¹⁴⁷ The University of Texas Rio Grande Valley, Brownsville, TX 78520, USA
- ¹⁴⁸ Bellevue College, Bellevue, WA 98007, USA
- ¹⁴⁹ Scuola Normale Superiore, Piazza dei Cavalieri, 7, I-56126 Pisa, Italy
- ¹⁵⁰ MTA-ELTE Astrophysics Research Group, Institute of Physics, Eötvös University, Budapest 1117, Hungary
- ¹⁵¹ Maastricht University, P.O. Box 616, 6200 MD Maastricht, The Netherlands
- ¹⁵² University of Portsmouth, Portsmouth, PO1 3FX, UK
- ¹⁵³ The University of Sheffield, Sheffield S10 2TN, UK
- ¹⁵⁴ Université Lyon, Université Claude Bernard Lyon 1, CNRS, Laboratoire des Matériaux Avancés (LMA), IP2I Lyon/IN2P3, UMR 5822, F-69622 Villeurbanne, France
- ¹⁵⁵ Dipartimento di Scienze Matematiche, Fisiche e Informatiche, Università di Parma, I-43124 Parma, Italy
- ¹⁵⁶ INFN, Sezione di Milano Bicocca, Gruppo Collegato di Parma, I-43124 Parma, Italy
- ¹⁵⁷ Physik-Institut, University of Zurich, Winterthurerstrasse 190, 8057 Zurich, Switzerland
- ¹⁵⁸ University of Chicago, Chicago, IL 60637, USA
- ¹⁵⁹ Université de Strasbourg, CNRS, IPHC UMR 7178, F-67000 Strasbourg, France
- ¹⁶⁰ West Virginia University, Morgantown, WV 26506, USA
- ¹⁶¹ Montclair State University, Montclair, NJ 07043, USA
- ¹⁶² Colorado State University, Fort Collins, CO 80523, USA

- ¹⁶³ Institute for Nuclear Research, Hungarian Academy of Sciences, Bem tér 18/c, H-4026 Debrecen, Hungary
- ¹⁶⁴ Department of Physics, University of Texas, Austin, TX 78712, USA
- ¹⁶⁵ CNR-SPIN, c/o Università di Salerno, I-84084 Fisciano, Salerno, Italy
- ¹⁶⁶ Scuola di Ingegneria, Università della Basilicata, I-85100 Potenza, Italy
- ¹⁶⁷ Observatori Astronòmic, Universitat de València, E-46980 Paterna, València, Spain
- ¹⁶⁸ The University of Utah, Salt Lake City, UT 84112, USA
- ¹⁶⁹ Kenyon College, Gambier, OH 43022, USA
- ¹⁷⁰ Vrije Universiteit Amsterdam, 1081 HV, Amsterdam, The Netherlands
- ¹⁷¹ Department of Astronomy, The University of Tokyo, Mitaka City, Tokyo 181-8588, Japan
- ¹⁷² Faculty of Engineering, Niigata University, Nishi-ku, Niigata City, Niigata 950-2181, Japan
- ¹⁷³ State Key Laboratory of Magnetic Resonance and Atomic and Molecular Physics, Innovation Academy for Precision Measurement Science and Technology (APM), Chinese Academy of Sciences, Xiao Hong Shan, Wuhan 430071, People's Republic of China
- ¹⁷⁴ University of Szeged, Dóm tér 9, Szeged 6720, Hungary
- ¹⁷⁵ Universiteit Gent, B-9000 Gent, Belgium
- ¹⁷⁶ Cornell University, Ithaca, NY 14850, USA
- ¹⁷⁷ University of British Columbia, Vancouver, BC V6T 1Z4, Canada
- ¹⁷⁸ Tata Institute of Fundamental Research, Mumbai 400005, India
- ¹⁷⁹ INAF, Osservatorio Astronomico di Capodimonte, I-80131 Napoli, Italy
- ¹⁸⁰ The University of Mississippi, University, MS 38677, USA
- ¹⁸¹ University of Michigan, Ann Arbor, MI 48109, USA
- ¹⁸² Texas A&M University, College Station, TX 77843, USA
- ¹⁸³ Department of Physics, Ulsan National Institute of Science and Technology (UNIST), Ulju-gun, Ulsan 44919, Republic of Korea
- ¹⁸⁴ Applied Research Laboratory, High Energy Accelerator Research Organization (KEK), Tsukuba City, Ibaraki 305-0801, Japan
- ¹⁸⁵ Dipartimento di Fisica, Università di Trieste, I-34127 Trieste, Italy
- ¹⁸⁶ Shanghai Astronomical Observatory, Chinese Academy of Sciences, Shanghai 200030, People's Republic of China
- ¹⁸⁷ American University, Washington, DC 20016, USA
- ¹⁸⁸ Faculty of Science, University of Toyama, Toyama City, Toyama 930-8555, Japan
- ¹⁸⁹ Institute for Cosmic Ray Research (ICRR), KAGRA Observatory, The University of Tokyo, Kamioka-cho, Hida City, Gifu 506-1205, Japan
- ¹⁹⁰ Carleton College, Northfield, MN 55057, USA
- ¹⁹¹ University of California, Berkeley, CA 94720, USA
- ¹⁹² Maastricht University, 6200 MD, Maastricht, The Netherlands
- ¹⁹³ College of Industrial Technology, Nihon University, Narashino City, Chiba 275-8575, Japan
- ¹⁹⁴ Graduate School of Science and Technology, Niigata University, Nishi-ku, Niigata City, Niigata 950-2181, Japan
- ¹⁹⁵ Department of Physics, National Taiwan Normal University, sec. 4, Taipei 116, Taiwan
- ¹⁹⁶ Astronomy & Space Science, Chungnam National University, Yuseong-gu, Daejeon 34134, Republic of Korea
- ¹⁹⁷ Department of Physics and Mathematics, Aoyama Gakuin University, Sagamihara City, Kanagawa 252-5258, Japan
- ¹⁹⁸ Kavli Institute for Astronomy and Astrophysics, Peking University, Haidian District, Beijing 100871, People's Republic of China
- ¹⁹⁹ Yukawa Institute for Theoretical Physics (YITP), Kyoto University, Sakyou-ku, Kyoto City, Kyoto 606-8502, Japan
- ²⁰⁰ Graduate School of Science and Engineering, University of Toyama, Toyama City, Toyama 930-8555, Japan
- ²⁰¹ Department of Physics, Graduate School of Science, Osaka City University, Sumiyoshi-ku, Osaka City, Osaka 558-8585, Japan
- ²⁰² Nambu Yoichiro Institute of Theoretical and Experimental Physics (NITEP), Osaka City University, Sumiyoshi-ku, Osaka City, Osaka 558-8585, Japan
- ²⁰³ Institute of Space and Astronautical Science (JAXA), Chuo-ku, Sagamihara City, Kanagawa 252-0222, Japan
- ²⁰⁴ Directorate of Construction, Services & Estate Management, Mumbai 400094, India
- ²⁰⁵ Vanderbilt University, Nashville, TN 37235, USA
- ²⁰⁶ Universiteit Antwerpen, Prinsstraat 13, B-2000 Antwerpen, Belgium
- ²⁰⁷ University of Białystok, 15-424 Białystok, Poland
- ²⁰⁸ Department of Physics, Ewha Womans University, Seodaemun-gu, Seoul 03760, Republic of Korea
- ²⁰⁹ National Astronomical Observatories, Chinese Academic of Sciences, Chaoyang District, Beijing, People's Republic of China
- ²¹⁰ School of Astronomy and Space Science, University of Chinese Academy of Sciences, Chaoyang District, Beijing, People's Republic of China
- ²¹¹ University of Southampton, Southampton SO17 1BJ, UK
- ²¹² Institute for Cosmic Ray Research (ICRR), The University of Tokyo, Kashiwa City, Chiba 277-8582, Japan
- ²¹³ Chung-Ang University, Seoul 06974, Republic of Korea
- ²¹⁴ Institut de Física d'Altes Energies (IFAE), Barcelona Institute of Science and Technology, and ICREA, E-08193 Barcelona, Spain
- ²¹⁵ Graduate School of Science, Tokyo Institute of Technology, Meguro-ku, Tokyo 152-8551, Japan
- ²¹⁶ University of Washington Bothell, Bothell, WA 98011, USA
- ²¹⁷ Institute of Applied Physics, Nizhny Novgorod, 603950, Russia
- ²¹⁸ Ewha Womans University, Seoul 03760, Republic of Korea
- ²¹⁹ Inje University Gimhae, South Gyeongsang 50834, Republic of Korea
- ²²⁰ Department of Physics, Myongji University, Yongin 17058, Republic of Korea
- ²²¹ Korea Astronomy and Space Science Institute, Daejeon 34055, Republic of Korea
- ²²² National Institute for Mathematical Sciences, Daejeon 34047, Republic of Korea
- ²²³ Ulsan National Institute of Science and Technology, Ulsan 44919, Republic of Korea
- ²²⁴ Department of Physical Science, Hiroshima University, Higashihiroshima City, Hiroshima 903-0213, Japan
- ²²⁵ School of Physics and Astronomy, Cardiff University, Cardiff, CF24 3AA, UK
- ²²⁶ Institute of Astronomy, National Tsing Hua University, Hsinchu 30013, Taiwan
- ²²⁷ Bard College, 30 Campus Road, Annandale-On-Hudson, NY 12504, USA
- ²²⁸ Institute of Mathematics, Polish Academy of Sciences, 00656 Warsaw, Poland
- ²²⁹ National Center for Nuclear Research, 05-400 Świerk-Otwock, Poland
- ²³⁰ Instituto de Física Teórica, E-28049 Madrid, Spain
- ²³¹ Department of Physics, Nagoya University, Chikusa-ku, Nagoya, Aichi 464-8602, Japan
- ²³² Université de Montréal/Polytechnique, Montreal, Quebec H3T 1J4, Canada
- ²³³ Laboratoire Lagrange, Université Côte d'Azur, Observatoire Côte d'Azur, CNRS, F-06304 Nice, France
- ²³⁴ Department of Physics, Hanyang University, Seoul 04763, Republic of Korea
- ²³⁵ Sungkyunkwan University, Seoul 03063, Republic of Korea
- ²³⁶ NAVIER, École des Ponts, Université Gustave Eiffel, CNRS, Marne-la-Vallée, France
- ²³⁷ Department of Physics, National Cheng Kung University, Tainan City 701, Taiwan

- ²³⁸ National Center for High-performance computing, National Applied Research Laboratories, Hsinchu Science Park, Hsinchu City 30076, Taiwan
- ²³⁹ Institute for High-Energy Physics, University of Amsterdam, Science Park 904, 1098 XH Amsterdam, The Netherlands
- ²⁴⁰ NASA Marshall Space Flight Center, Huntsville, AL 35811, USA
- ²⁴¹ University of Washington, Seattle, WA 98195, USA
- ²⁴² Dipartimento di Matematica e Fisica, Università degli Studi Roma Tre, I-00146 Roma, Italy
- ²⁴³ INFN, Sezione di Roma Tre, I-00146 Roma, Italy
- ²⁴⁴ ESPCI, CNRS, F-75005 Paris, France
- ²⁴⁵ Concordia University Wisconsin, Mequon, WI 53097, USA
- ²⁴⁶ Università di Camerino, Dipartimento di Fisica, I-62032 Camerino, Italy
- ²⁴⁷ School of Physics Science and Engineering, Tongji University, Shanghai 200092, People's Republic of China
- ²⁴⁸ Southern University and A&M College, Baton Rouge, LA 70813, USA
- ²⁴⁹ Centre Scientifique de Monaco, 8 quai Antoine 1er, MC-98000, Monaco
- ²⁵⁰ Institute for Photon Science and Technology, The University of Tokyo, Bunkyo-ku, Tokyo 113-8656, Japan
- ²⁵¹ Indian Institute of Technology Madras, Chennai 600036, India
- ²⁵² Saha Institute of Nuclear Physics, Bidhannagar, West Bengal 700064, India
- ²⁵³ The Applied Electromagnetic Research Institute, National Institute of Information and Communications Technology (NICT), Koganei City, Tokyo 184-8795, Japan
- ²⁵⁴ Institut des Hautes Etudes Scientifiques, F-91440 Bures-sur-Yvette, France
- ²⁵⁵ Faculty of Law, Ryukoku University, Fushimi-ku, Kyoto City, Kyoto 612-8577, Japan
- ²⁵⁶ Indian Institute of Science Education and Research, Kolkata, Mohanpur, West Bengal 741252, India
- ²⁵⁷ Department of Astrophysics/IMAPP, Radboud University Nijmegen, P.O. Box 9010, 6500 GL Nijmegen, The Netherlands
- ²⁵⁸ Department of Physics, University of Notre Dame, Notre Dame, IN 46556, USA
- ²⁵⁹ Consiglio Nazionale delle Ricerche—Istituto dei Sistemi Complessi, Piazzale Aldo Moro 5, I-00185 Roma, Italy
- ²⁶⁰ Korea Astronomy and Space Science Institute (KASI), Yuseong-gu, Daejeon 34055, Republic of Korea
- ²⁶¹ Hobart and William Smith Colleges, Geneva, NY 14456, USA
- ²⁶² International Institute of Physics, Universidade Federal do Rio Grande do Norte, Natal RN 59078-970, Brazil
- ²⁶³ Museo Storico della Fisica e Centro Studi e Ricerche “Enrico Fermi,” I-00184 Roma, Italy
- ²⁶⁴ Lancaster University, Lancaster LA1 4YW, UK
- ²⁶⁵ Università di Trento, Dipartimento di Matematica, I-38123 Povo, Trento, Italy
- ²⁶⁶ Indian Institute of Science Education and Research, Pune, Maharashtra 411008, India
- ²⁶⁷ Dipartimento di Fisica, Università degli Studi di Torino, I-10125 Torino, Italy
- ²⁶⁸ Indian Institute of Technology, Palaj, Gandhinagar, Gujarat 382355, India
- ²⁶⁹ Department of Physics, Kyoto University, Sakyou-ku, Kyoto City, Kyoto 606-8502, Japan
- ²⁷⁰ Department of Electronic Control Engineering, National Institute of Technology, Nagaoka College, Nagaoka City, Niigata 940-8532, Japan
- ²⁷¹ Departamento de Matemática da Universidade de Aveiro and Centre for Research and Development in Mathematics and Applications, Campus de Santiago, 3810-183 Aveiro, Portugal
- ²⁷² Marquette University, 11420 W. Clybourn Street, Milwaukee, WI 53233, USA
- ²⁷³ Graduate School of Science and Engineering, Hosei University, Koganei City, Tokyo 184-8584, Japan
- ²⁷⁴ Faculty of Science, Toho University, Funabashi City, Chiba 274-8510, Japan
- ²⁷⁵ Faculty of Information Science and Technology, Osaka Institute of Technology, Hirakata City, Osaka 573-0196, Japan
- ²⁷⁶ Università di Firenze, Sesto Fiorentino I-50019, Italy
- ²⁷⁷ INAF, Osservatorio Astrofisico di Arcetri, Largo E. Fermi 5, I-50125 Firenze, Italy
- ²⁷⁸ Indian Institute of Technology Hyderabad, Sangareddy, Khandi, Telangana 502285, India
- ²⁷⁹ iTHEMS (Interdisciplinary Theoretical and Mathematical Sciences Program), The Institute of Physical and Chemical Research (RIKEN), Wako, Saitama 351-0198, Japan
- ²⁸⁰ INAF, Osservatorio di Astrofisica e Scienza dello Spazio, I-40129 Bologna, Italy
- ²⁸¹ Department of Space and Astronautical Science, The Graduate University for Advanced Studies (SOKENDAI), Sagami-hara City, Kanagawa 252-5210, Japan
- ²⁸² Andrews University, Berrien Springs, MI 49104, USA
- ²⁸³ Research Center for Space Science, Advanced Research Laboratories, Tokyo City University, Setagaya, Tokyo 158-0082, Japan
- ²⁸⁴ Institute for Cosmic Ray Research (ICRR), Research Center for Cosmic Neutrinos (RCCN), The University of Tokyo, Kashiwa City, Chiba 277-8582, Japan
- ²⁸⁵ National Metrology Institute of Japan, National Institute of Advanced Industrial Science and Technology, Tsukuba City, Ibaraki 305-8568, Japan
- ²⁸⁶ Dipartimento di Scienze Aziendali—Management and Innovation Systems (DISA-MIS), Università di Salerno, I-84084 Fisciano, Salerno, Italy
- ²⁸⁷ Van Swinderen Institute for Particle Physics and Gravity, University of Groningen, Nijenborgh 4, 9747 AG Groningen, The Netherlands
- ²⁸⁸ Faculty of Science, Department of Physics, The Chinese University of Hong Kong, Shatin, N.T., Hong Kong
- ²⁸⁹ Vrije Universiteit Brussel, Boulevard de la Plaine 2, B-1050 Ixelles, Belgium
- ²⁹⁰ Department of Communications Engineering, National Defense Academy of Japan, Yokosuka City, Kanagawa 239-8686, Japan
- ²⁹¹ Department of Physics, University of Florida, Gainesville, FL 32611, USA
- ²⁹² Department of Information and Management Systems Engineering, Nagaoka University of Technology, Nagaoka City, Niigata 940-2188, Japan
- ²⁹³ Vrije Universiteit Amsterdam, 1081 HV Amsterdam, The Netherlands
- ²⁹⁴ Department of Physics and Astronomy, Sejong University, Gwangjin-gu, Seoul 143-747, Republic of Korea
- ²⁹⁵ Department of Electrophysics, National Chiao Tung University, Hsinchu, Taiwan
- ²⁹⁶ Department of Physics, Rikkyo University, Toshima-ku, Tokyo 171-8501, Japan
- ²⁹⁷ Department of Physics, McGill University, 3600 rue University, Montréal, QC H3A 2T8, Canada
- ²⁹⁸ McGill Space Institute, McGill University, 3550 rue University, Montréal, QC H3A 2A7, Canada
- ²⁹⁹ David A. Dunlap Department of Astronomy & Astrophysics, University of Toronto, 50 St. George Street, Toronto, ON M5S 3H4, Canada
- ³⁰⁰ Dunlap Institute for Astronomy & Astrophysics, University of Toronto, 50 St. George Street, Toronto, ON M5S 3H4, Canada
- ³⁰¹ Department of Physics and Astronomy, University of British Columbia, 6224 Agricultural Road, Vancouver, BC V6T 1Z1, Canada
- ³⁰² Department of Physics and Astronomy, West Virginia University, P.O. Box 6315, Morgantown, WV 26506, USA
- ³⁰³ Center for Gravitational Waves and Cosmology, West Virginia University, Chestnut Ridge Research Building, Morgantown, WV 26505, USA
- ³⁰⁴ MIT Kavli Institute for Astrophysics and Space Research, Massachusetts Institute of Technology, 77 Massachusetts Avenue, Cambridge, MA 02139, USA
- ³⁰⁵ Department of Physics, Massachusetts Institute of Technology, 77 Massachusetts Avenue, Cambridge, MA 02139, USA
- ³⁰⁶ Division of Physics, Mathematics, and Astronomy, California Institute of Technology, Pasadena, CA 91125, USA
- ³⁰⁷ Anton Pannekoek Institute for Astronomy, University of Amsterdam, Science Park 904, 1098 XH Amsterdam, The Netherlands
- ³⁰⁸ Perimeter Institute for Theoretical Physics, 31 Caroline Street N, Waterloo, ON N2S 2YL, Canada
- ³⁰⁹ Department of Physics and Astronomy, University of Waterloo, Waterloo, ON N2L 3G1, Canada
- ³¹⁰ Sidrat Research, P.O. Box 73527 RPO Wychwood, Toronto, ON M6C 4A7, Canada

³¹¹ National Radio Astronomy Observatory, 520 Edgemont Road, Charlottesville, VA 22903, USA³¹² Department of Astronomy and Astrophysics, Tata Institute of Fundamental Research, Mumbai, 400005, India³¹³ National Centre for Radio Astrophysics, Post Bag 3, Ganeshkhind, Pune, 411007, India

Received 2022 March 21; revised 2023 May 9; accepted 2023 May 18; published 2023 September 28

Abstract

We search for gravitational-wave (GW) transients associated with fast radio bursts (FRBs) detected by the Canadian Hydrogen Intensity Mapping Experiment Fast Radio Burst Project, during the first part of the third observing run of Advanced LIGO and Advanced Virgo (2019 April 1 15:00 UTC–2019 October 1 15:00 UTC). Triggers from 22 FRBs were analyzed with a search that targets both binary neutron star (BNS) and neutron star–black hole (NSBH) mergers. A targeted search for generic GW transients was conducted on 40 FRBs. We find no significant evidence for a GW association in either search. Given the large uncertainties in the distances of our FRB sample, we are unable to exclude the possibility of a GW association. Assessing the volumetric event rates of both FRB and binary mergers, an association is limited to 15% of the FRB population for BNS mergers or 1% for NSBH mergers. We report 90% confidence lower bounds on the distance to each FRB for a range of GW progenitor models and set upper limits on the energy emitted through GWs for a range of emission scenarios. We find values of order 10^{51} – 10^{57} erg for models with central GW frequencies in the range 70–3560 Hz. At the sensitivity of this search, we find these limits to be above the predicted GW emissions for the models considered. We also find no significant coincident detection of GWs with the repeater, FRB 20200120E, which is the closest known extragalactic FRB.

Key words: Gravitational wave astronomy – Radio transient sources

1. Introduction

Fast radio bursts (FRBs) are millisecond duration radio pulses that have been observed out to cosmological distances, several with inferred redshifts greater than unity (Lorimer et al. 2007; Cordes & Chatterjee 2019; Petroff et al. 2019). Although intensely studied for more than a decade, the emission mechanisms and progenitor populations of FRBs are still one of the outstanding questions in astronomy.

Some FRBs have been shown to repeat (Amiri et al. 2019a; CHIME/FRB Collaboration et al. 2019; Kumar et al. 2019), and the recent association of an FRB with the Galactic magnetar SGR 1935+2154 proves that magnetars can produce FRBs (Bochenek et al. 2020; CHIME/FRB Collaboration et al. 2020). Alternative progenitors and mechanisms to produce nonrepeating FRBs are still credible and have so far not been ruled out (Zhang 2020a). Data currently suggest that both repeating and nonrepeating classes of FRBs have dispersion measures (DMs), a quantity equal to the integral of the free electron density along the line of sight, and sky locations consistent with being drawn from the same population. However, the two classes have been shown to differ in their intrinsic temporal widths and spectral bandwidths (CHIME/FRB Collaboration et al. 2021). Whether genuine nonrepeating sources have a different origin compared to that of their repeating cousins is an unresolved question.

The first discovery of an FRB was made over a decade ago by Parkes 64 m radio telescope (Lorimer et al. 2007). This burst, FRB 010724 or FRB 20010724A, known as the *Lorimer burst*, first indicated an extragalactic origin for FRBs through its observed DM. This burst had a DM of 375 pc cm^{-3} , far in excess

of the likely Galactic DM contribution along the line of sight (of order 45 pc cm^{-3} for this event), supporting an extragalactic origin. The precise localizations of FRB host galaxies have since unambiguously confirmed an extragalactic hypothesis (Chatterjee et al. 2017; Bannister et al. 2019; Heintz et al. 2020; Li & Zhang 2020), and constraints on the progenitor population are starting to be understood (e.g., Bhandari et al. 2020). The inferred cosmological distances for many FRBs have shown that these transients have extreme luminosities by radio standards, of the order 10^{38} – $10^{46} \text{ erg s}^{-1}$ (Zhang 2018).

Recent studies suggest a volumetric rate of order $3.5_{-2.4}^{+5.7} \times 10^4 \text{ Gpc}^{-3} \text{ yr}^{-1}$ above $10^{42} \text{ erg s}^{-1}$ (Luo et al. 2020). Up to mid-2018, around 70 FRBs had been publicly announced (Petroff et al. 2016). The majority of the detections during this period had been made by Parkes (27 FRBs at $\sim 1.5 \text{ GHz}$; Thornton et al. 2013; Champion et al. 2016) and ASKAP (28 FRBs at central frequencies of $\sim 1.3 \text{ GHz}$; Bannister et al. 2017; Shannon et al. 2018). Other detections were contributed by telescopes including UTMOST (Caleb et al. 2017) and the Green Bank Telescope (Masui et al. 2015), each operating around 800 MHz, and Arecibo (Spitler et al. 2014), operating around $\sim 1.5 \text{ GHz}$.

The FRB detection rate has greatly increased since the Canadian Hydrogen Intensity Mapping Experiment (CHIME) instrument (Bandura et al. 2014; Newburgh et al. 2014; CHIME/FRB Collaboration 2020; see³¹⁷) began its commissioning phase in late 2018, and its first FRB observation run shortly after. The CHIME radio telescope observes in the frequency range 400–800 MHz and consists of four $20 \times 100 \text{ m}$ cylindrical parabolical reflectors. Its large collecting area and wide field of view ($\approx 200 \text{ deg}^2$) make it a valuable survey instrument for radio transients. FRB detection for this instrument has been led by the CHIME/FRB project (CHIME/FRB Collaboration et al. 2018), which published its first sample of 13 FRBs during its early commissioning phase, despite operating at a lower sensitivity and field of view than design specifications (Amiri et al. 2019b).

³¹⁴ Deceased, August 2020.³¹⁵ McGill Space Institute Fellow.³¹⁶ FRQNT Postdoctoral Fellow.

Original content from this work may be used under the terms of the [Creative Commons Attribution 4.0 licence](https://creativecommons.org/licenses/by/4.0/). Any further distribution of this work must maintain attribution to the author(s) and the title of the work, journal citation and DOI.

³¹⁷ <https://chime-experiment.ca/>

The CHIME/FRB project recently published a catalog of 535 FRBs detected during their first year of operation; this includes 62 bursts from 18 previously identified repeating sources (CHIME/FRB Collaboration et al. 2021). This is the first large collection, $\mathcal{O}(100)$ s, of FRBs from a homogeneous survey and represents a significant milestone in this area of study. The CHIME/FRB data is supportive of different propagation or emission mechanisms between repeaters and nonrepeaters; however, it is still not clear whether all FRBs do repeat (Ravi 2019), and significantly, the FRB emission mechanism remains unknown. There presently exist many competing FRB emission theories (Platts et al. 2019), some of which predict the accompaniment of a time-varying mass quadrupole moment, and, thus, the emission of gravitational waves (GWs).

A number of studies have looked at the possibility of GW emission associated with FRBs indirectly, using radio observations to search for coherent FRB-like emissions associated with short, hard gamma-ray bursts (GRBs; Anderson et al. 2018; Rowlinson & Anderson 2019; Bouwhuis et al. 2020; Gourdji et al. 2020; Rowlinson et al. 2021).

The identification of an FRB within the sensitive reach of GW interferometric detectors could provide conclusive proof of an association or constrain the parameters of the emission mechanisms for a given FRB. The increased population of detected FRBs from the CHIME/FRB Project therefore offers a unique chance of achieving this endeavor.

The first search for GW counterparts to transient radio sources was conducted by Abbott et al. (2016). This used a minimally modeled coherent search (X-Pipeline) ± 2 minutes around the detection time of 6 Parkes FRBs using GW data from GEO600 (Grote 2010) and initial Virgo (Accadia et al. 2012). No GW coincidences were found, but this study provided a useful framework for future searches using improved GW sensitivities.

In this paper, we present the second targeted GW follow-up of FRBs using bursts detected by CHIME/FRB during the first part of the third observing run of Advanced LIGO and Advanced Virgo (O3a; Aasi et al. 2015; Acernese et al. 2015), which took place between 2019 April 1 15:00 UTC and 2019 October 1 15:00 UTC. This search uses both a generic GW transient search and a modeled search targeting coalescing binary systems.

The organization of this paper is as follows: in Section 2, we describe the motivation of this study by discussing possible GW counterparts to FRBs. We introduce the CHIME/FRB data sample in Section 3 and in Section 4 discuss the GW search methods employed; this includes an overview of both of the pipelines used in our analysis. Section 5 provides the results of the GW analysis of the FRB sample. In Section 6, we report results of a gravitational-wave analysis of the repeater, FRB 20200120E, which is the closest known extragalactic FRB. Finally, in Section 7, we summarize the astrophysical implications of our results and discuss future GW searches for FRB counterparts at greater GW sensitivities.

2. Proposed Gravitational-wave Counterparts to FRBs

This section will review some of the more popular models of nonrepeating and repeating FRBs that could provide plausible GW counterparts and could therefore be constrained or

confirmed through GW searches. (An online theory catalog tracks new FRB models; see).³¹⁸

As the millisecond durations of FRBs indicate compact emission regions, many models of nonrepeating FRBs have suggested cataclysmic events, including coalescing compact objects. As will be discussed below, the fraction of the energy budget emitted by proposed FRB emission models is comparatively small compared to $\mathcal{O}(10^{52})$ erg emitted in GWs (e.g., Abbott et al. 2017c) but high by radio standards.

A number of studies have investigated the possibility of FRB-like emissions from binary neutron star (BNS) coalescence around the time of merger (see review in Platts et al. 2019). During this phase, the magnetic fields of the neutron stars (NSs) are synchronized to binary rotation, and a coherent radiation could be generated due to magnetic braking. The mechanism requires magnetic fields of the order 10^{12} – 10^{13} Gauss and could lead to energy-loss rates of the order 10^{45} erg s⁻¹. The predicted FRB pulse widths are consistent with the timescale of the orbital period of the BNS just prior to coalescence (Totani 2013).

Wang et al. (2016) considered that an FRB could be produced during the final stages of a BNS inspiral through magnetic reconnection due to the interaction of a toroidal magnetic field, produced as the NS magnetospheres approach each other. The predicted energy-loss rates are order 10^{42} erg s⁻¹ assuming magnetic fields of the order 10^{12} Gauss. One should note, the dynamic ejecta launched shortly after the final merger would produce significant opacity over a large solid angle, thus screening an FRB-type signal via absorption (Yamasaki et al. 2018). Zhang (2020b) has also entertained the idea that similar interactions between the two NS magnetospheres could produce repeating FRB-like coherent radio emissions decades or centuries before the final plunge.

Other mechanisms to produce prompt coherent radio emission on millisecond timescales include excitation of the circumbinary plasma by GWs (Moortgat & Kuijpers 2005), from dynamically generated magnetic fields post-merger (Pshirkov & Postnov 2010), or from the collision of a GRB forward shock with the surrounding medium (Usov & Katz 2000; Sagiv & Waxman 2002).

Mergers of significant fractions of BNSs are likely to give rise to millisecond magnetars (Gao et al. 2016; Margalit et al. 2019), although this is highly dependent on the unknown nuclear equation of state (see Sarin & Lasky 2021, for a review). If the remnant NS mass is greater than the maximum nonrotating mass, it can survive for hundreds to thousands of seconds before collapsing to form a BH (Ravi & Lasky 2014). As the magnetic field lines snap as they cross the black hole (BH) horizon, an outwardly directed magnetic shock would dissipate as a short, intense radio burst (Falcke & Rezzolla 2014; Zhang 2014). The energy in the magnetic shock can be estimated as $\mathcal{O}(10^{47})$ erg, which is more than sufficient to support an FRB emission. This model has been motivated by the observation of relatively long-lived X-ray plateaus following short gamma-ray bursts that exhibit an abrupt decay phase, commonly interpreted as the collapse of the nascent NS to a BH (Troja et al. 2007; Lyons et al. 2010; Rowlinson et al. 2010, 2013). Such collapses are expected to occur $\lesssim 5 \times 10^4$ s after the merger (Ravi & Lasky 2014).

³¹⁸ <https://frbtheorycat.org>

The detection of the intense millisecond duration radio associated with the Galactic magnetar SGR 1935+2154 (CHIME/FRB Collaboration et al. 2020) has provided significant evidence to an FRB–magnetar connection (Popov & Postnov 2013). It is known that the energy stored in rotational kinetic energy and the magnetic field of a millisecond pulsar is ample to power a repeating FRB (Metzger et al. 2017). In terms of the energy, Margalit et al. (2020) used the energy-loss rates of repeater FRB 20121102A to estimate an energy budget for repeaters at least 10^{47} – 10^{49} erg. This lower limit is based on the so-far observed pulses and without consideration of beaming, so could increase with further monitoring of this source (Petroff et al. 2022).

Resonant oscillation modes in the core and crust of magnetars have been suggested to cause quasi-periodic oscillations observed in the X-ray tails of giant flares. If the process by which FRBs are created also excites nonradial modes in the magnetars, then GWs could simultaneously be produced (e.g., Levin & van Hoven 2011; Quitzow-James et al. 2017).

The stellar oscillation mode that couples strongest to GW emission is the fundamental f-mode. The frequency of this mode depends on the equation of state; however, analyses of the tidal deformability of GW170817 are consistent with NS f-mode frequencies typically being around 2 kHz (Abbott et al. 2017b, 2017d, 2018; Wen et al. 2019). This is above the most sensitive frequency of the Advanced LIGO/Virgo observatories.

Early theoretical studies suggested $\sim 10^{48}$ – 10^{49} erg in GW energy emitted at around 1–2 kHz (Ioka 2001; Corsi & Owen 2011); large enough for f-mode oscillations from Galactic magnetar flares to be observable by Advanced LIGO/Virgo. The predictions by Levin & van Hoven (2011), Zink et al. (2012) span a much lower range $\sim 10^{28}$ – 10^{38} erg suggesting lower effective energy conversion to GWs.

Other modes such as gravity g-modes (here the restoring force is buoyancy) and Rossby r-modes (where the restoring force is the Coriolis force) emit at frequencies closer to the most sensitive range for Advanced LIGO/Virgo; however, these modes couple more weakly to gravitational modes, and are therefore not likely to be detectable in association with an FRB.

3. The CHIME/FRB Sample

The CHIME/FRB data sample provided for this analysis consists of 338 bursts observed within O3a out of 806 total bursts. Out of this sample, 168 bursts have been published in the first CHIME/FRB catalog (CHIME/FRB Collaboration et al. 2021). Within the sample of 338 bursts, only events overlapping with up-time of at least one of the three GW observatories were considered for analysis. Within this subsample, the selection of bursts that were analyzed was based on the inferred distance to each burst. This selection will be described at the end of this section, after the calculation of the inferred distance is described.

The data for each FRB include localization information, a topocentric arrival time, and a measure of the total DM. For each burst, a transient name server (TNS; see <https://www.wis-tns.org>) designation was also provided. The TNS naming convention takes the form *FRB YYYYMMDDLLL* with the year (YYYY), month (MM), and day (DD) information in UTC and LLL a unique, sequential letter code starting with A up to Z,

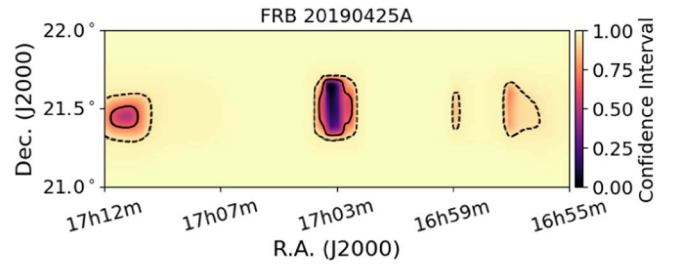


Figure 1. An example of a CHIME localization confidence interval plot for the closest nonrepeating burst in our sample, FRB 190425A. The plot shows 4 localization islands and is centered at the beam with the highest S/N.

then from AA to AZ, up to ZZZ, in order of detection on any given day.

The arrival time at the CHIME instrument’s location (topocentric) at 400 MHz was converted to a dedispersed arrival time using the DM value associated with each event. This time was used as the central event time around which each GW search was conducted.

The localization information of each FRB is in the form of up to 5 disjoint error regions of varied morphology centered around the region with the highest signal-to-noise ratio (S/N); each separate localization *island* has a central value and a 95% confidence uncertainty region. An example is shown in Figure 1.

The localization regions are reported in the sample as a list of 5 R.A. (R.A.) values, 5 95% confidence uncertainty region sizes for the R.A. values, 5 decl. (decl.) values, and 5 95% confidence uncertainty region sizes for the decl. values. The different approaches to these localization data adopted by the generic transient and modeled search pipelines will be described in Section 4.

To determine a measure of the luminosity distance of each FRB, we employ the Macquart relation (Macquart et al. 2020). This relation maps the redshift to the quantity DM_{IGM} , which is the DM contribution from extragalactic gas along the line of sight; this can be obtained after all other contributions are subtracted. Taking into account all contributions to the total DM, the quantity DM_{T} , a measure of redshift can therefore be determined by solving the following:

$$DM_{\text{T}}(z) = DM_{\text{MW}} + DM_{\text{halo}} + DM_{\text{IGM}}(z) + DM_{\text{host}}(z)/(1+z), \quad (1)$$

where DM_{MW} is the Milky Way contribution to the DM along the line of sight, DM_{halo} is the contribution from the Milky Way halo, and DM_{host} is the contribution from the host galaxy, which is corrected by the cosmic expansion factor. The estimates of z are then converted to a luminosity distance assuming a “flat- Λ ” cosmology with the cosmological parameters $\Omega_{\text{m}} = 0.31$, $\Omega_{\Lambda} = 0.69$, and $H_0 = 67.8 \text{ km s}^{-1} \text{ Mpc}^{-1}$ (Planck Collaboration et al. 2016).

To determine redshift values for each FRB, we employ the Bayesian Markov Chain Monte Carlo (MCMC) sampling framework described in Bhardwaj et al. (2021b) with a posterior distribution defined by the following:

$$\mathcal{P}(\hat{\theta} | DM_{\text{T},\text{O}}) = \frac{\mathcal{L}(DM_{\text{T},\text{O}} | \hat{\theta}) \pi(\hat{\theta})}{\mathcal{Z}}, \quad (2)$$

where $\mathcal{L}(DM_{\text{T},\text{O}} | \hat{\theta})$ is the likelihood distribution of the observed quantity $DM_{\text{T},\text{O}}$ given the parameters $\hat{\theta}$, $\pi(\hat{\theta})$ are the

prior distributions on $\hat{\theta}$, and \mathcal{Z} is the Bayesian evidence; this latter factor enters Equation (2) as a normalization factor independent of the model parameters and can be ignored if one is only interested in the posterior distribution rather than model selection. We assume a Gaussian likelihood function provided as the following:

$$\mathcal{L}(\text{DM}_{\text{T},\text{O}} | \hat{\theta}) = \frac{1}{\sqrt{2\pi\sigma^2}} \exp\left[-\frac{(\text{DM}_{\text{T},\text{O}} - \text{DM}_{\text{T}}(\hat{\theta}))^2}{2\sigma^2}\right], \quad (3)$$

with σ the uncertainty on $\text{DM}_{\text{T},\text{O}}$ for each burst and DM_{T} given by Equation (1) (Rafiei-Ravandi et al. 2021).

For the Milky Way contribution DM_{MW} , there is no consensus between the two popular models of Cordes & Lazio (2002), Yao et al. (2017). Therefore, we follow Bhardwaj et al. (2021b) and assume a Gaussian prior based around the minimum of DM_{MW} from these two models along the line of sight; a standard deviation of 20% of this value is also used.

The contribution DM_{halo} has been estimated in a number of studies but is quite uncertain. For example, Yamasaki & Totani (2020) found values of $\text{DM}_{\text{halo}} \sim 30\text{--}245 \text{ pc cm}^{-3}$ using a two component model. Studies by Dolag et al. (2015) found values between $\text{DM}_{\text{halo}} \sim 30\text{--}50 \text{ pc cm}^{-3}$ based on cosmological simulation, and Prochaska & Zheng (2019) estimated values between 30 and 80 pc cm^{-3} . To take account of the large uncertainty in this quantity, we follow Bhardwaj et al. (2021b) and assume a Gaussian prior such that, at 3σ , DM_{halo} has a value 0 or 80 pc cm^{-3} .

The prior on DM_{IGM} assumes the parameterization $\Delta = \text{DM}_{\text{IGM}} / \langle \text{DM}_{\text{IGM}} \rangle$ with the denominator obtained through the Macquart relation. This takes the form provided in Macquart et al. (2020):

$$P(\Delta) = A\Delta^{-\beta} \exp\left[-\frac{(\Delta^{-\alpha} - C^2)}{2\alpha^2\sigma_{\text{DM}}^2}\right], \quad (4)$$

with $\sigma_{\text{DM}} = 0.2z^{-0.5}$, and $[\alpha, \beta] = 3$; the value of C is determined by requiring that $\langle \Delta \rangle = 1$. The form of this model is motivated by the requirement that the DM distribution approaches a Gaussian at small σ_{DM} in accordance with the Gaussianity of large scale structure. It also incorporates a skew at large σ_{DM} to reflect the possibility of overdensities along the line of sight.

Finally, for a prior on DM_{host} , we adopt a lognormal distribution with median $e^{\mu} = 68.2$, and logarithmic width parameter $\sigma_{\text{host}} = 0.88$ as in Macquart et al. (2020).

The quantities outlined above have a large range of uncertainty, and there could be additional contributions, e.g., circumburst material. As a result, redshift values calculated from DMs are generally taken as upper limits. We perform MCMC sampling using the `emcee` package (Foreman-Mackey et al. 2013) based on an affine-invariant sampling algorithm (Goodman & Weare 2010) using 256 walkers of 20,000 samples. The inferred values of z , and thereby luminosity distance, and their 90% credible intervals are thus determined for each FRB, based on the observed values of DM_{T} , R.A. and decl., the estimated DM_{MW} along the line of sight, and the priors on other DM contributions described above.

Given the large uncertainties in the distances of FRBs, we based our analysis and results on the 90% credible intervals inferred for the CHIME/FRB sample of bursts. However, for

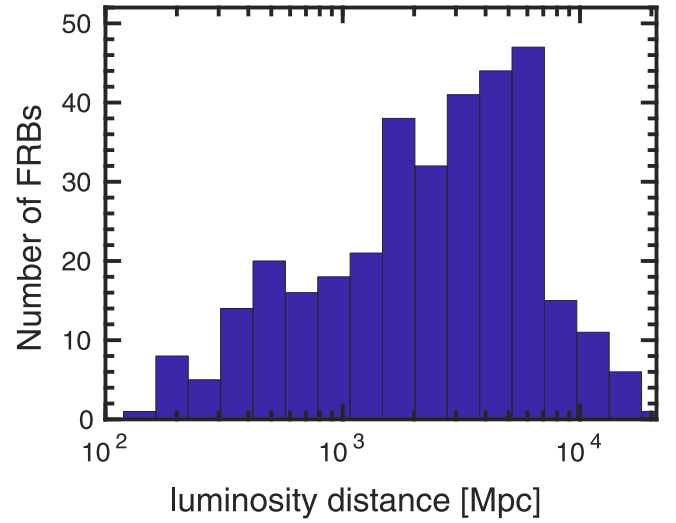


Figure 2. The distribution of inferred median distances for the CHIME/FRB data sample based on the MCMC analysis of Section 3; there is a large uncertainty in these distances; thus, this distribution should be taken as only an approximate representation. The distribution peaks between 1700 Mpc ($z \sim 0.3$) and 6000 Mpc ($z \sim 0.9$). The closest nonrepeating event analyzed in our sample was FRB 20190425A for which we inferred a median distance of 133 Mpc and a range [13–386] Mpc at 90% confidence; the most distant was FRB 20190601C with a median inferred distance of 914 Mpc within a range [199–1737] Mpc.

illustration, we show in Figure 2 the distribution of the median distances of the total sample of 338 FRBs that occurred during O3a. The plot shows that most events seem to occur within 1700 Mpc ($z \sim 0.3$) and 6000 Mpc ($z \sim 0.9$). The closest events in the distribution include a significant number of repeating FRBs. Due to the relatively limited range of the GW detectors, in selecting which bursts to analyze, we first downselected the sample to all bursts from the closest 10% of CHIME/FRB nonrepeating bursts that have GW detector network data available for analysis (if the recent CHIME/FRB catalog of 535 bursts is representative of the FRB population, at least around 11% of FRBs repeat). Within this selection, a coherent analysis using modeled waveforms was then conducted on a smaller subset of the closest 22 nonrepeating events for which data were available from at least one interferometric GW detector, and a generic transient coherent analysis was conducted on a subset of FRBs for which data were available from at least two interferometric GW detectors. The further downselection to the final set of analyses reported was based on two considerations. For some events, the systematic noise in the detector was too significant near the time of the burst for one or both of our two searches, and these events were then excluded. Finally, as each search requires significant person power and computational resources, we performed searches on the remaining subset of events in order of increasing distance, until we reached a point of diminishing returns caused by the reduced overlap between the effective detection range of the GW detection network and the inferred distance to each FRB event. These considerations yielded a sample of 34 nonrepeating FRBs that were analyzed by one or both types of analysis. Using the same considerations for selection, we analyzed a total of 11 repeated bursts from the closest 3 repeating sources: FRB 20180916B (7 repeat events during O3A), FRB 20180814A (2 repeat events), and FRB20190303A (2 events). The lower and upper 90% limits of the credible

intervals on the luminosity distances to each of the nonrepeating FRBs analyzed are included in the tables in Section 5.

4. Search Methods

Here, we will provide a description of the two targeted search methods used in this paper. These are the same methods applied to search for GW events coincident with GRBs that occurred during the first (Abbott et al. 2017a), second (Abbott et al. 2019a), and third (Abbott et al. 2021) Advanced LIGO and Advanced Virgo observing runs. In Section 4.1, we describe the modeled search method that aims to uncover subthreshold GW signals emitted by BNS and neutron star–black hole (NSBH) binaries (PyGRB; Harry & Fairhurst 2011; Williamson et al. 2014), highlighting choices in analysis configuration that are unique to the follow-up of FRB events. In Section 4.2, we discuss the search for generic GW transients (X-Pipeline; Sutton et al. 2010; Was et al. 2012).

4.1. PyGRB—Modeled Search for Binary Mergers

The modeled search for GWs associated with FRB events makes use of the PyGRB data analysis pipeline (Harry & Fairhurst 2011; Williamson et al. 2014), and the search is configured to be similar to the search for GW signals coincident with GRBs in O3a (Abbott et al. 2021). This is a coherent matched-filtering pipeline that compares the GW detector network data with a bank of pregenerated waveforms, including the inspiral of BNS and NSBH binaries. PyGRB uses the PyCBC (Nitz et al. 2020) open-source framework for distribution of the analysis of the GW data across large computing clusters, and also relies on several elements of the LALSuite software library (LIGO Scientific Collaboration 2018).

The PyGRB analysis searches the combined detector data in the range 30–1000 Hz. A set of coherent data streams is formed by combining the data from the detectors, using a sample of sky positions in the region reported for the FRB event that is being studied. These data streams are then compared using matched filtering to the same predefined bank of waveform templates (Owen & Sathyaprakash 1999) used in the search for GWs associated with GRBs events in O3a (Abbott et al. 2021). The bank is created with a hybrid of geometric and stochastic template placement methods across target search space (Harry et al. 2008, 2014; Brown et al. 2012; Capano et al. 2016; Dal Canton & Harry 2017), using a phenomenological inspiral-merger-ringdown waveform model for non-precessing point-particle binaries (IMRPhenomD; Husa et al. 2016; Khan et al. 2016). This bank of templates is designed to cover binary masses in the range $[1.0, 2.8]M_{\odot}$ for NSs, and $[1.0, 25.0]M_{\odot}$ for BHs. The bank also allows for aligned-spin, zero-eccentricity BNS and NSBH, with dimensionless spins in the range $[0, 0.05]$ for NSs and $[0, 0.998]$ for BHs.

Coherent matched filtering can be susceptible to loud transient noise in the detector data and can produce a high S/N (Nitz et al. 2017). To combat this, the analysis performs additional tests on each point of high S/N data, which we also refer to as triggers. These tests can either remove the trigger or reweight the S/N using a χ^2 test. This latter test determines how well the data agrees with the template over the whole template duration. Such cuts and reweighting significantly improve the ability of the search to distinguish a GW from many types of transient noise, thus improving the significance

of real GW triggers. The final reweighted S/N of each candidate event is used as the measure of its relative significance, or ranking statistic, within the search.

The PyGRB analysis searches for GW inspiral events that merge within 12 s of the dedispersed event time of each FRB, with an asymmetric *on-source window* starting 10 s before the FRB event and ending 2 s after the event. The search window is chosen to strike a balance between maximizing the possible progenitor models through a wider window or maximizing the sensitivity of the search by using a narrower window. In this search, we seek a GW signal with a merger time close to the time of the FRB, assuming the FRB results from the interaction of the two binary components.

The sensitivity of the search is governed by the comparison between the most significant event in the on-source window and the most significant event in equivalent trial searches of 12 s windows in the surrounding data, known as the *off-source trials*. These off-source trials form the background data for the search, and if a sufficient number of background trials are conducted, this allows the search to determine the significance of any candidate events in the on-source window to the level needed to make a confident detection statement by computing a false-alarm probability.

If multiple detectors are available, then additional effective background data can be produced by combining the data from the detectors with an intentional misalignment in time of at least the light-travel time across the network to ensure any detected events cannot possibly be true coherent GW candidates (Williamson et al. 2014). This can be repeated for multiple possible time shifts, and in this search, these time shifts are set to match the on-source window length of 12 s. This produces fewer time shifts than a 6 s on-source window, as used in previous searches for GW associated with GRB events such as Abbott et al. (2021). This again impacts the effective significance of any detected events, because the amount of background data used by the search is limited by the amount of coherently analyzable data for all detectors in the network that surrounds the target time. Thus, a search is only conducted if a minimum of 30 minutes of data is available.

In the results section, we report the effective range of each search conducted as a 90% exclusion distance, D_{90} . This is calculated by first creating a set of simulated GW signals to inject into the off-source data, then attempting to find these injected signals with the standard search pipeline. The signals are injected with amplitudes appropriate for a distribution of distances between their simulated origin and the detectors, and the D_{90} distance is defined as the distance within which 90% of the injected simulated signals are recovered with a ranking statistic greater than the loudest on-source event.

Mirroring the approach taken in the O3a search for GW events associated with GRB detections (Abbott et al. 2021), the injected signals include BNS systems with dimensionless spins in the range -0.4 to 0.4 , taken from observed pulsar spins (Hessels et al. 2006), and are distributed uniformly in spin and with random orientations. The injections also include aligned-spin NSBH binaries, and NSBH binaries with generically oriented spins up to 0.98, motivated by X-ray binary observations (e.g., Özel et al. 2010; Kreidberg et al. 2012; Miller & Miller 2014). The simulated signals are intentionally generated using different GW signal models than those used in the matched-filtering template bank, to approximate the target search space difference between the approximate templates

used and the true GW signals. In particular, the injected waveforms are identical to those used in the equivalent O3a GRB event follow-up analysis (Abbott et al. 2021). Precessing BNS signals are simulated using the TaylorT2 time-domain, post-Newtonian inspiral approximant (`SpinTaylorT2`; Sathyaprakash & Dhurandhar 1991; Blanchet et al. 1996; Mikoczi et al. 2005; Arun et al. 2009; Bohé et al. 2013, 2015; Mishra et al. 2016), while NSBH injected waveforms are generated assuming a point-particle effective-one-body model tuned to numerical simulations, which can allow for precession effects from misaligned spins (`SEOBNRv3`; Pan et al. 2014; Taracchini et al. 2014; Babak et al. 2017). Again, identical to the injections used in Abbott et al. (2021), NS masses for the injections are taken between $1 M_{\odot}$ and $3 M_{\odot}$ from a normal distribution centered at $1.4 M_{\odot}$ with a standard deviation of $0.2 M_{\odot}$ (Kiziltan et al. 2013) and $0.4 M_{\odot}$ for BNS and NSBH systems, respectively. BH masses are taken to be between $3 M_{\odot}$ and $25 M_{\odot}$ from a normal distribution centered at $10 M_{\odot}$ with a standard deviation of $6 M_{\odot}$.

Although this `PyGRB` follow-up of FRB events mirrors the search conducted for GWs associated with GRB events in O3a (Abbott et al. 2021) where appropriate, there were several differences in the choices of analysis parameters for the FRB analysis. The first major difference has been noted above, wherein a 12 s on-source window is used, which is double that of the GRB analysis. This does reduce the significance of any detected signals, but has the benefit of allowing for more progenitor models where the EM emission occurs further in time from the peak of the GW emission.

Another significant change was the method of determining the area of sky over which to search for the GW signals. The FRB data sample contains multiple localizations for each event, each with their own R.A. and decl. uncertainties. This effectively creates multiple patches on the sky where the source could potentially reside. The effective GW network localization capability results in 90% credible regions for detections on the order of ≈ 10 – $10,000 \text{ deg}^2$, with an average of order 100 deg^2 . In contrast, the multiple O3a FRB sample localizations spanned only the order 1 deg^2 in total (Abbott et al. 2020a). The sensitivity of the search also did not vary significantly over the sky localizations, and so the final set of sky positions considered by the analysis was one circular patch on the sky with a size large enough to ensure coverage over all possible provided FRB localizations. This circular region is centered on the median of the provided R.A. and decl. values, with a radius scaled to match either the largest position error provided or the largest R.A. or decl. separation between the 5 localization points, using whichever is greater. Within this patch, the sky is sampled by creating a circular grid of sky positions such that the time-delay between grid points is kept below 0.5 s (Williamson et al. 2014). This ensures coverage of the possible sky location of the source. For each sky position, the timestream data from each GW detector are combined with the appropriately different time offsets required to form a coherent stream of data for that point on the grid. These multiple coherent time streams are finally each considered in the search.

4.2. X-Pipeline—Unmodeled Search for Generic Transients

The search for generic transients is performed with the coherent analysis algorithm X-Pipeline (Sutton et al. 2010;

Was et al. 2012). This targeted search uses the sky localization and time window for each CHIME/FRB trigger to identify consistent excess power that is coherent across the network of GW detectors. We use different search parameters in our searches for repeating and nonrepeating FRB sources.

There are a number of differences between our generic transient search on nonrepeated sources and those previously conducted on GRBs (Abbott et al. 2017a, 2019a, 2021). As in GRB searches, the on-source time window is chosen to start 600 s before the trigger, but is extended from 60 s seconds post trigger to 120 s to allow for the possibility of GW emissions delayed relative to the FRB emission. This on-source window is also longer than the $\pm 120 \text{ s}$ window employed in the previous FRB search (Abbott et al. 2016). The extended window allows for a greater number of noncompact binary coalescence (CBC) sources than those considered in GRB searches and possible GW emissions from magnetars, given the recent FRB–magnetar association (CHIME/FRB Collaboration et al. 2020).

The broadband search for FRBs with X-Pipeline covers the range 32 Hz up to 2 kHz, the upper range being higher than the GRB search (20–500 Hz) in order to include GW emissions from oscillation modes of NSs that are likely to occur above 1 kHz, specifically f-modes (Wen et al. 2019; Ho et al. 2020). We note that above 300 Hz a $\propto f^2$ frequency dependence in energy (see later Equation (5)) combined with the $\propto f^1$ of the noise power spectral density of the detector increases the GW energy required to enable a confident detection as $\propto f^3$. Although including high-frequency data increases the computational cost, including this data allows us to set limits on a wider variety of signal models.

X-Pipeline processes the on-source data around each FRB trigger by combining the GW data coherently after the data is whitened by dividing by each detector’s amplitude spectrum (Abbott et al. 2020b). The coherent combination is formed by taking into account the antenna response and noise level of each detector to generate a series of time–frequency maps. The maps show the temporal evolution of the spectral properties of the signal and allow searches for clusters of pixels with excess energy significantly greater than one would expect from background noise. These clusters are referred to as *events*.

Events are given a ranking statistic based on energy and are subjected to coherent consistency tests based on the signal correlations between data in different detectors. This allows X-Pipeline to veto events that have properties similar to the noise background.

The surviving event with the largest ranking statistic is taken to be the best candidate for a GW detection. Its significance is quantified as the probability for the background alone to produce such an event. This is done by comparing the S/N of the trigger within the 720 s on-source to the distribution of the S/Ns of the loudest triggers in the off-source trials. The off-source data are set to consist of at least 1.5 hr of coincident data from at least two detectors around the trigger time. This window is small enough to select data where the detectors should be in a similar state of operation as during the on-source interval, and large enough so that, through artificial time-shifting, probabilities can be estimated at the subpercent level.

We quantify the sensitivity of the generic transient search by injecting simulated signals into off-source data and recovering them. We account for calibration errors by jittering the amplitude and arrival time of the injections according to a

Gaussian distribution representative of the typical calibration uncertainties expected in O3a. We compute the percentage of injections that have a significance higher than the best event candidate and determine the amplitude at which this percentage is above 90%; this value sets the upper limit.

As discussed in Section 3, the localization information for each FRB is in the form of up to 5 noncontiguous or overlapping error regions of varied morphology. Occasionally, these islands can be dominated by the uncertainty of a single island. The sky position errors can span a few degrees or more in R.A. This could result in a temporal shift causing a GW signal to be rejected by a coherent consistency test (Was et al. 2012). For each island, we set up a circular grid around the central location of the island, with overlapping grid points discarded. A coherent data stream is formed from the GW detector data with an appropriate time offset for each point on the grid. These data streams are then analyzed. The grid positions are large enough to cover the error radius and dense enough to ensure that a maximum timing delay error, set as 1.25×10^{-4} s, is within 25% of the signal period at our frequency upper limit of 2000 Hz. This is 4 times finer than GRB searches that typically analyze data up to a frequency cutoff of 500 Hz. Using this grid approach, the antenna responses change only slightly over sky position; of the order of a few percent over a few degrees (Aasi et al. 2014). The responses are known to change rapidly near a null of the response; in such a case, they are already negligible.

A particular difference between this search and other searches focused on GRBs is the increased number of simulated waveform types used in this study. Given the uncertainty in plausible GW emissions, we consider a larger range of generic burst scenarios, using an extended set of those used in both GRB and magnetar searches (Abbott et al. 2019b, 2021). Also, as we have no knowledge on whether or not FRBs are beamed along the rotation axis of the progenitor, all of our signal models correspond to elliptical and random polarization.

The waveforms chosen to cover the search parameter space are from 3 families that have different morphological characteristics: binary signals, generic burst-like signals, and accretion disk instability (ADI) models. X-Pipeline is equally adept at detecting signals whose frequency decreases with time (ADI) and signals whose frequency increases with time (CBC models; Abadie et al. 2012; Abbott et al. 2017a). This paper reports the results for CBCs when obtained using the dedicated modeled search (described in Section 4.1), so we will limit our discussions here to only the latter two waveform families.

The generic burst-type waveforms are described in Table 1, where we list the most important parameters (see also Abbott et al. 2019c). In all cases, to determine exclusion distances for this model family, we assume an optimistic emission of energy in GWs of $E_{\text{GW}} = 10^{-2} M_{\odot} c^2$ (Abbott et al. 2021). The waveforms in this family aim to capture the general characteristics of a burst of GW energy:

Sine-Gaussian. These signals have been used previously to represent the GWs from stellar collapses. The models are defined in Equation (1) of Abbott et al. (2017a) with a Q factor of 9 and varying central frequency as shown in Table 1. They can also model f-modes in the core of a canonical NS. We therefore also include them in the search over repeating sources, and include sine-Gaussian (SG)

Table 1
The Main Parameters of the Waveform Injections Used for the Generic Transient Search

Label	Frequency (Hz)	Duration Parameter (ms)
Sine-Gaussian Chirplets		
SG-A	70	14
SG-B	90	11
SG-C	145	6.9
SG-D	290	3.4
SG-E	650	1.5
SG-F	1100	0.9
SG-G	1600	0.6
SG-H	1995	0.5
SG-I*	2600	0.38
SG-J*	3100	0.32
SG-K*	3560	0.28
SG-L ^{*c}	1600	0.6
SG-M ^{*c}	1995	0.5
Ringdowns		
DS2P-A	1500	100
DS2P-B	1500	200
White Noise Bursts		
WNB-A	150 (100–200)	11
WNB-B	150 (100–200)	100
WNB-C	550 (100–1000)	11
WNB-D	550 (100–1000)	100

Notes. Models and their parameters have been chosen to cover as large a parameter space as possible. For all models, the central frequencies are shown. We note that WNB models are defined by an additional frequency bandwidth; this parameter is shown in parenthesis. For the SG and WNB waveforms, the duration parameter scales the width of the Gaussian envelope; for the DS2P models, this parameter defines the decay time constant. An asterisk (*) denotes waveforms used in the repeaters search only; ^c denotes waveforms with a circular polarization.

waveforms at additional frequencies listed in Table 1. In order to better constrain some models, we also include circularly polarized SG chirplets at the frequencies nearest the f-mode range (1600 and 1995 Hz) in the search over repeated sources.

Ringdowns (DS2P). These signals capture the form of damped sinusoids (DS2P) at a frequency of 1500 Hz and decay constants of 100 and 200 ms.

White noise bursts (WNB). These signals mimic broad bursts of uncorrelated white noise, time-shaped by a Gaussian envelope. We use two models band-limited within frequencies of 100–200 and 100–1000 Hz, and with time constants of 11 and 100 ms.

Following the predictions from oscillation modes for NS starquakes (Li et al. 2019; Wen et al. 2019), the first two waveforms in this family (SG and DS2P) have been used in the search for GWs associated with magnetar bursts (Abbott et al. 2019b, 2022).

We also consider a range of models. These are long-lasting waveforms, which are modeled to represent the GW emissions from instabilities in a magnetically suspended torus around a rapidly spinning BH. The model specifics and parameters used to generate the five types of ADI signals, designated ADI-A to

ADI-E, are the same used in the previous searches (see Table 1 of Abbott et al. 2017a).

The version of X-Pipeline used in this analysis has a new feature named autogating. This feature increases the sensitivity of the longer-duration ($\gtrsim 10$ s) signals, previously limited by loud background noise transients (Abbott et al. 2021). This technique gates the whitened data from a single detector if the average energy over a 1 s window exceeds a user-specified threshold. To minimize the possibility of a loud GW transient being gated, this procedure is canceled if the average energy at the same time in any other detector exceeds the threshold.

4.2.1. X-pipeline Search on Repeating FRBs

A subset of 11 of the FRBs that we analyze has been identified to repeat. Repeating FRBs are possibly caused by a process distinct from those that produce singular FRBs; most notably they are unlikely to be associated with CBC events. We therefore only run the X-Pipeline generic transient search on these events, and we choose the parameters to provide maximal sensitivity to the GW transients that would most probably be produced by flaring magnetars.

This search is similar to that for GW events associated with magnetars during the third observing run of Advanced LIGO and Advanced Virgo (O3; R. Abbott et al. 2023, in preparation). The frequency band of the search ranges from 50 to 4000 Hz, which encapsulates the NS f-mode frequency band, but excludes the lowest frequencies where nonstationary noise could potentially *pollute* the search statistics. The search spans 8 s of time centered within 1 s of the arrival time of the FRB to ensure optimal sensitivity at the event time. Injected waveforms are chosen to reasonably model the f-modes of a canonical NS as described in Kokkotas et al. (2001). This includes a series of SG chirplets with a quality (Q) factor of 9 and varying center frequencies as shown in Table 1. We also neglect to use the autogating algorithm for noise transients as described above, as its tendency is also to gate fast injections such as SG. We also inject WNBs to estimate the sensitivity at broadband frequency ranges.

4.3. RAVEN Coincident Analysis

To perform a wider sweep of the O3a data, we also looked for coincidences between these CHIME/FRB events and existing GW candidates using the tools of the Rapid, on-source VOEvent Coincidence Monitor (RAVEN; Urban 2016; Cho 2019) to query the Gravitational-Wave Candidate Event Database (GraceDB; Pace et al. 2012). This query to GraceDB tests whether any GW candidates were found by any of the modeled or generic transient low-latency GW search pipelines within a time window around the FRB events. The queries used the same on-source search windows as our modeled and generic transient searches, with $[-10, +2$ s] and $[-600, +120$ s] windows around the FRB triggers, respectively. We then computed the joint false-alarm rate of any coincident GW candidate within these windows using the overall rate of FRB events in the CHIME/FRB sample calculated across the full span of the O3a observing run and the false-alarm rate of the GW candidate. The joint false-alarm rates were compared against thresholds of around 6 and 1 yr^{-1} for modeled and generic transient searches respectively. This analysis, although not as sensitive as a targeted search, is a strategy that allows us

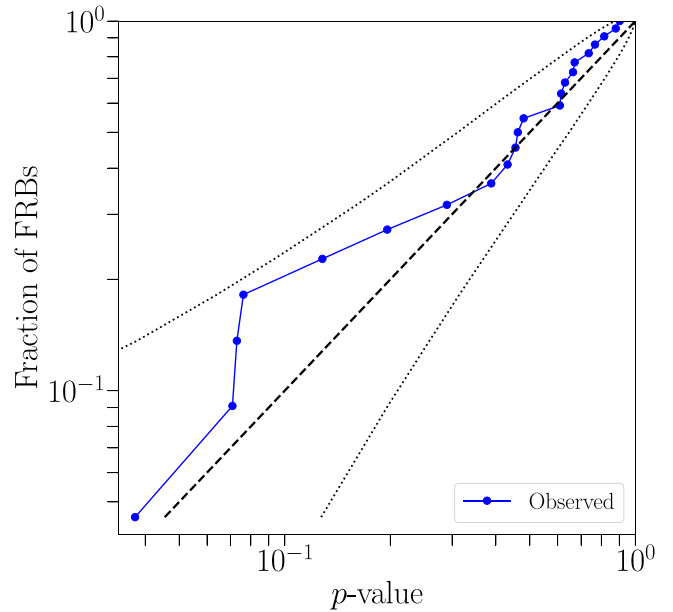


Figure 3. The cumulative distribution of p -values for the loudest on-source events for the modeled search in O3a around CHIME/FRB data. The dashed line indicates an expected uniform distribution of p -values under a no-signal hypothesis, with the corresponding 90% confidence band shown by the dotted lines.

to perform a broad search across O3a data for possible coincidences missed by our analysis.

5. Results of Analysis

5.1. Analysis Subsample

We performed two different searches: for nonrepeating FRBs, a PyGRB modeled search was completed on a total of 22 FRB events; and an X-Pipeline search for generic transient signals was completed on a total of 29 nonrepeaters and 11 repeating FRBs.

5.2. The False-alarm Probability (p -value) Distribution

The searches conducted for GW counterparts returned no likely GW signals in association with any of the analyzed repeating or nonrepeating FRB events.

The most significant events found by the PyGRB search and the X-Pipeline search had p -values of 3.74×10^{-2} and 1.90×10^{-2} , respectively. For the X-Pipeline analysis of the repeating FRBs, the lowest p -value was 1.3×10^{-1} , corresponding to the repeat FRB 20190702B of burst FRB 20190303A, for which we analyzed 2 burst events.

The cumulative p -value distributions from both search methods are shown in Figures 3 and 4. In both figures, the dashed lines indicate the expected background distribution under the no-signal hypothesis, and the dotted lines indicate the 90% confidence band around the no-signal hypothesis.

5.3. Exclusion Distance Results

Figure 5 shows the cumulative 90% exclusion distances for the 22 FRBs followed up with the modeled search. The lowest exclusion distances, of order 40 Mpc, were obtained for FRBs that occurred during times in which only Virgo data were available.

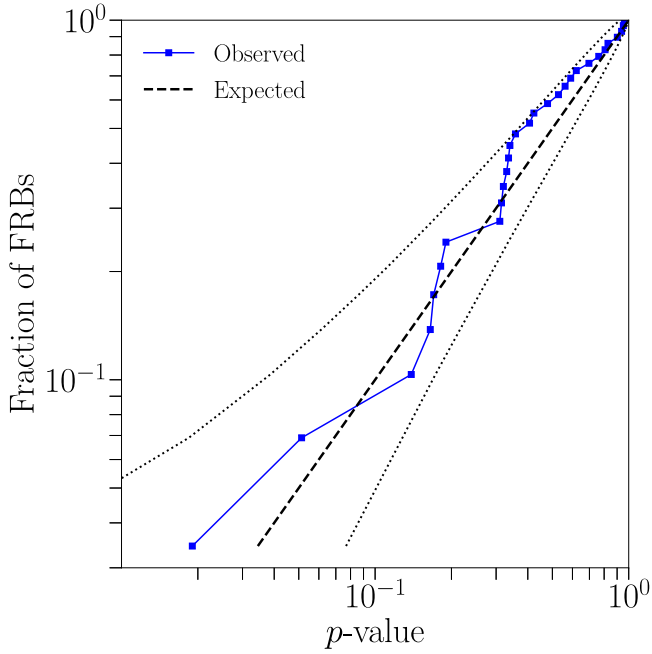


Figure 4. The cumulative distribution of p -values for the loudest events from the generic transient search for transient GWs associated with 29 nonrepeating CHIME/FRB bursts. The dashed line represents the expected distribution under the no-signal hypothesis, with the 90% bands shown as dotted lines.

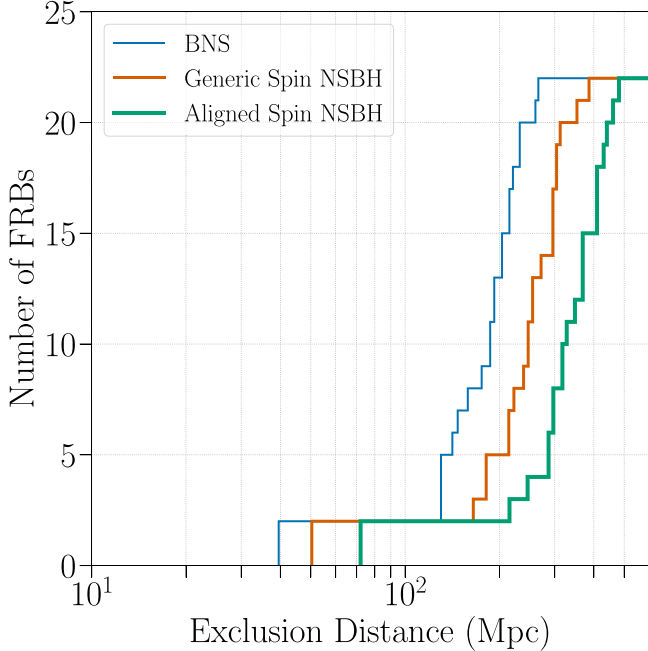


Figure 5. Cumulative histograms of the 90% confidence exclusion distances, D_{90} , for the 22 CHIME/FRB bursts followed up by the modeled search. The blue line shows generically spinning BNS models, the orange line shows generically spinning NSBH models, and the thick green line shows aligned-spin NSBH models. We define D_{90} as the distance within which 90% of the simulated GW signals injected into the off-source data were recovered with a significance greater than the most significant on-source trigger.

For each of the three simulated signal classes considered in the modeled search, we quote the median of the D_{90} results in the top row of Table 2; we see values of the order of 190 Mpc for BNS and around 260 Mpc (350 Mpc) for NSBH with generic (aligned) spins.

Table 2
Median Values for the 90% Confidence Level Exclusion Distances, D_{90}

Modeled Search	NSBH					
	BNS	Generic Spins	Aligned Spins			
D_{90} [Mpc]	191.9	256.6	345.1			
Unmodeled search	SG	SG	SG	SG		
	A	B	C	D		
D_{90} [Mpc]	77.9	63.3	43.7	24.9		
Unmodeled search	SG	SG	SG	SG		
	E	F	G	H		
D_{90} [Mpc]	6.8	2.3	1.2	0.5		
Unmodeled search	DS2P	DS2P	WNB	WNB	WNB	WNB
	A	B	A	B	C	D
D_{90} [Mpc]	0.7	0.7	66.4	71.7	15.2	9.2
Unmodeled search	ADI	ADI	ADI	ADI	ADI	
	A	B	C	D	E	
D_{90} [Mpc]	17.6	64.9	23.1	8.4	25.7	

Note. Modeled search results are shown for three classes of BNS progenitor model, and generic transient search results are shown for models described in Table 1.

Figure 6 provides the cumulative 90% exclusion distances for 29 nonrepeating FRBs considered in the generic transient search. This plot shows three representative burst models: ADI-A, SG-C, and a WNB-C; the latter two have central frequencies of 145 and 550 Hz respectively. Based on a standard $E_{\text{GW}} \sim 10^{-2} M_{\odot} c^2$ of emitted GW energy, there is a noticeable offset between the SG and the other two GW burst models. For the ADI-A waveform model, this is due to the energy of the former being distributed over a longer signal duration, of the order ~ 40 s; for the WNB-C model, this effect is due to a significant portion of its energy content being at higher frequency where detector performance is more comparatively limited.

The lower rows of Table 2 show the median of the D_{90} estimates for all other waveforms considered by the generic transient search. We see that SG models spanning central frequencies 70–2000 Hz have corresponding median values of D_{90} in the range 78–0.5 Mpc; the latter models’ performance diminished at higher frequency through a detector response. This is also clearly evident for the DS2P ringdown models, which are more likely to encounter a transient burst of noise than SG models due to their longer durations. Similarly, the median D_{90} values for the higher-frequency WNB models are lower in comparison with the lower-frequency models (WNB-A and WNB-B). These median D_{90} values of the 150 and 550 Hz models differ by around a factor of at least 4. Overall, the median D_{90} varies within a range approaching 2 orders of magnitude, reflecting the wide range of models used in the analysis.

In comparison with D_{90} values obtained in the O3a GRB paper (Abbott et al. 2021), the values in Table 2 are almost

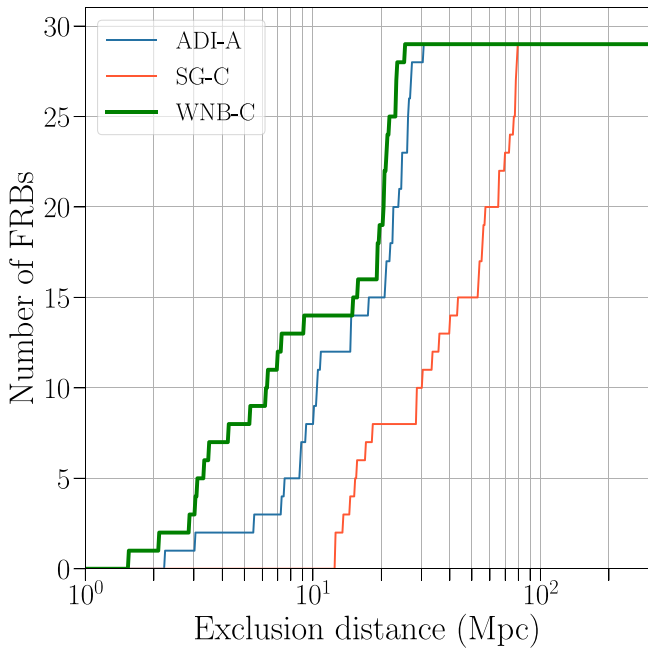


Figure 6. Cumulative histograms of the 90% confidence exclusion distances, D_{90} , for SG model (C) (orange line), accretion disk instability signal model (A) (blue line), and white noise burst model (C) (green, thick line). The quantity has the same definition as described in Figure 5.

systematically a factor of 2 smaller for the SG and ADI models used in that study. We find that this is a result of the sky locations surveyed by CHIME corresponding with a region of weak sensitivity for the Virgo interferometric detector, due to their relative locations on the surface of the Earth. The average antenna responses for the LIGO Hanford (H1) and LIGO Livingston (L1) detectors are of order 0.72 and 0.65 respectively; the same metric for the V1 instrument is 0.28. This has a severe effect when V1 is one of only two detectors in a network, a situation that has occurred 55% of the time for the generic transient analysis of nonrepeating FRBs. Looking ahead, this type of sensitivity bias will be a feature of future searches for CHIME/FRB triggers, as well as surveys by other facilities, depending on their location on the Earth.

In Table 3, we present the exclusion distances achieved for each of the FRBs analyzed in our joint analysis. For the modeled search, we quote values from each of the 3 classes of compact binary progenitor models considered. For the generic transient search, we present values of D_{90} for a representative sample of SG, ADI, DS2P, and WNB models. We also provide information relating to the times and positions of these events as well as values of the DM, and the inferred 90% credible intervals on the luminosity distance. Table 3 allows comparison of the inferred luminosity distances of each FRB with the D_{90} value for different searches.

Figure 7 compares the D_{90} values for the BNS and NSBH (with generic spin) emission models with the 90% credible intervals on D_L inferred by the MCMC analysis. The plot shows the FRB sample in order of increasing distance. No event can be fully excluded from any of the models we have considered for this search, because there is still a sufficient region of space from which the FRB events could have originated that is outside the detection range of the searches performed.

5.4. RAVEN Analysis Results

As described in Section 4.3, two RAVEN coincidence searches were completed with differing time windows, $[-600\text{ s}, +120\text{ s}]$ for the generic transient search and $[-10\text{ s}, +2\text{ s}]$ for the modeled search. The generic transient search found 8 coincidences, and the modeled search found 1 coincidence. However, none of these were of sufficient significance, as determined by the computed joint false-alarm rate from the two samples, to be distinguished from random coincidences. All of the FRBs in these coincidences had distances that were well beyond the values of D_{90} obtained, with the exception being FRB 20190518E, a repeat of burst FRB 20190518A, with 9 episodes occurring during O3a. Of these 9 repeating episodes, 7 were also analyzed using our generic transient search method, as described earlier. Again, none of the repeating episodes returned a significant false-alarm probability, with the minimum p -value across the search of repeating FRB events equal to 1.3×10^{-1} .

5.5. Upper Limits on GW Energy

A measure of the inferred distance to an FRB source also allows one to place constraints on the energy carried in a burst of GWs. The GW energy, E_{GW} , emitted by an elliptically polarized GW burst signal can be related to the root-sum-square signal amplitude h_{rss} and the central frequency of the source, f_0 , through the following (Sutton 2013):

$$E_{\text{GW}} = \frac{2}{5} \frac{\pi^2 c^3}{G} D_L^2 f_0^2 h_{\text{rss}}^2, \quad (5)$$

where D_L is the luminosity distance to the source. As the DMs of FRBs provide a measure of the maximum distance, one can use Equation (5) to place 90% upper limits on the GW energy emitted by each FRB source, $E_{\text{GW}}^{90\%}$. This estimate, calculated using $h_{\text{rss}}^{90\%}$, the 90% detection upper limit on the root-sum-squared GW amplitude, is highly dependent on the detector sensitivity and antenna factors at the time of the FRB as well as the central frequency of the simulated waveform injections.

Tables A1 and A2 provide the upper limits on $E_{\text{GW}}^{90\%}$ for SG models and DS2P or WNB GW burst models respectively. These limits assume that the FRB distances are at the lower limits of their inferred distance ranges. Given a large range of models, and since this quantity scales as $h_{\text{rss}}^2 f_0^2$, one would expect the lower-frequency models to provide the most constraining limits. For SG models, the most constraining estimate was 2.5×10^{50} erg for the 70 Hz SG-A model, and for the highest-frequency model considered, SG-H at 1995 Hz, the upper limit was 7.9×10^{54} erg. These values were obtained for the closest inferred burst in the sample, FRB 20190425A. The same burst yielded upper limit values in the range $4.8 - 470 \times 10^{50}$ erg for the WNB model. The DS2P model gave the best constraints, $5.8 - 6.4 \times 10^{54}$ erg, for FRB 20190531B.

For completeness, in Tables A3 and A4, we also provide less constraining limits on $E_{\text{GW}}^{90\%}$ based on the upper credible intervals on the distance of each FRB.

Table 4 lists the repeating bursts that were analyzed in the generic transient search. The most sensitive counterpart to a repeating FRB was for CHIME/FRB event FRB20190825A. The SG injection centered at 1600 Hz (which most closely models an f-mode) was recovered 90% of the time at

Table 3
Details of the FRB Sample and the 90% Exclusion Distances for Each of the Events Considered in This Analysis

FRB Name	UTC Time	R.A.	Decl.	Network	DM (pc cm^{-3})	$D_{L\text{-low}}$ (Mpc)	$D_{L\text{-high}}$ (Mpc)	D_{90} (Mpc)							
								BNS	Generic NSBH	Aligned NSBH	SG C	SG F	ADI A	DS2P A	WNB C
FRB 20190410A	12:19:41	17 ^h 33 ^m 43 ^s	−2°10′	LIV1	270	60	960	160	190	300	36	1.1	15	0.57	6.4
FRB 20190418A	22:34:17	4 ^h 21 ^m 07 ^s	15°27′	V1	180	27	610	40	50	72
FRB 20190419B	22:38:24	17 ^h 02 ^m 02 ^s	86°44′	LIV1	170	25	580	130	170	250	34	1.1	10	0.5	6.2
FRB 20190423B	13:51:43	19 ^h 54 ^m 44 ^s	26°19′	H1V1	590	58	1700	190	250	320	13	0.33	5.6	0.16	3.1
FRB 20190425A	10:47:49	17 ^h 02 ^m 47 ^s	21°30′	HILIV1	130	13	390	240	390	440	66	3.2	27	0.13	21
FRB 20190517B	20:33:37	4 ^h 16 ^m 49 ^s	73°10′	V1	190	20	540	130	230	300
FRB 20190517C	22:06:34	5 ^h 50 ^m 57 ^s	26°34′	LIV1	340	44	1000	40	1.3	10	0.72	7.4
FRB 20190518D	09:04:35	12 ^h 06 ^m 50 ^s	89°25′	HIL1	200	62	850	140	190	220	54	3.2	21	1	16
FRB 20190531B	08:47:40	17 ^h 31 ^m 26 ^s	49°18′	LIV1	170	37	680	210	310	370	56	3.5	23	2.1	20
FRB 20190601C	21:13:28	5 ^h 55 ^m 06 ^s	28°28′	HILIV1	420	200	1700	66	3.2	21	1.1	21
FRB 20190604G	23:12:19	8 ^h 03 ^m 13 ^s	59°32′	LIV1	230	97	1100	14	0.47	8.8	0.3	1.6
FRB 20190605C	02:20:41	11 ^h 14 ^m 04 ^s	−5°18′	LIV1	190	68	890	190	260	370	29	0.94	15	0.59	5.4
FRB 20190606B	22:19:30	7 ^h 14 ^m 42 ^s	86°58′	HILIV1	280	170	1500	44	2.3	18	0.95	15
FRB 20190611A	18:52:42	4 ^h 05 ^m 12 ^s	73°37′	V1	200	19	550	43	57	72
FRB 20190612B	05:30:37	14 ^h 48 ^m 53 ^s	4°21′	HIL1	190	65	920	220	300	410	70	3.3	26	1.1	21
FRB 20190613B	18:56:15	4 ^h 23 ^m 08 ^s	42°37′	HILIV1	290	28	780	270	320	470	78	4.3	28	1.5	23
FRB 20190616A	05:56:30	15 ^h 34 ^m 04 ^s	34°21′	H1V1	210	110	1100	17	0.64	9	0.31	4.3
FRB 20190617A	02:12:33	11 ^h 49 ^m 13 ^s	83°50′	HILIV1	200	62	870	210	310	420	54	2.9	23	1.4	19
FRB 20190618A	11:42:06	21 ^h 24 ^m 28 ^s	25°25′	HIL1	230	78	960	270	360	480	80	4.3	25	1.6	26
FRB 20190621A	02:21:17	12 ^h 06 ^m 36 ^s	74°43′	LIV1	200	78	980	150	220	300	15	0.41	2.2	0.31	2.9
FRB 20190624B	22:11:00	20 ^h 01 ^m 07 ^s	73°34′	H1V1	210	47	820	30	1.3	7.5	0.45	9.2
FRB 20190710A	22:09:19	9 ^h 26 ^m 32 ^s	63°06′	HIL1	200	89	1000	78	4.3	31	1.9	23
FRB 20190713A	02:19:56	1 ^h 35 ^m 49 ^s	72°53′	H1V1	340	140	1400	29	0.9	11	0.39	7
FRB 20190718A	01:11:16	13 ^h 04 ^m 18 ^s	74°14′	HIL1	200	72	970	220	300	410	58	3.5	25	1.6	21
FRB 20190722A	18:30:18	6 ^h 35 ^m 11 ^s	64°17′	LIV1	250	98	1100	18	0.65	11	0.39	2.1
FRB 20190812A	04:35:08	17 ^h 53 ^m 14 ^s	50°48′	HILIV1	250	190	1400	79	4.1	24	1.5	24
FRB 20190903A	12:25:19	3 ^h 12 ^m 01 ^s	21°25′	LIV1	210	67	930	180	260	360	13	0.33	7.3	0.27	3.1
FRB 20190912A	00:50:21	16 ^h 13 ^m 58 ^s	22°13′	LIV1	210	98	1100	15	0.46	9.4	0.29	3.5
FRB 20190912B	08:51:31	0 ^h 15 ^m 57 ^s	6°12′	HIL1	130	23	490	240	300	440	74	3.6	27	1.1	21
FRB 20190912C	09:46:46	1 ^h 13 ^m 16 ^s	67°08′	H1	340	42	1000	190	240	320
FRB 20190913A	15:11:12	6 ^h 40 ^m 02 ^s	39°39′	L1	230	32	710	200	250	330
FRB 20190922A	00:11:04	16 ^h 14 ^m 10 ^s	68°48′	H1V1	200	66	960	140	220	290	16	0.53	3.1	0.19	3.4
FRB 20190928A	21:32:10	14 ^h 00 ^m 25 ^s	80°06′	HILIV1	140	20	510	220	270	370	57	3	22	1.1	19
FRB 20190929B	13:32:01	6 ^h 02 ^m 53 ^s	11°51′	HILIV1	380	150	1500	77	3.9	26	1.7	22

Notes. The TNS name is provided in the first column. The network column lists the GW detector network used: LIGO Hanford (H1), LIGO Livingston (L1), and Virgo (V1). The total DM for each FRB is listed in the DM column, and the 90% credible intervals on the luminosity distance of each burst are provided in columns $D_{L\text{-low}}$ and $D_{L\text{-high}}$. Where the generic transient search (Section 4.2) and the modeled search (Section 4.1) used a different Interferometer network, the network used by the generic transient search is shown in parentheses. The last 8 columns show the 90% confidence exclusion distances for each FRB (D_{90}) for the following emission scenarios: BNS, generic and aligned-spin NSBH from the modeled search, and from the generic transient search, SG-C, SG-F, ADI-A, DS2P-A, and WNB-C; for the latter 5 types of GW bursts, we assume a total radiated energy $E_{\text{GW}} = 10^{-2} M_{\odot} c^2$.

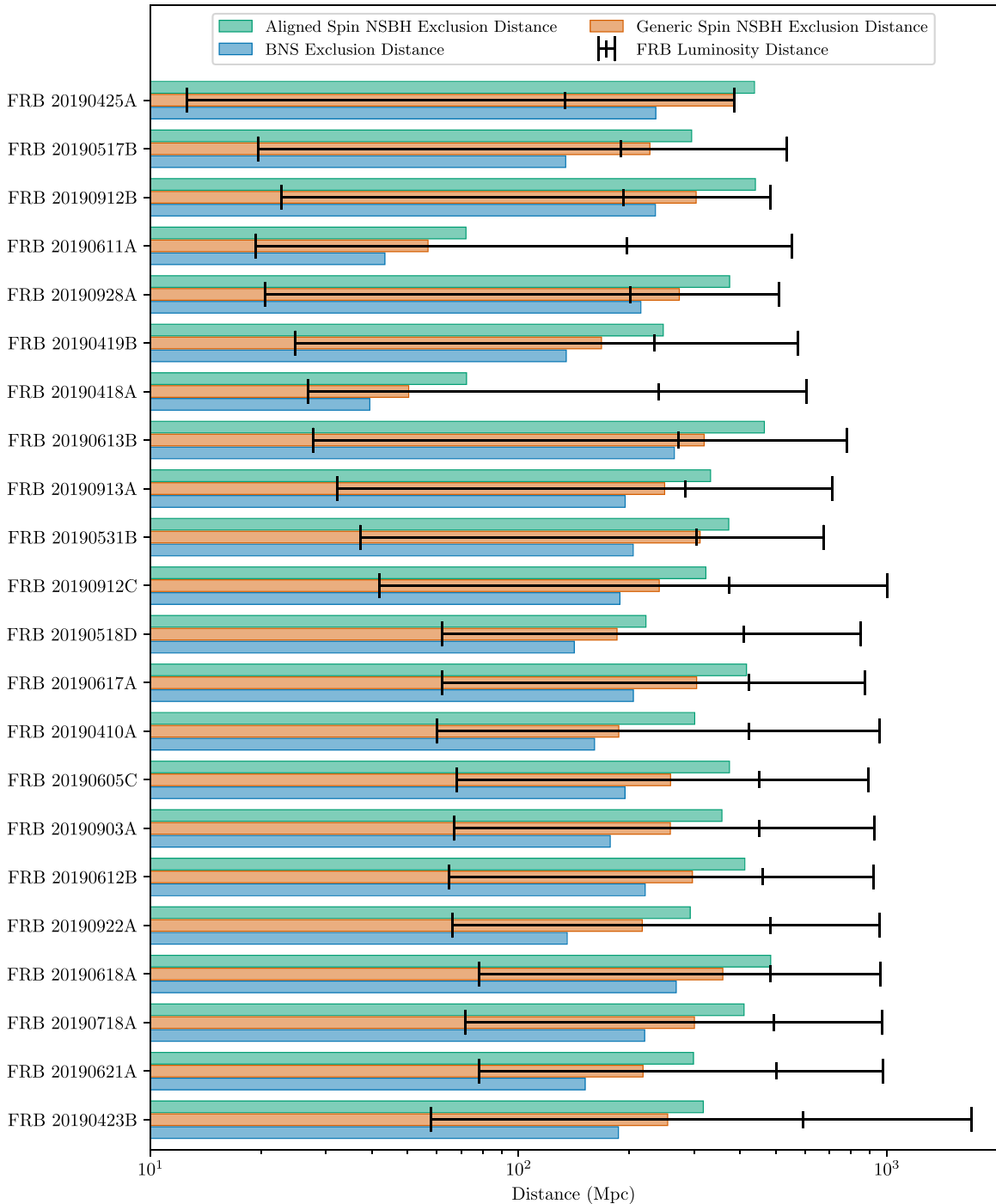


Figure 7. Lower limits on the 90% confidence level exclusion distances for BNS (lower bar), generic spin NSBH (middle bar), and aligned-spin NSBH (upper bar) progenitor systems are shown as found by the modeled search. These are compared to the 90% credible intervals (whisker plot) on the D_L posterior determined by the MCMC method for the FRBs considered in this study.

$h_{\text{rss}} = 2.62 \times 10^{-22}$. The distance to this event is 148.1–149.9 Mpc. This corresponds to an energy upper limit range of 5.83×10^{55} to 5.98×10^{55} erg.

These estimates are well above predictions of the GW emissions through the NS’s fundamental f-mode discussed in Section 2.

6. The M81 Repeater FRB 20200120E

A repeater, FRB 20200120E, which was discovered by CHIME/FRB on 2020 January 20, overlaps with the second part of the third observing run of Advanced LIGO and

Advanced Virgo (O3b), which took place between 2019 October 1 15:00 UTC and 2020 March 27 15:00 UTC. This burst is at 3.6 Mpc, the closest extragalactic FRB so far discovered (Bhardwaj et al. 2021a). This event was shown to be conclusively associated with a globular cluster in the M81 galactic system (Kirsten et al. 2022), which supports the possibility that it was formed from an evolved stellar population such as a compact binary system. Due to the proximity and significance of this burst, we discuss it in this paper, despite it being discovered after O3a.

Table 4
Details of the 3 Repeating FRBs Analyzed in the Generic Transient Search and Their Various Repeating Episodes

FRB Name	UTC Time (s)	R.A.	Decl.	Network	DM (pc cm ⁻³)	D_L -low (Mpc)	D_L -high (Mpc)
FRB20190817A	14:39:52	4 ^h 21 ^m 08 ^s	73°47′	H1L1V1	190	19	540
FRB20190929C	11:58:29	4 ^h 22 ^m 25 ^s	73°40′	H1L1V1	190	21	550
FRB20190518A	18:13:33	1 ^h 58 ^m 14 ^s	65°46′	L1V1	350.5	148.1	149.9
FRB20190518E	18:20:57	1 ^h 57 ^m 50 ^s	65°43′	L1V1	350.0	148.1	149.9
FRB20190519A	17:50:16	1 ^h 43 ^m 44 ^s	65°48′	H1V1	350.0	148.1	149.9
FRB20190519C	18:10:41	1 ^h 58 ^m 00 ^s	65°47′	H1V1	348.8	148.1	149.9
FRB20190809A	12:50:40	1 ^h 58 ^m 16 ^s	65°43′	H1L1	356.2	148.1	149.9
FRB20190825A	11:48:18	1 ^h 58 ^m 07 ^s	65°42′	H1L1	349.6	148.1	149.9
FRB20190825B	11:51:54	1 ^h 58 ^m 04 ^s	65°23′	H1L1	349.9	148.1	149.9
FRB20190421A	08:00:04	13 ^h 51 ^m 57 ^s	48°10′	H1L1V1	230	130	1300
FRB20190702B	03:14:36	13 ^h 52 ^m 25 ^s	48°15′	L1V1	220	130	1300

Notes. The TNS name is provided in the first column. The network column lists the GW detector network used: LIGO Hanford (H1), LIGO Livingston (L1), and Virgo (V1). The total DM for each FRB is listed in the DM column, and the 90% credible intervals on the luminosity distance are provided in columns D_L -low and D_L -high. 11 total events were analyzed for the three different FRB repeaters considered. For FRB 20190518A and its associated repeats, we list only the distance of Marcote et al. (2020) obtained by galaxy localization.

The burst FRB 20200120E was shown to repeat at least 4 times. Two of the repeats occurred after O3b; another episode, despite being consistent with the localization of the other associated bursts, had no intensity data saved. Therefore, we discuss here only the initial burst FRB 20200120E, for which GW data exists.

At the time of FRB 20200120E, only H1 data were available; thus, a generic transient search was not conducted. Likewise, since this is a repeating event, it does not pass our criteria for conducting a modeled search. Due to these restrictions, only a RAVEN coincidence search was conducted within a $[-6000, +6000]$ s time window. No coincidences were found with sufficient significance as determined by the coincident false-alarm rate. Given the relative close proximity of this burst, further repeat emissions will be of interest for GW follow-up during the fourth observing run of Advanced LIGO, Advanced Virgo, and Kagra (O4; Abbott et al. 2020a) when constraints on the energy emitted in GWs will be of order 10^{50} at around 500 Hz.

7. Conclusions

We performed a targeted search for GWs associated with FRBs detected by the CHIME/FRB project during O3a. As the sources of nonrepeating FRBs are currently not known, we ran both a modeled search for BNS and NSBH signals (Harry & Fairhurst 2011; Williamson et al. 2014) and a generic transient search for generic GW transient signals (Sutton et al. 2010; Was et al. 2012).

Our searches found no significant GW event candidates in association with the analyzed FRBs. We set 90% confidence lower bounds on the distances to FRB progenitors for several different emission models. Additionally, we present 90% credible intervals on the luminosity distance, D_L , inferred from the DM measurement of each FRB source.

The D_L information can be used to test models based on the simulated injections used for calculating the D_{90} values of each FRB. However, the significant uncertainties in the relative contributions to the total DM for each FRB produce relatively wide credible intervals for the D_L posteriors. We find no FRB event can be fully excluded from any of the models we have

considered due to some posterior support on D_L existing for the FRB outside the detection range of the analyses performed.

The results, however, as illustrated in Figure 7, indicate that the GW network’s detection range is advancing into cosmological volumes where FRB emissions are expected. This is encouraging as we look forward to future GW searches at higher sensitivity. Furthermore, the redshifts obtained from the ongoing efforts to localize host galaxies (there are currently 18 FRBs with an associated host galaxy; see³¹⁹) could significantly improve the chances of constraining progenitor populations (Heintz et al. 2020; Bhandari et al. 2022).

The distance estimates for each FRB allowed us to place 90% upper limits on the GW energy emitted by each FRB source, $E_{GW}^{90\%}$. For each nonrepeating FRB analyzed with a generic transient search, we provided limits on $E_{GW}^{90\%}$ for a range of emission models. Repeating FRBs were also analyzed to determine 90% upper limits on the energy emitted through GWs. For the most sensitive repeating FRB analysis in our sample, we find an energy upper limit range of 5.83×10^{54} to 5.98×10^{55} erg, well above the predictions for GW emissions from the fundamental f-modes of NSs. Based on Equation (5), an FRB event such as that associated with SGR 1935+2154 occurring during O3a would have allowed the search to probe the more optimistic of these estimates allowing limits, $E_{GW} \sim 10^{47}$ erg, assuming a generic burst waveform emitting at roughly 1 kHz at 10 kpc.

We also analyzed the repeater, FRB 20200120E, discovered on 2020 January 20 during O3b. A RAVEN (Urban 2016; Cho 2019) coincidence search for any previously detected compact binary coalescence GW events was conducted within a $[-6000, +6000]$ s time window around the first burst of this repeater. No coincidences were found with sufficient significance to be distinguished from random coincidences, as determined by the computed joint false-alarm rate from the two samples.

A comparison of the expected volumetric rates is one avenue to yield insights on possible associations between two transient source populations. An analysis of the most recent Gravitational Wave Transient Catalog 3 (GWTC-3 The LIGO

³¹⁹ <http://frbhosts.org/>

Scientific Collaboration et al. 2021, 2023) has inferred merger rates in the ranges $10\text{--}1700\text{ Gpc}^{-3}\text{ yr}^{-1}$ for BNS and $7.8\text{--}140\text{ Gpc}^{-3}\text{ yr}^{-1}$ for NSBH populations. These estimates are significantly lower than estimates of the FRB rate $3.5_{-2.4}^{+5.7} \times 10^4\text{ Gpc}^{-3}\text{ yr}^{-1}$ provided by Luo et al. (2020) for sources above $10^{42}\text{ erg s}^{-1}$. Based on these numbers, the percentage of FRBs that could possibly be associated with BNSs is at most 15%, and for NSBH sources, the percentage is 1%. As noted by Luo et al. (2020), if BNS and/or NSBH sources were only associated with FRBs from the high end of the luminosity function ($>10^{43}\text{ erg s}^{-1}$), such rates could be comparable.

However, there are a number of unknown factors that complicate reconciling the GW and FRB source populations; these include the proportion of FRBs that may repeat or the possible effects of beaming (Ravi 2019; Connor et al. 2020).

Probing the local population of FRBs through targeted searches, the strategy adopted in this study can constrain associations between GW sources and FRBs. The distance uncertainties in the FRB sample are a particular obstacle, and ongoing efforts to identify FRB host galaxies (Chatterjee et al. 2017) could provide valuable prior information for FRBs discovered within the BNS and/or NSBH detection range of future searches.

CHIME/FRB is deploying a set of Outrigger telescopes located at sufficient distances to allow autonomous very-long-baseline interferometry on CHIME/FRB detected bursts (Cassanelli et al. 2022; Mena-Parra et al. 2022). This development promises subarcsecond localizations on hundreds of FRBs per year allowing host galaxy identification and redshift determination through optical follow-ups or through cross matching of positional data with photometric galaxy surveys (Shin et al. 2023). The resulting sample of FRBs at low redshift will be a significant development for GW detection networks, particularly as the sensitive volume increases with future observation runs and should allow targeted searches to obtain statistical evidence toward supporting or ruling out GW–FRB associations.

Acknowledgments

This material is based upon work supported by NSF’s LIGO Laboratory, which is a major facility fully funded by the National Science Foundation. The authors also gratefully acknowledge the support of the Science and Technology Facilities Council (STFC) of the United Kingdom, the Max-Planck-Society (MPS), and the State of Niedersachsen/Germany for support of the construction of Advanced LIGO and construction and operation of the GEO 600 detector. Additional support for Advanced LIGO was provided by the Australian Research Council. The authors gratefully acknowledge the Italian Istituto Nazionale di Fisica Nucleare (INFN), the French Centre National de la Recherche Scientifique (CNRS), and the Netherlands Organization for Scientific Research (NWO), for the construction and operation of the Virgo detector and the creation and support of the EGO consortium. The authors also gratefully acknowledge research support from these agencies as well as by the Council of Scientific and Industrial Research of India, the Department of Science and Technology, India, the Science & Engineering Research Board (SERB), India, the Ministry of Human Resource Development, India, the Spanish Agencia Estatal de Investigación (AEI), the Spanish Ministerio de Ciencia e

Innovación and Ministerio de Universidades, the Conselleria de Fons Europeus, Universitat i Cultura and the Direcció General de Política Universitaria i Recerca del Govern de les Illes Balears, the Conselleria d’Innovació Universitats, Ciència i Societat Digital de la Generalitat Valenciana and the CERCA Programme Generalitat de Catalunya, Spain, the National Science Centre of Poland and the European Union—European Regional Development Fund; Foundation for Polish Science (FNP), the Swiss National Science Foundation (SNSF), the Russian Foundation for Basic Research, the Russian Science Foundation, the European Commission, the European Social Funds (ESF), the European Regional Development Funds (ERDF), the Royal Society, the Scottish Funding Council, the Scottish Universities Physics Alliance, the Hungarian Scientific Research Fund (OTKA), the French Lyon Institute of Origins (LIO), the Belgian Fonds de la Recherche Scientifique (FRS-FNRS), Actions de Recherche Concertées (ARC) and Fonds Wetenschappelijk Onderzoek—Vlaanderen (FWO), Belgium, the Paris Île-de-France Region, the National Research, Development and Innovation Office Hungary (NKFIH), the National Research Foundation of Korea, the National Science and Engineering Research Council Canada, Canadian Foundation for Innovation (CFI), the Brazilian Ministry of Science, Technology, and Innovations, the International Center for Theoretical Physics South American Institute for Fundamental Research (ICTP-SAIFR), the Research Grants Council of Hong Kong, the National Natural Science Foundation of China (NSFC), the Leverhulme Trust, the Research Corporation, the Ministry of Science and Technology (MOST), Taiwan, the United States Department of Energy, and the Kavli Foundation. The authors gratefully acknowledge the support of the NSF, STFC, INFN, and CNRS for provision of computational resources.

This work was supported by MEXT, JSPS Leading-edge Research Infrastructure Program, JSPS Grant-in-Aid for Specially Promoted Research 26000005, JSPS Grant-in-Aid for Scientific Research on Innovative Areas 2905 (JP17H06358, JP17H06361, and JP17H0636), JSPS Core-to-Core Program (A) Advanced Research Networks, JSPS Grant-in-Aid for Scientific Research (S) 17H06133 and 20H05639, JSPS Grant-in-Aid for Transformative Research Areas (A) 20A203 (JP20H05854), the joint research program of the Institute for Cosmic Ray Research, University of Tokyo, National Research Foundation (NRF), Computing Infrastructure Project of KISTI-GSDC, Korea Astronomy and Space Science Institute (KASI), and Ministry of Science and ICT (MSIT) in Korea, Academia Sinica (AS), AS Grid Center (ASGC) and the Ministry of Science and Technology (MoST) in Taiwan under grants including AS-CDA-105-M06, Advanced Technology Center (ATC) of NAOJ, and Mechanical Engineering Center of Kō Enerugi Kasokuki Kenkyū Kikō (KEK).

We acknowledge that CHIME is located on the traditional, ancestral, and unceded territory of the Syilx and Okanagan people.

We thank the Dominion Radio Astrophysical Observatory, operated by the National Research Council Canada, for gracious hospitality and expertise. CHIME is funded by a grant from the Canada Foundation for Innovation (CFI) 2012 Leading Edge Fund (Project 31170) and by contributions from the provinces of British Columbia, Québec, and Ontario. The CHIME/FRB Project is funded by a grant from the CFI 2015 Innovation Fund (Project 33213) and by contributions from the provinces of British Columbia and Québec, and by the Dunlap

Institute for Astronomy and Astrophysics at the University of Toronto. Additional support was provided by the Canadian Institute for Advanced Research (CIFAR), McGill University and the McGill Space Institute via the Trottier Family Foundation, and the University of British Columbia. The Dunlap Institute is funded through an endowment established by the David Dunlap family and the University of Toronto. Research at Perimeter Institute is supported by the Government of Canada through Industry Canada and by the Province of Ontario through the Ministry of Research & Innovation. The National Radio Astronomy Observatory is a facility of the National Science Foundation (NSF) operated under cooperative agreement by Associated Universities, Inc. FRB research at UBC is supported by an NSERC Discovery Grant and by the Canadian Institute for Advanced Research. The CHIME/FRB baseband system is funded in part by a CFI John R. Evans Leaders Fund award to IHS.

We would like to thank all of the essential workers who put their health at risk during the COVID-19 pandemic, without whom we would not have been able to complete this work.

Appendix

Tables of Upper Limits on the Energy Emitted through GWs for the Generic Transient Search

This section provides the supplemental tables containing the upper limits on the energy emitted through GWs for the generic transient search for different waveform models and luminosity distance estimates. Tables A1 and A2 provide the upper limits on $E_{\text{GW}}^{90\%}$ for SG models and DS2P or WNB GW burst models respectively. These limits assume that the FRB distances are at the lower limits of their inferred distance ranges. Tables A3 and A4 provide less constraining limits on $E_{\text{GW}}^{90\%}$ based on the upper credible intervals on the distance of each FRB.

Table A1

The Upper Limits on the Energy Emitted through GWs in erg for the Generic Transient Search Using the SG Waveforms Described in Table 1

FRB	D_L (Mpc)	SG A	SG B	SG C	SG D	SG E	SG F	SG G	SG H
FRB 20190410A	6.0×10^1	1.5×10^{52}	2.8×10^{52}	4.9×10^{52}	4.1×10^{53}	5.5×10^{54}	5.4×10^{55}	3.0×10^{56}	1.1×10^{57}
FRB 20190419B	2.5×10^1	2.6×10^{51}	4.3×10^{51}	9.7×10^{51}	5.9×10^{52}	9.4×10^{53}	8.9×10^{54}	5.0×10^{55}	1.5×10^{58}
FRB 20190423B	5.8×10^1	5.9×10^{52}	8.9×10^{52}	3.7×10^{53}	3.7×10^{54}	4.6×10^{55}	5.6×10^{56}	3.4×10^{57}	1.1×10^{58}
FRB 20190425A	1.3×10^1	2.5×10^{50}	3.5×10^{50}	6.5×10^{50}	3.4×10^{51}	2.6×10^{52}	2.7×10^{53}	1.6×10^{54}	7.9×10^{54}
FRB 20190517C	4.4×10^1	5.8×10^{51}	8.8×10^{51}	2.2×10^{52}	1.3×10^{53}	2.3×10^{54}	2.1×10^{55}	9.8×10^{55}	3.5×10^{56}
FRB 20190518D	6.2×10^1	9.5×10^{51}	1.3×10^{52}	2.3×10^{52}	9.5×10^{52}	1.1×10^{54}	6.8×10^{54}	3.6×10^{55}	2.0×10^{56}
FRB 20190531B	3.7×10^1	3.2×10^{51}	3.4×10^{51}	7.9×10^{51}	3.3×10^{52}	2.5×10^{53}	2.0×10^{54}	8.1×10^{54}	3.1×10^{55}
FRB 20190601C	2.0×10^2	8.6×10^{52}	1.1×10^{53}	1.6×10^{53}	6.3×10^{53}	1.1×10^{55}	6.8×10^{55}	4.8×10^{56}	1.5×10^{57}
FRB 20190604G	9.7×10^1	1.1×10^{53}	3.2×10^{53}	9.0×10^{53}	3.7×10^{54}	8.7×10^{55}	7.5×10^{56}	3.2×10^{57}	1.2×10^{58}
FRB 20190605C	6.8×10^1	3.0×10^{52}	2.8×10^{52}	1.0×10^{53}	5.2×10^{53}	8.7×10^{54}	9.4×10^{55}	5.2×10^{56}	1.6×10^{57}
FRB 20190606B	1.7×10^2	1.7×10^{53}	1.3×10^{53}	2.7×10^{53}	8.2×10^{53}	1.1×10^{55}	9.6×10^{55}	3.6×10^{56}	1.4×10^{57}
FRB 20190612B	6.5×10^1	8.2×10^{51}	8.5×10^{51}	1.5×10^{52}	7.3×10^{52}	8.0×10^{53}	7.0×10^{54}	3.7×10^{55}	3.6×10^{56}
FRB 20190613B	2.8×10^1	1.2×10^{51}	1.0×10^{51}	2.2×10^{51}	1.3×10^{52}	9.3×10^{52}	7.4×10^{53}	4.2×10^{54}	1.8×10^{55}
FRB 20190616A	1.1×10^2	1.9×10^{53}	2.1×10^{53}	6.9×10^{53}	3.1×10^{54}	3.5×10^{55}	5.1×10^{56}	2.8×10^{57}	8.2×10^{57}
FRB 20190617A	6.2×10^1	9.5×10^{51}	1.3×10^{52}	2.4×10^{52}	9.2×10^{52}	9.2×10^{53}	8.3×10^{54}	4.2×10^{55}	8.8×10^{55}
FRB 20190618A	7.8×10^1	6.0×10^{51}	7.7×10^{51}	1.7×10^{52}	7.0×10^{52}	6.8×10^{53}	5.9×10^{54}	3.0×10^{55}	1.4×10^{56}
FRB 20190621A	7.8×10^1	1.1×10^{53}	1.2×10^{53}	4.6×10^{53}	1.5×10^{54}	5.4×10^{55}	6.5×10^{56}	1.7×10^{57}	4.9×10^{57}
FRB 20190624B	4.7×10^1	1.3×10^{52}	1.9×10^{52}	4.2×10^{52}	1.7×10^{53}	2.9×10^{54}	2.3×10^{55}	1.5×10^{56}	8.3×10^{56}
FRB 20190710A	8.9×10^1	1.1×10^{52}	1.6×10^{52}	2.3×10^{52}	1.0×10^{53}	9.4×10^{53}	7.6×10^{54}	3.3×10^{55}	1.4×10^{56}
FRB 20190713A	1.4×10^2	1.2×10^{53}	1.6×10^{53}	4.3×10^{53}	2.3×10^{54}	4.2×10^{55}	4.4×10^{56}	2.2×10^{57}	6.7×10^{57}
FRB 20190718A	7.2×10^1	1.1×10^{52}	1.1×10^{52}	2.8×10^{52}	1.1×10^{53}	1.1×10^{54}	7.7×10^{54}	3.1×10^{55}	1.2×10^{56}
FRB 20190722A	9.8×10^1	7.0×10^{52}	1.3×10^{53}	5.0×10^{53}	3.3×10^{54}	5.4×10^{55}	4.0×10^{56}	1.6×10^{57}	9.6×10^{57}
FRB 20190812A	1.9×10^2	3.7×10^{52}	4.1×10^{52}	9.9×10^{52}	4.3×10^{53}	4.3×10^{54}	3.7×10^{55}	1.6×10^{56}	5.8×10^{56}
FRB 20190903A	6.7×10^1	9.0×10^{52}	9.8×10^{52}	5.0×10^{53}	4.4×10^{54}	5.5×10^{55}	7.4×10^{56}	3.4×10^{57}	9.2×10^{57}
FRB 20190912A	9.8×10^1	1.2×10^{53}	2.0×10^{53}	7.9×10^{53}	4.6×10^{54}	1.0×10^{56}	8.1×10^{56}	3.8×10^{57}	1.7×10^{58}
FRB 20190912B	2.3×10^1	7.1×10^{50}	9.1×10^{50}	1.7×10^{51}	8.1×10^{51}	6.9×10^{52}	7.1×10^{53}	3.9×10^{54}	1.5×10^{55}
FRB 20190922A	6.6×10^1	5.1×10^{52}	7.7×10^{52}	3.1×10^{53}	1.5×10^{54}	2.4×10^{55}	2.8×10^{56}	1.5×10^{57}	4.7×10^{57}
FRB 20190928A	2.0×10^1	9.9×10^{50}	1.1×10^{51}	2.3×10^{51}	9.2×10^{51}	1.1×10^{53}	8.2×10^{53}	3.7×10^{54}	1.4×10^{55}
FRB 20190929B	1.5×10^2	2.9×10^{52}	3.9×10^{52}	6.7×10^{52}	3.4×10^{53}	2.8×10^{54}	2.6×10^{55}	1.2×10^{56}	4.0×10^{56}

Note. The distances represent the lower bounds of 90% credible intervals from the MCMC inference described in Section 3.

Table A2

The Upper Limits on the Energy Emitted through GWs in erg for the Generic Transient Search Using the DS2P and WNB Waveforms Described in Table 1

FRB	D_L (Mpc)	DS2P A	DS2P B	WNB A	WNB B	WNB C	WNB D
FRB 20190410A	6.0×10^1	2.0×10^{56}	1.8×10^{56}	1.2×10^{53}	9.5×10^{52}	3.4×10^{54}	1.0×10^{55}
FRB 20190419B	2.5×10^1	4.4×10^{55}	3.0×10^{55}	1.6×10^{54}	1.8×10^{52}	6.0×10^{53}	1.7×10^{54}
FRB 20190423B	5.8×10^1	2.4×10^{57}	2.6×10^{57}	2.8×10^{53}	3.0×10^{53}	1.4×10^{55}	3.6×10^{55}
FRB 20190425A	1.3×10^1	1.7×10^{56}	4.6×10^{54}	4.8×10^{50}	7.9×10^{50}	1.4×10^{52}	4.7×10^{52}
FRB 20190517C	4.4×10^1	6.7×10^{55}	5.8×10^{55}	2.4×10^{52}	3.1×10^{52}	1.4×10^{54}	7.3×10^{54}
FRB 20190518D	6.2×10^1	6.7×10^{55}	1.1×10^{56}	2.0×10^{52}	2.6×10^{52}	5.8×10^{53}	1.7×10^{54}
FRB 20190531B	3.7×10^1	5.8×10^{54}	6.4×10^{54}	5.7×10^{51}	8.6×10^{51}	1.4×10^{53}	5.6×10^{53}
FRB 20190601C	2.0×10^2	5.5×10^{56}	8.3×10^{56}	1.2×10^{53}	1.6×10^{53}	3.4×10^{54}	8.6×10^{54}
FRB 20190604G	9.7×10^1	1.9×10^{57}	1.6×10^{57}	...	4.9×10^{54}	1.5×10^{56}	3.4×10^{56}
FRB 20190605C	6.8×10^1	2.4×10^{56}	1.7×10^{56}	3.5×10^{53}	1.6×10^{53}	6.2×10^{54}	1.8×10^{55}
FRB 20190606B	1.7×10^2	5.7×10^{56}	9.9×10^{56}	3.6×10^{53}	2.0×10^{53}	4.7×10^{54}	1.3×10^{55}
FRB 20190612B	6.5×10^1	6.2×10^{55}	1.1×10^{58}	1.3×10^{52}	2.1×10^{52}	3.7×10^{53}	1.2×10^{54}
FRB 20190613B	2.8×10^1	6.2×10^{54}	1.1×10^{55}	1.6×10^{51}	2.5×10^{51}	5.4×10^{52}	1.6×10^{53}
FRB 20190616A	1.1×10^2	2.2×10^{57}	2.7×10^{57}	1.1×10^{54}	7.3×10^{53}	2.4×10^{55}	1.4×10^{56}
FRB 20190617A	6.2×10^1	3.6×10^{55}	5.1×10^{55}	3.3×10^{52}	2.7×10^{52}	3.9×10^{53}	1.6×10^{54}
FRB 20190618A	7.8×10^1	4.4×10^{55}	7.0×10^{55}	9.9×10^{51}	1.8×10^{52}	3.6×10^{53}	1.2×10^{54}
FRB 20190621A	7.8×10^1	1.1×10^{57}	4.8×10^{56}	...	9.3×10^{53}	2.8×10^{55}	5.9×10^{55}
FRB 20190624B	4.7×10^1	1.9×10^{56}	3.6×10^{56}	2.8×10^{52}	4.4×10^{52}	1.0×10^{54}	3.7×10^{54}
FRB 20190710A	8.9×10^1	3.9×10^{55}	4.3×10^{55}	1.7×10^{52}	2.6×10^{52}	5.6×10^{53}	1.6×10^{54}
FRB 20190713A	1.4×10^2	2.3×10^{57}	3.7×10^{57}	3.1×10^{53}	5.0×10^{53}	1.5×10^{55}	4.4×10^{55}
FRB 20190718A	7.2×10^1	3.7×10^{55}	6.1×10^{55}	1.7×10^{52}	2.3×10^{52}	4.6×10^{53}	1.4×10^{54}
FRB 20190722A	9.8×10^1	1.1×10^{57}	8.0×10^{56}	9.2×10^{55}	2.7×10^{54}	8.2×10^{55}	1.8×10^{56}
FRB 20190812A	1.9×10^2	2.7×10^{56}	5.3×10^{56}	8.2×10^{52}	1.1×10^{53}	2.4×10^{54}	7.1×10^{54}
FRB 20190903A	6.7×10^1	1.1×10^{57}	7.3×10^{56}	5.0×10^{53}	3.6×10^{53}	1.7×10^{55}	4.5×10^{55}
FRB 20190912A	9.8×10^1	2.0×10^{57}	1.5×10^{57}	7.9×10^{53}	6.6×10^{53}	2.9×10^{55}	8.9×10^{55}
FRB 20190912B	2.3×10^1	7.6×10^{54}	1.4×10^{55}	1.4×10^{51}	1.7×10^{51}	4.3×10^{52}	1.2×10^{53}
FRB 20190922A	6.6×10^1	2.2×10^{57}	3.2×10^{57}	1.5×10^{54}	4.2×10^{53}	1.5×10^{55}	3.9×10^{55}
FRB 20190928A	2.0×10^1	6.2×10^{54}	1.1×10^{55}	1.8×10^{51}	2.6×10^{51}	4.3×10^{52}	1.7×10^{53}
FRB 20190929B	1.5×10^2	1.4×10^{56}	3.0×10^{56}	6.6×10^{52}	7.3×10^{52}	1.8×10^{54}	4.7×10^{54}

Note. The distances represent the lower bounds of 90% credible intervals from the MCMC inference described in Section 3.

Table A3

As for Table A1 but with Distances Based on the Upper Bounds of 90% Credible Intervals on the Luminosity Distance

FRB	D_L (Mpc)	SG A	SG B	SG C	SG D	SG E	SG F	SG G	SG H
FRB 20190410A	9.6×10^2	3.9×10^{54}	7.2×10^{54}	1.2×10^{55}	1.0×10^{56}	1.4×10^{57}	1.4×10^{58}	7.5×10^{58}	2.7×10^{59}
FRB 20190419B	5.8×10^2	1.4×10^{54}	2.3×10^{54}	5.2×10^{54}	3.2×10^{55}	5.1×10^{56}	4.8×10^{57}	2.7×10^{58}	8.0×10^{60}
FRB 20190423B	1.7×10^3	5.1×10^{55}	7.7×10^{55}	3.2×10^{56}	3.2×10^{57}	4.0×10^{58}	4.9×10^{59}	2.9×10^{60}	9.4×10^{60}
FRB 20190425A	3.9×10^2	2.4×10^{53}	3.3×10^{53}	6.1×10^{53}	3.2×10^{54}	2.4×10^{55}	2.5×10^{56}	1.6×10^{57}	7.5×10^{57}
FRB 20190517C	1.0×10^3	3.1×10^{54}	4.7×10^{54}	1.2×10^{55}	6.8×10^{55}	1.2×10^{57}	1.1×10^{58}	5.3×10^{58}	1.9×10^{59}
FRB 20190518D	8.5×10^2	1.8×10^{54}	2.4×10^{54}	4.4×10^{54}	1.8×10^{55}	2.0×10^{56}	1.3×10^{57}	6.9×10^{57}	3.8×10^{58}
FRB 20190531B	6.8×10^2	1.0×10^{54}	1.1×10^{54}	2.6×10^{54}	1.1×10^{55}	8.2×10^{55}	6.7×10^{56}	2.7×10^{57}	1.0×10^{58}
FRB 20190601C	1.7×10^3	6.6×10^{54}	8.3×10^{54}	1.2×10^{55}	4.8×10^{55}	8.2×10^{56}	5.2×10^{57}	3.6×10^{58}	1.1×10^{59}
FRB 20190604G	1.1×10^3	1.5×10^{55}	4.5×10^{55}	1.3×10^{56}	5.1×10^{56}	1.2×10^{58}	1.0×10^{59}	4.5×10^{59}	1.6×10^{60}
FRB 20190605C	8.9×10^2	5.1×10^{54}	4.9×10^{54}	1.7×10^{55}	8.9×10^{55}	1.5×10^{57}	1.6×10^{58}	8.9×10^{58}	2.7×10^{59}
FRB 20190606B	1.5×10^3	1.3×10^{55}	9.6×10^{54}	2.0×10^{55}	6.2×10^{55}	8.3×10^{56}	7.3×10^{57}	2.7×10^{58}	1.0×10^{59}
FRB 20190612B	9.2×10^2	1.7×10^{54}	1.7×10^{54}	3.1×10^{54}	1.5×10^{55}	1.6×10^{56}	1.4×10^{57}	7.4×10^{57}	7.3×10^{58}
FRB 20190613B	7.8×10^2	9.7×10^{53}	8.2×10^{53}	1.8×10^{54}	1.0×10^{55}	7.4×10^{55}	5.8×10^{56}	3.4×10^{57}	1.4×10^{58}
FRB 20190616A	1.1×10^3	2.1×10^{55}	2.4×10^{55}	7.6×10^{55}	3.4×10^{56}	3.9×10^{57}	5.6×10^{58}	3.1×10^{59}	9.0×10^{59}
FRB 20190617A	8.7×10^2	1.9×10^{54}	2.5×10^{54}	4.7×10^{54}	1.8×10^{55}	1.8×10^{56}	1.6×10^{57}	8.2×10^{57}	1.7×10^{58}
FRB 20190618A	9.6×10^2	9.1×10^{53}	1.2×10^{54}	2.6×10^{54}	1.1×10^{55}	1.0×10^{56}	9.0×10^{56}	4.5×10^{57}	2.1×10^{58}
FRB 20190621A	9.8×10^2	1.7×10^{55}	2.0×10^{55}	7.2×10^{55}	2.3×10^{56}	8.4×10^{57}	1.0×10^{59}	2.6×10^{59}	7.7×10^{59}
FRB 20190624B	8.2×10^2	4.0×10^{54}	5.8×10^{54}	1.3×10^{55}	5.1×10^{55}	8.9×10^{56}	7.0×10^{57}	4.6×10^{58}	2.5×10^{59}
FRB 20190710A	1.0×10^3	1.4×10^{54}	2.0×10^{54}	2.9×10^{54}	1.2×10^{55}	1.2×10^{56}	9.5×10^{56}	4.1×10^{57}	1.7×10^{58}
FRB 20190713A	1.4×10^3	1.2×10^{55}	1.6×10^{55}	4.4×10^{55}	2.4×10^{56}	4.4×10^{57}	4.6×10^{58}	2.2×10^{59}	6.9×10^{59}
FRB 20190718A	9.7×10^2	2.0×10^{54}	2.1×10^{54}	5.1×10^{54}	2.0×10^{55}	1.9×10^{56}	1.4×10^{57}	5.8×10^{57}	2.3×10^{58}
FRB 20190722A	1.1×10^3	9.4×10^{54}	1.7×10^{55}	6.7×10^{55}	4.4×10^{56}	7.2×10^{57}	5.3×10^{58}	2.2×10^{59}	1.3×10^{60}
FRB 20190812A	1.4×10^3	2.0×10^{54}	2.2×10^{54}	5.3×10^{54}	2.3×10^{55}	2.3×10^{56}	2.0×10^{57}	8.7×10^{57}	3.1×10^{58}
FRB 20190903A	9.3×10^2	1.7×10^{55}	1.9×10^{55}	9.6×10^{55}	8.4×10^{56}	1.0×10^{58}	1.4×10^{59}	6.5×10^{59}	1.8×10^{60}
FRB 20190912A	1.1×10^3	1.5×10^{55}	2.5×10^{55}	9.9×10^{55}	5.8×10^{56}	1.2×10^{58}	1.0×10^{59}	4.7×10^{59}	2.2×10^{60}
FRB 20190912B	4.9×10^2	3.2×10^{53}	4.1×10^{53}	7.7×10^{53}	3.7×10^{54}	3.1×10^{55}	3.3×10^{56}	1.8×10^{57}	6.7×10^{57}
FRB 20190922A	9.6×10^2	1.1×10^{55}	1.6×10^{55}	6.6×10^{55}	3.2×10^{56}	5.0×10^{57}	5.9×10^{58}	3.2×10^{59}	9.8×10^{59}
FRB 20190928A	5.1×10^2	6.1×10^{53}	6.9×10^{53}	1.5×10^{54}	5.7×10^{54}	6.6×10^{55}	5.1×10^{56}	2.3×10^{57}	8.4×10^{57}
FRB 20190929B	1.5×10^3	3.0×10^{54}	4.1×10^{54}	7.1×10^{54}	3.6×10^{55}	3.0×10^{56}	2.8×10^{57}	1.3×10^{58}	4.2×10^{58}

Table A4
As for Table A2 but with Distances Based on the Upper Bounds of 90% Credible Intervals on the Luminosity Distance

FRB	D_L (Mpc)	DS2P A	DS2P B	WNB A	WNB B	WNB C	WNB D
FRB 20190410A	9.6×10^2	5.0×10^{58}	4.5×10^{58}	3.2×10^{55}	2.4×10^{55}	8.6×10^{56}	2.5×10^{57}
FRB 20190419B	5.8×10^2	2.3×10^{58}	1.6×10^{58}	8.3×10^{56}	9.5×10^{54}	3.2×10^{56}	9.0×10^{56}
FRB 20190423B	1.7×10^3	2.1×10^{60}	2.2×10^{60}	2.4×10^{56}	2.6×10^{56}	1.2×10^{58}	3.2×10^{58}
FRB 20190425A	3.9×10^2	1.6×10^{59}	4.4×10^{57}	4.5×10^{53}	7.4×10^{53}	1.3×10^{55}	4.4×10^{55}
FRB 20190517C	1.0×10^3	3.6×10^{58}	3.2×10^{58}	1.3×10^{55}	1.7×10^{55}	7.5×10^{56}	4.0×10^{57}
FRB 20190518D	8.5×10^2	1.3×10^{58}	2.1×10^{58}	3.7×10^{54}	4.9×10^{54}	1.1×10^{56}	3.2×10^{56}
FRB 20190531B	6.8×10^2	1.9×10^{57}	2.1×10^{57}	1.9×10^{54}	2.9×10^{54}	4.5×10^{55}	1.8×10^{56}
FRB 20190601C	1.7×10^3	4.2×10^{58}	6.4×10^{58}	9.4×10^{54}	1.2×10^{55}	2.6×10^{56}	6.6×10^{56}
FRB 20190604G	1.1×10^3	2.6×10^{59}	2.2×10^{59}	...	6.8×10^{56}	2.0×10^{58}	4.7×10^{58}
FRB 20190605C	8.9×10^2	4.1×10^{58}	2.9×10^{58}	5.9×10^{55}	2.7×10^{55}	1.1×10^{57}	3.0×10^{57}
FRB 20190606B	1.5×10^3	4.3×10^{58}	7.5×10^{58}	2.7×10^{55}	1.5×10^{55}	3.6×10^{56}	9.7×10^{56}
FRB 20190612B	9.2×10^2	1.3×10^{58}	2.2×10^{60}	2.7×10^{54}	4.2×10^{54}	7.5×10^{55}	2.5×10^{56}
FRB 20190613B	7.8×10^2	4.9×10^{57}	8.9×10^{57}	1.3×10^{54}	2.0×10^{54}	4.3×10^{55}	1.3×10^{56}
FRB 20190616A	1.1×10^3	2.4×10^{59}	3.0×10^{59}	1.2×10^{56}	8.0×10^{55}	2.6×10^{57}	1.6×10^{58}
FRB 20190617A	8.7×10^2	7.1×10^{57}	1.0×10^{58}	6.4×10^{54}	5.3×10^{54}	7.7×10^{55}	3.2×10^{56}
FRB 20190618A	9.6×10^2	6.7×10^{57}	1.1×10^{58}	1.5×10^{54}	2.7×10^{54}	5.4×10^{55}	1.8×10^{56}
FRB 20190621A	9.8×10^2	1.8×10^{59}	7.6×10^{58}	...	1.5×10^{56}	4.4×10^{57}	9.2×10^{57}
FRB 20190624B	8.2×10^2	5.9×10^{58}	1.1×10^{59}	8.5×10^{54}	1.4×10^{55}	3.1×10^{56}	1.1×10^{57}
FRB 20190710A	1.0×10^3	4.8×10^{57}	5.4×10^{57}	2.1×10^{54}	3.2×10^{54}	6.9×10^{55}	2.0×10^{56}
FRB 20190713A	1.4×10^3	2.4×10^{59}	3.8×10^{59}	3.2×10^{55}	5.2×10^{55}	1.6×10^{57}	4.5×10^{57}
FRB 20190718A	9.7×10^2	6.7×10^{57}	1.1×10^{58}	3.2×10^{54}	4.2×10^{54}	8.4×10^{55}	2.6×10^{56}
FRB 20190722A	1.1×10^3	1.5×10^{59}	1.1×10^{59}	1.2×10^{58}	3.6×10^{56}	1.1×10^{58}	2.3×10^{58}
FRB 20190812A	1.4×10^3	1.4×10^{58}	2.8×10^{58}	4.4×10^{54}	6.1×10^{54}	1.3×10^{56}	3.8×10^{56}
FRB 20190903A	9.3×10^2	2.1×10^{59}	1.4×10^{59}	9.6×10^{55}	7.0×10^{55}	3.3×10^{57}	8.7×10^{57}
FRB 20190912A	1.1×10^3	2.5×10^{59}	1.8×10^{59}	9.9×10^{55}	8.2×10^{55}	3.7×10^{57}	1.1×10^{58}
FRB 20190912B	4.9×10^2	3.5×10^{57}	6.4×10^{57}	6.5×10^{53}	7.9×10^{53}	2.0×10^{55}	5.3×10^{55}
FRB 20190922A	9.6×10^2	4.7×10^{59}	6.7×10^{59}	3.2×10^{56}	8.8×10^{55}	3.1×10^{57}	8.3×10^{57}
FRB 20190928A	5.1×10^2	3.8×10^{57}	7.1×10^{57}	1.1×10^{54}	1.6×10^{54}	2.6×10^{55}	1.1×10^{56}
FRB 20190929B	1.5×10^3	1.5×10^{58}	3.1×10^{58}	7.0×10^{54}	7.8×10^{54}	1.9×10^{56}	5.0×10^{56}

ORCID iDs

A. Cumming  <https://orcid.org/0000-0002-6335-0169>

References

Aasi, J., Abbott, B. P., Abbott, R., et al. 2014, *PhRvD*, **89**, 122004
Aasi, J., Abbott, B. P., Abbott, R., et al. 2015, *CQGrA*, **32**, 074001
Abadie, J., Abbott, B. P., Abbott, R., et al. 2012, *ApJ*, **760**, 12
Abbott, B. P., Abbott, R., Abbott, T. D., et al. 2017a, *ApJ*, **841**, 89
Abbott, B. P., Abbott, R., Abbott, T. D., et al. 2017b, *PhRvL*, **119**, 161101
Abbott, B. P., Abbott, R., Abbott, T. D., et al. 2019a, *ApJ*, **886**, 75
Abbott, B. P., Abbott, R., Abbott, T. D., et al. 2019b, *ApJ*, **874**, 163
Abbott, B. P., Abbott, R., Abbott, T. D., et al. 2019c, *PhRvD*, **100**, 024017
Abbott, B. P., Abbott, R., Abbott, T. D., et al. 2020a, *LRR*, **23**, 3
Abbott, B. P., Abbott, R., Abbott, T. D., et al. 2017c, *PhRvL*, **119**, 161101
Abbott, B. P., Abbott, R., Abbott, T. D., et al. 2017d, *ApJL*, **848**, L13
Abbott, B. P., Abbott, R., Abbott, T. D., et al. 2018, *PhRvL*, **121**, 161101
Abbott, B. P., Abbott, R., Abbott, T. D., et al. 2020b, *CQGrA*, **37**, 055002
Abbott, B. P., Abbott, R., Abbott, T. D., et al. 2016, *PhRvD*, **93**, 122008
Abbott, R., Abbott, T. D., Abraham, S., et al. 2021, *ApJ*, **915**, 86
Abbott, R., Abe, H., Acernese, F., et al. 2022, arXiv:2210.10931
Accadia, T., Acernese, F., Alshourbagy, M., et al. 2012, *JINST*, **7**, P03012
Acernese, F., Agathos, M., Agatsuma, K., et al. 2015, *CQGrA*, **32**, 024001
Amiri, M., Bandura, K., Bhardwaj, M., et al. 2019a, *Natur*, **566**, 235
Amiri, M., Bandura, K., Bhardwaj, M., et al. 2019b, *Natur*, **566**, 230
Anderson, M. M., Hallinan, G., Eastwood, M. W., et al. 2018, *ApJ*, **864**, 22
Arun, K. G., Buonanno, A., Faye, G., & Ochsner, E. 2009, *PhRvD*, **79**, 104023
Babak, S., Taracchini, A., & Buonanno, A. 2017, *PhRvD*, **95**, 024010
Bandura, K., Addison, G. E., Amiri, M., et al. 2014, *Proc. SPIE*, **9145**, 914522
Bannister, K. W., Deller, A. T., Phillips, C., et al. 2019, *Sci*, **365**, 565
Bannister, K. W., Shannon, R. M., Macquart, J.-P., et al. 2017, *ApJL*, **841**, L12
Bhandari, S., Heintz, K. E., Aggarwal, K., et al. 2022, *AJ*, **163**, 69
Bhandari, S., Sadler, E. M., Prochaska, J. X., et al. 2020, *ApJL*, **895**, L37
Bhardwaj, M., Gaensler, B. M., Kaspi, V. M., et al. 2021a, *ApJL*, **910**, L18

Bhardwaj, M., Kirichenko, A. Y., Michilli, D., et al. 2021b, *ApJL*, **919**, L24
Blanchet, L., Iyer, B. R., Will, C. M., & Wiseman, A. G. 1996, *CQGrA*, **13**, 575
Bochenek, C. D., Ravi, V., Belov, K. V., et al. 2020, *Natur*, **587**, 59
Bohé, A., Faye, G., Marsat, S., & Porter, E. K. 2015, *CQGrA*, **32**, 195010
Bohé, A., Marsat, S., & Blanchet, L. 2013, *CQGrA*, **30**, 135009
Bouwuis, M., Bannister, K. W., Macquart, J.-P., et al. 2020, *MNRAS*, **497**, 125
Brown, D. A., Harry, I., Lundgren, A., & Nitz, A. H. 2012, *PhRvD*, **86**, 084017
Caleb, M., Flynn, C., Bailes, M., et al. 2017, *MNRAS*, **468**, 3746
Capano, C., Harry, I., Privitera, S., & Buonanno, A. 2016, *PhRvD*, **93**, 124007
Cassanelli, T., Leung, C., Rahman, M., et al. 2022, *AJ*, **163**, 65
Champion, D. J., Petroff, E., Kramer, M., et al. 2016, *MNRAS Lett.*, **460**, L30
Chatterjee, S., Law, C. J., Wharton, R. S., et al. 2017, *Natur*, **541**, 58
CHIME/FRB Collaboration 2020, The Canadian Hydrogen Intensity Mapping Experiment is a Revolutionary new Canadian Radio Telescope Designed to answer Major Questions in Astrophysics and Cosmology, <https://chime-experiment.ca/>
CHIME/FRB Collaboration, Amiri, M., Bandura, K., et al. 2018, *ApJ*, **863**, 48
CHIME/FRB Collaboration, Amiri, M., Andersen, B. C., et al. 2021, *ApJS*, **257**, 59
CHIME/FRB Collaboration, Andersen, B. C., Bandura, K. M., et al. 2020, *Natur*, **587**, 54
CHIME/FRB Collaboration, Andersen, B. C., Bandura, K., et al. 2019, *ApJL*, **885**, L24
Cho, M.-A. 2019, PhD thesis, Univ. Maryland
Connor, L., Miller, M. C., & Gardenier, D. W. 2020, *MNRAS*, **497**, 3076
Cordes, J. M., & Chatterjee, S. 2019, *ARA&A*, **57**, 417
Cordes, J. M., & Lazio, T. J. W. 2002, arXiv:astro-ph/0207156
Corsi, A., & Owen, B. J. 2011, *PhRvD*, **83**, 104014
Dal Canton, T., & Harry, I. W. 2017, arXiv:1705.01845
Dolag, K., Gaensler, B. M., Beck, A. M., & Beck, M. C. 2015, *MNRAS*, **451**, 4277
Falcke, H., & Rezzolla, L. 2014, *A&A*, **562**, A137
Foreman-Mackey, D., Hogg, D. W., Lang, D., & Goodman, J. 2013, *PASP*, **125**, 306
Gao, H., Zhang, B., & Lü, H.-J. 2016, *PhRvD*, **93**, 044065

- Goodman, J., & Weare, J. 2010, *CAMCS*, **5**, 65
- Gourdji, K., Rowlinson, A., Wijers, R. A. M. J., & Goldstein, A. 2020, *MNRAS*, **497**, 3131
- Grote, H. 2010, *CQGra*, **27**, 084003
- Harry, I. W., & Fairhurst, S. 2011, *PhRvD*, **83**, 084002
- Harry, I. W., Fairhurst, S., & Sathyaprakash, B. S. 2008, *CQGra*, **25**, 184027
- Harry, I. W., Nitz, A. H., Brown, D. A., et al. 2014, *PhRvD*, **89**, 024010
- Heintz, K. E., Prochaska, J. X., Simha, S., et al. 2020, *ApJ*, **903**, 152
- Hessels, J. W. T., Ransom, S. M., Stairs, I. H., et al. 2006, *Sci*, **311**, 1901
- Ho, W. C. G., Jones, D. I., Andersson, N., & Espinoza, C. M. 2020, *PhRvD*, **101**, 103009
- Husa, S., Khan, S., Hannam, M., et al. 2016, *PhRvD*, **93**, 044006
- Ioka, K. 2001, *MNRAS*, **327**, 639
- Khan, S., Husa, S., Hannam, M., et al. 2016, *PhRvD*, **93**, 044007
- Kirsten, F., Marcote, B., Nimmo, K., et al. 2022, *Natur*, **602**, 585
- Kiziltan, B., Kottas, A., De Yoreo, M., & Thorsett, S. E. 2013, *ApJ*, **778**, 66
- Kokkotas, K. D., Apostolatos, T. A., & Andersson, N. 2001, *MNRAS*, **320**, 307
- Kreidberg, L., Bailyn, C. D., Farr, W. M., & Kalogera, V. 2012, *ApJ*, **757**, 36
- Kumar, P., Shannon, R. M., Oslowski, S., et al. 2019, *ApJL*, **887**, L30
- Levin, Y., & van Hoven, M. 2011, *MNRAS*, **418**, 659
- Li, B.-A., Krastev, P. G., Wen, D.-H., & Zhang, N.-B. 2019, *EPJA*, **55**, 117
- Li, Y., & Zhang, B. 2020, *ApJL*, **899**, L6
- LIGO Scientific Collaboration 2018, LIGO Algorithm Library, doi:10.7935/GT1W-FZ16
- Lorimer, D. R., Bailes, M., McLaughlin, M. A., Narkevic, D. J., & Crawford, F. 2007, *Sci*, **318**, 777
- Luo, R., Men, Y., Lee, K., et al. 2020, *MNRAS*, **494**, 665
- Lyons, N., O'Brien, P. T., Zhang, B., et al. 2010, *MNRAS*, **402**, 705
- Macquart, J.-P., Prochaska, J. X., McQuinn, M., et al. 2020, *Natur*, **581**, 391
- Marcote, B., Nimmo, K., Hessels, J. W. T., et al. 2020, *Natur*, **577**, 190
- Margalit, B., Berger, E., & Metzger, B. D. 2019, *ApJ*, **886**, 110
- Margalit, B., Metzger, B. D., & Sironi, L. 2020, *MNRAS*, **494**, 4627
- Masui, K., Lin, H.-H., Sievers, J., et al. 2015, *Natur*, **528**, 523
- Mena-Parra, J., Leung, C., Cary, S., et al. 2022, *AJ*, **163**, 48
- Metzger, B. D., Berger, E., & Margalit, B. 2017, *ApJ*, **841**, 14
- Mikoczi, B., Vasúth, M., & Gergely, L. Á. 2005, *PhRvD*, **71**, 124043
- Miller, M. C., & Miller, J. M. 2014, *PhR*, **548**, 1
- Mishra, C. K., Kela, A., Arun, K. G., & Faye, G. 2016, *PhRvD*, **93**, 084054
- Moortgat, J., & Kuijpers, J. 2005, in Proc. 22nd Texas Symp. on Relativistic Astrophysics, ed. P. Chen et al. (Stanford, CA: Stanford Univ.), 326
- Newburgh, L. B., Addison, G. E., Amiri, M., et al. 2014, *Proc. SPIE*, **9145**, 91454V
- Nitz, A., Harry, I., Brown, D., et al. 2020, gwastro/pycbc: PyCBC, v1.16.6, Zenodo, doi:10.5281/zenodo.3961510
- Nitz, A. H., Dent, T., Dal Canton, T., Fairhurst, S., & Brown, D. A. 2017, *ApJ*, **849**, 118
- Owen, B. J., & Sathyaprakash, B. S. 1999, *PhRvD*, **60**, 022002
- Özel, F., Psaltis, D., Narayan, R., & McClintock, J. E. 2010, *ApJ*, **725**, 1918
- Pace, A., Prestegard, T., Moe, B., & Stephens, B. 2012, Gravitational-Wave Candidate Event Database, <https://gracedb.ligo.org>
- Pan, Y., Buonanno, A., Taracchini, A., et al. 2014, *PhRvD*, **89**, 084006
- Petroff, E., Barr, E. D., Jameson, A., et al. 2016, *PASA*, **33**, e045
- Petroff, E., Hessels, J. W. T., & Lorimer, D. R. 2019, *A&ARv*, **27**, 4
- Petroff, E., Hessels, J. W. T., & Lorimer, D. R. 2022, *A&ARv*, **30**, 2
- Planck Collaboration, Ade, P. A. R., Aghanim, N., et al. 2016, *A&A*, **594**, A13
- Platts, E., Weltman, A., Walters, A., et al. 2019, *PhR*, **821**, 1
- Popov, S. B., & Postnov, K. A. 2013, arXiv:1307.4924
- Prochaska, J. X., & Zheng, Y. 2019, *MNRAS*, **485**, 648
- Pshirkov, M. S., & Postnov, K. A. 2010, *Ap&SS*, **330**, 13
- Quitow-James, R., Brau, J., Clark, J. A., et al. 2017, *CQGra*, **34**, 164002
- Rafiei-Ravandi, M., Smith, K. M., Li, D., et al. 2021, *ApJ*, **922**, 42
- Ravi, V. 2019, *NatAs*, **3**, 928
- Ravi, V., & Lasky, P. D. 2014, *MNRAS*, **441**, 2433
- Rowlinson, A., & Anderson, G. E. 2019, *MNRAS*, **489**, 3316
- Rowlinson, A., O'Brien, P. T., Metzger, B. D., Tanvir, N. R., & Levan, A. J. 2013, *MNRAS*, **430**, 1061
- Rowlinson, A., Starling, R. L. C., Gourdji, K., et al. 2021, *MNRAS*, **506**, 5268
- Rowlinson, A., Wiersema, K., Levan, A. J., et al. 2010, *MNRAS*, **408**, 383
- Sagiv, A., & Waxman, E. 2002, *ApJ*, **574**, 861
- Sarin, N., & Lasky, P. D. 2021, *GREGr*, **53**, 59
- Sathyaprakash, B. S., & Dhurandhar, S. V. 1991, *PhRvD*, **44**, 3819
- Shannon, R. M., Macquart, J.-P., Bannister, K. W., et al. 2018, *Natur*, **562**, 386
- Shin, K., Masui, K. W., Bhardwaj, M., et al. 2023, *ApJ*, **944**, 105
- Spitler, L. G., Cordes, J. M., Hessels, J. W. T., et al. 2014, *ApJ*, **790**, 101
- Sutton, P. J. 2013, arXiv:1304.0210
- Sutton, P. J., Jones, G., Chatterji, S., et al. 2010, *NJPh*, **12**, 053034
- Taracchini, A., Buonanno, A., Pan, Y., et al. 2014, *PhRvD*, **89**, 061502
- The LIGO Scientific Collaboration, the Virgo Collaboration, the KAGRA Collaboration, et al. 2021, arXiv:2111.03606
- The LIGO Scientific Collaboration, the Virgo Collaboration, the KAGRA Collaboration, et al. 2023, *PhRvX*, **13**, 011048
- Thornton, D., Stappers, B., Bailes, M., et al. 2013, *Sci*, **341**, 53
- Totani, T. 2013, *PASJ*, **65**, L12
- Troja, E., Cusumano, G., O'Brien, P. T., et al. 2007, *ApJ*, **665**, 599
- Urban, A. L. 2016, PhD thesis, Univ. Wisconsin-Milwaukee
- Usov, V. V., & Katz, J. I. 2000, *A&A*, **364**, 655
- Wang, J.-S., Yang, Y.-P., Wu, X.-F., Dai, Z.-G., & Wang, F.-Y. 2016, *ApJL*, **822**, L7
- Was, M., Sutton, P. J., Jones, G., & Leonor, I. 2012, *PhRvD*, **86**, 022003
- Wen, D.-H., Li, B.-A., Chen, H.-Y., & Zhang, N.-B. 2019, *PhRvC*, **99**, 045806
- Williamson, A. R., Biwer, C., Fairhurst, S., et al. 2014, *PhRvD*, **90**, 122004
- Yamasaki, S., & Totani, T. 2020, *ApJ*, **888**, 105
- Yamasaki, S., Totani, T., & Kiuchi, K. 2018, *PASJ*, **70**, 39
- Yao, J. M., Manchester, R. N., & Wang, N. 2017, *ApJ*, **835**, 29
- Zhang, B. 2014, *ApJL*, **780**, L21
- Zhang, B. 2018, *ApJL*, **867**, L21
- Zhang, B. 2020a, *Natur*, **587**, 45
- Zhang, B. 2020b, *ApJL*, **890**, L24
- Zink, B., Lasky, P. D., & Kokkotas, K. D. 2012, *PhRvD*, **85**, 024030